UNIVERSITY OF CALIFORNIA SAN DIEGO

Diagnosis and Optimization of High Voltage Cathode Materials and Electrolyte for Next Generation Li-ion Batteries

A Dissertation submitted in partial satisfaction of the requirements
for the degree Doctor of Philosophy

in

NanoEngineering

by

Yixuan Li

Committee in charge:

Professor Ying Shirley Meng, Chair
Professor Ping Liu, Co-Chair
Professor Seth M. Cohen
Professor Chunhui Du
Professor David Fenning

2022

The Dissertation of Yixuan Li is approved, and it is acceptable in quality and form for publication on microfilm and electronically.

University of California San Diego

2022

DEDICATION

To my grandmother Wenhua Pan

To all my female scientist fellows

TABLE OF CONTENTS

LIST OF FIGURES

LIST OF TABLES

ACKNOWLEDGEMENTS

All the work presented here would not be possible without the support of many. Firstly, I would like to thank my PhD advisor Professor Ying Shirley Meng for her guidance and support over the years. She is always sharp and full of insights and vision in directing my scientific research. Shirley has also been a unique and important mentor of my life, from whom I leaned to be strong for myself and never throw away my shot. It was my honor to work with her in the last five years. I would also like to express my deep gratitude to my committee members: Professor Ping Liu, Professor Seth M. Cohen, Professor Chunhui Du, and Professor David Fenning, who provided the most thoughtful suggestions during our discussions in the past years.

During my PhD, I received infinite love and support from my friends and my family. I would like to thank my parents, Rong Huang and Dr. Ningchuan Li, who always believe in me when I am taking this relatively different route from a lot of my peers back in high school or undergrad. I am also deeply grateful to my friends, Dr. Darren Tan, Dr. Rory Runser, Xu Fan, and Dr. Rina Schul, who have always been there for me to share my joys and tears during this journey.

Moreover, I would like to acknowledge all my brilliant-minded collaborators at UC San Diego. I am grateful that I was able to work with Dr. Minghao Zhang, Dr. Weikang Li, Dr. Jean-Marie Doux, Dr. Hyeseung Chung, Dr. Thomas Wynn, Dr. Darren Tan, Baharak Sayahpour, Diyi Cheng, Weiliang Yao, and Ryosuke Shimizu. They have been amazing coworkers and friends through my PhD. They generously shared their knowledge with me and provided countless insightful discussions. A lot of my work could never be completed without

their intellectual contribution. I would also like to thank the hard work done by the undergraduate students working in my projects: Susie Park, Meghan Shen, and Carlos Mejia. I am also grateful to all my group mates in Laboratory for Energy Storage and Conversion. Each of them helped and inspired me in many ways.

Furthermore, I would like to thank my external collaborators and co-authors: Dr. Mateusz Zuba, Dr. Zachary Lebens-Higgins, and Dr. Louis Piper from Binghamton University; Dr. Shinichi Kumakura, Dr. HongNam Nguyen, Dr. Jens Paulsen, and Dr. Wendy Zhou from Umicore; Dr. Ashfia Huq from Oak Ridge National Lab; Dr. Kamila Wiaderek, Dr. Olaf J. Borkiewicz, and Kevin Beyer from Advanced Photon Source in Argonne Nation Lab; Dr. Bao Qiu and Dr. Zhaoping Liu from Ningbo Institute of Materials Technology and Engineering; Dr. Antonin Grenier and Dr. Karena W. Chapman from Stony Brook University. All my collaborators were so helpful and proactive whenever I wanted to discuss my research with them. I am truly grateful for their technical expertise and invaluable support throughout my PhD.

Lastly, I would like to acknowledge the funding sources for my research: NorthEast Center for Chemical Energy Storage (NECCES), an Energy Frontier Research Center funded by the U.S. Department of Energy, Office of Science, Office of Basic Energy Sciences under Award No. DE-SC0012583; Umicore and LESC collaborative project for developing high energy cathode materials for next-generation Li-ion batteries.

Chapter 2, in full, is a reprint of the material, as it appears in: Chung, H.*, Li, Y.*, Zhang, M., Grenier, A., Mejia, C., Cheng, D., Sayahpour, B., Song, C., Shen, M.H., Huang, R., Wu, E.A., Chapman, K.W., Kim, S.J., and Meng, Y.S., 2022. Mitigating Anisotropic Changes in Classical Layered Oxide Materials by Controlled Twin Boundary Defects for Long Cycle

Life Li-Ion Batteries. Chemistry of Materials, 34(16), pp.7302–7312. The dissertation author was the co-primary investigator and co-first author of this paper.

Chapter 3, in full, is a reprint of the material, as it appears in: Li, Y., Zuba, M.J., Bai, S., Lebens-Higgins, Z.W., Qiu, B., Park, S., Liu, Z., Zhang, M., Piper, L.F. and Meng, Y.S., 2021. Regeneration of degraded Li-rich layered oxide materials through heat treatment-induced transition metal reordering. Energy Storage Materials, 35, pp.99-107. The dissertation author was the primary investigator and first author of this paper.

Chapter 4, in full, is a reprint of the material, as it appears in: Li, Y., Li, W., Shimizu, R., Cheng, D., Nguyen, H., Paulsen, J., Kumakura, S., Zhang, M. and Meng, Y.S., 2022. Elucidating the Effect of Borate Additive in High-Voltage Electrolyte for Li-Rich Layered Oxide Materials. Advanced Energy Materials, 12(11), p.2103033.The dissertation author was the primary investigator and first author of this paper.

VITA

2016 Bachelor of Engineering in Energy Science and Engineering, Nanjing University

2018 Master of Science in NanoEngineering, University of California, San Diego

2022 Doctor of Philosophy in NanoEngineering, University of California San Diego

PUBLICATIONS

(* authors contributed equally to the work)

Li,Y., Li, W., Shimizu, R., Cheng, D., Nguyen, H., Paulsen, J., Kumakura, S., Zhang, M., Meng, Y.S., 2022. Elucidating the Effect of Borate Additive in High Voltage Electrolyte for Li-rich Layered Oxide Materials. Advanced Energy Materials, 12(11), p.2103033.

Li, Y., Zuba, M.J., Bai, S., Lebens-Higgins, Z.W., Qiu, B., Park, S., Liu, Z., Zhang, M., Piper, L.F. and Meng, Y.S., 2021. Regeneration of Degraded Li-rich Layered Oxide Materials through Heat Treatment-induced Transition Metal Reordering. Energy Storage Materials, 35, pp.99-107.

Chung, H.*, **Li, Y.***, Zhang, M., Grenier, A., Mejia, C., Cheng, D., Sayahpour, B., Song, C., Shen, M.H., Huang, R., Wu, E.A., Chapman, K.W., Kim, S.J., and Meng, Y.S., 2022. Mitigating Anisotropic Changes in Classical Layered Oxide Materials by Controlled Twin Boundary Defects for Long Cycle Life Li-Ion Batteries. Chemistry of Materials, 34(16), pp.7302–7312.

Hirsh, H.*, **Li, Y.***, Cheng, J.H., Shimizu, R., Zhang, M., Zhao, E. and Meng, Y.S., 2021. The Negative Impact of Transition Metal Migration on Oxygen Redox Activity of Layered Cathode Materials for Na-Ion Batteries. Journal of The Electrochemical Society, 168(4), p.040539.

Hirsh, H.*, **Li, Y.***, Tan, D.H., Zhang, M., Zhao, E. and Meng, Y.S., 2020. Sodium-ion Batteries Paving the Way for Grid Energy Storage. Advanced Energy Materials, 10(32), p.2001274.

Grenier, A., Kamm, G.E., **Li, Y.**, Chung, H., Meng, Y.S. and Chapman, K.W., 2021. Nanostructure Transformation as a Signature of Oxygen Redox in Li-Rich 3d and 4d Cathodes. Journal of the American Chemical Society, 143(15), pp.5763-5770.

Li, Q., Lebens-Higgins, Z.W., **Li, Y.**, Meng, Y.S., Chuang, Y.D., Piper, L.F., Liu, Z. and Yang, W., 2021. Could Irradiation Introduce Oxidized Oxygen Signals in Resonant Inelastic X-ray

Scattering of Battery Electrodes? The Journal of Physical Chemistry Letters, 12(4), pp.1138-1143.

Li, W., Cho, Y.G., Yao, W., **Li, Y.**, Cronk, A., Shimizu, R., Schroeder, M.A., Fu, Y., Zou, F., Battaglia, V. and Manthiram, A., 2020. Enabling high areal capacity for Co-free high voltage spinel materials in next-generation Li-ion batteries. Journal of Power Sources, 473, p.228579.

Hirsh, H., Olguin, M., Chung, H., **Li, Y.**, Bai, S., Feng, D., Wang, D., Zhang, M. and Meng, Y.S., 2019. Meso-Structure Controlled Synthesis of Sodium Iron-Manganese Oxides Cathode for Low-Cost Na-Ion Batteries. Journal of The Electrochemical Society, 166(12), p.A2528.

Zhang, M., Qiu, B., Gallardo-Amores, J.M., Olguin, M., Liu, H., **Li, Y.**, Yin, C., Jiang, S., Yao, W., Arroyo-de Dompablo, M.E. and Liu, Z., 2021. High pressure effect on structural and electrochemical properties of anionic redox-based lithium transition metal oxides. Matter, 4(1), pp.164-181.

Zuba, M.J., Grenier, A., Lebens-Higgins, Z., Fajardo, G.J.P., **Li, Y.**, Ha, Y., Zhou, H., Whittingham, M.S., Yang, W., Meng, Y.S. and Chapman, K.W., 2021. Whither Mn Oxidation in Mn-Rich Alkali-Excess Cathodes?. ACS Energy Letters, 6(3), pp.1055-1064.

Wu, E.A., Banerjee, S., Tang, H., Richardson, P.M., Doux, J.M., Qi, J., Zhu, Z., Grenier, A., **Li, Y.**, Zhao, E. and Deysher, G., 2021. A stable cathode-solid electrolyte composite for high-voltage, long-cycle-life solid-state sodium-ion batteries. Nature communications, 12(1), pp.1-11.

Lebens-Higgins, Z.W., Chung, H., Zuba, M.J., Rana, J., **Li, Y.**, Faenza, N.V., Pereira, N., McCloskey, B.D., Rodolakis, F., Yang, W. and Whittingham, M.S., 2020. How bulk sensitive is hard X-ray photoelectron spectroscopy: accounting for the cathode–electrolyte interface when addressing oxygen redox. The journal of physical chemistry letters, 11(6), pp.2106-2112.

Chung, H., Lebens-Higgins, Z., Sayahpour, B., Mejia, C., Grenier, A., Kamm, G.E., **Li, Y.**, Huang, R., Piper, L.F., Chapman, K.W. and Doux, J.M., 2021. Experimental considerations to study Li-excess disordered rock salt cathode materials. Journal of Materials Chemistry A, 9(3), pp.1720-1732.

Lebens-Higgins, Z.W., Vinckeviciute, J., Wu, J., Faenza, N.V., **Li, Y.**, Sallis, S., Pereira, N., Meng, Y.S., Amatucci, G.G., Der Ven, A.V. and Yang, W., 2019. Distinction between intrinsic and X-ray-induced oxidized oxygen states in Li-rich 3d layered oxides and LiAlO2. The Journal of Physical Chemistry C, 123(21), pp.13201-13207.

ABSTRACT OF THE DISSERTATION

Diagnosing and Optimization of High Voltage Cathode Materials and Electrolyte for Next Generation Li-ion Batteries

by

Yixuan Li

Doctor of Philosophy in NanoEngineering

University of California San Diego, 2022

Professor Ying Shirley Meng, Chair
Professor Ping Liu, Co-Chair

The rapid growth of the electric vehicle market requires the development of Li-ion batteries (LIBs) with higher energy density and longer cycle life. The classical layered nickel, manganese, and cobalt oxides (NMC) and lithium-rich layered oxides (LRLO) have attracted great interest as high-energy LIB cathode materials due to their high theoretical capacity. However, their inherent structure instability at the highly-

delithiated state and the electrolyte degradation induced at high voltage cause cell degradation as cycling proceeds. In this thesis, different degradation mechanisms and the corresponding mitigating strategies are studied for both NMC and LRLO materials. Firstly, twin boundary defect engineering was adopted in a series of NMC cathodes to improve the structure and cycling stability. The radially aligned twin boundaries with the formation of rocksalt-like phase along the boundaries are observed through STEM, acting as a rigid framework that mitigates the anisotropic changes during charge and discharge, as confirmed by *operando* XRD. The reduced microcrack formation is also confirmed by FIB and SEM. Secondly, an in-depth understanding of the heat treatment induced structure and voltage recovery in cycled LRLO is provided. The transition metal layer reordering is identified as the key factor under the structure recovery of degraded LRLO. The reappearance of the honeycomb superlattice during heat treatment is captured through NPD, PDF, and EXAFS. In addition, an ambient-air relithiation combined with heat treatment is proved to effectively recover both the voltage and capacity of cycled LRLO. Lastly, lithium bis-(oxalate)borate (LiBOB) is studied as an electrolyte additive in protecting cathode-electrolyte interphase (CEI) from hydrofluoric acid (HF) corrosion induced by electrolyte decomposition at high voltage. Analytical EM under cryo-condition confirms the formation of a uniform CEI and less phase transformation on the LRLO particle surface. The formation of B-F species is identified in the cycled electrolyte with NMR, elucidating the HF scavenger effect of LiBOB. Due to less HF corrosion on both CEI and SEI, a reduced amount of transition metal dissolution and redeposition has been proved by EDX and XPS. The prevention of cell crosstalk thereby mitigates the capacity decay in LRLO/graphite full cells.

Chapter 1. Introduction

1.1 Overview of Li-ion Batteries

The global production and consumption of electricity grows rapidly since the second industrial revolution.[1,2] While fossil fuels maintain to be the major source of electricity generation, there has been significant growth of cleaner and more sustainable energy sources such as solar energy, wind energy, hydropower, as shown in Figure 1.1.[3,4] Due to the intermittent nature of most of the renewable energy sources, the development for energy storage devices has attracted many research interests in the past a few decades.[5] Lithium-ion batteries (LIBs) as an efficient energy storage device has been studied since 1950s. In 1991, Sony Corp. introduced the first commercialized secondary LIB to the market with lithium cobalt oxide ($LiCoO_2$) as the cathode and petroleum coke as the anode.[6] Ever since then, LIBs have been applied to a diversity of consumer products in the portable electronic devices market such as phones, computers, cameras. In recent years, LIBs have also been adopted in the field of electric vehicles (EV) and grid storage.

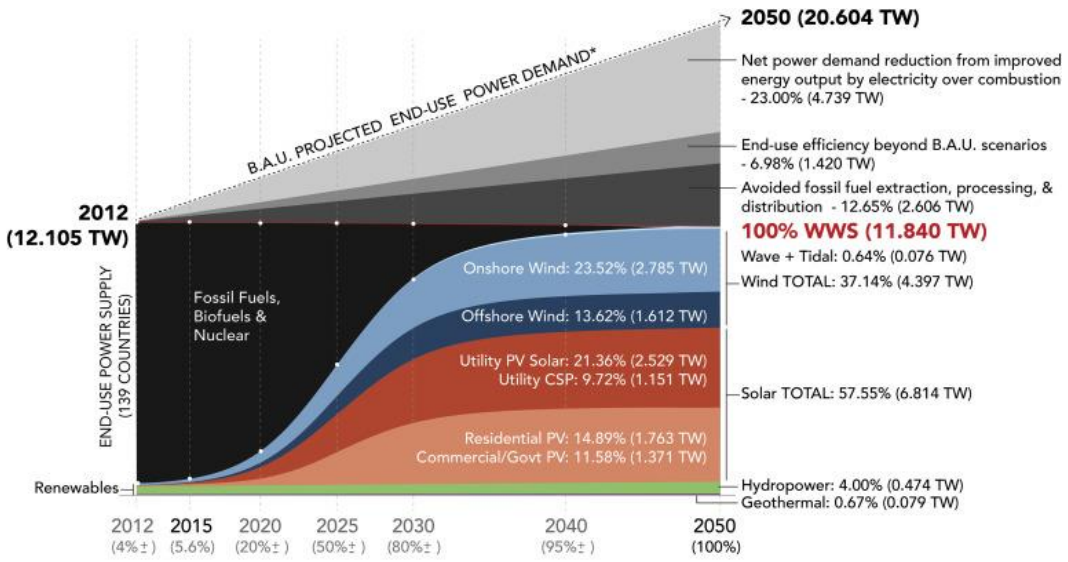

Figure 1.1 Projected power supply and demand in 139 country-summed case.[3]

LIBs exhibit two fundamental advantages compared to other battery chemistries. Firstly, lithium is the lightest metal element and has one of the smallest ionic radii for a single charged ion, which allows lithium batteries to deliver larger gravimetric and volumetric energy densities than utilizing other single charged metal ions. Secondly, lithium has the lowest reduction potential of any element, which enables lithium batteries to have higher cell potential compared to other elements. As illustrated in Figure 1.2[7], a LIB contains four main components - cathode, anode, separator, and electrolyte. Other than these four components, an actual battery also includes current collector, tabs, insulation pieces, cell containers such as pouch bag or cylindrical cans. LIBs store charges through redox reactions happening in the cathode and anode. The electrochemical reaction of a commercial LIB with $LiCoO_2$ cathode and graphite anode can be expressed as following:

$$\text{Cathode: } LiCoO_2 \leftrightarrow Li_xCoO_2 + xLi^+ + xe^- \quad (1.1)$$

$$\text{Anode: } 6C + xLi^+ \leftrightarrow Li_xC_6 \quad (1.2)$$

During the charge process, Li-ions are extracted from the metal oxide cathode and move through the electrolyte to the anode (graphite, Li metal, or other anode materials). At the same time, the electrons are pulled from the cathode and move to the anode through the outer electric circuit. This process occurs in reverse in the discharge process. The electrolyte in the battery needs to be conductive for Li-ions but insulate for electrons, so that the Li-ions can migrate between the two electrodes in the electrolyte whereas electrons travel through the outer circuit to perform work. Common electrolytes in commercial LIBs contains lithium hexafluorophosphate ($LiPF_6$) salt and carbonate-based solvents such as ethylene carbonate (EC), ethyl methyl carbonate (EMC), and/or dimethyl carbonate (DMC). The separator (usually polymers) separates the cathode and anode from contacting and shorting.

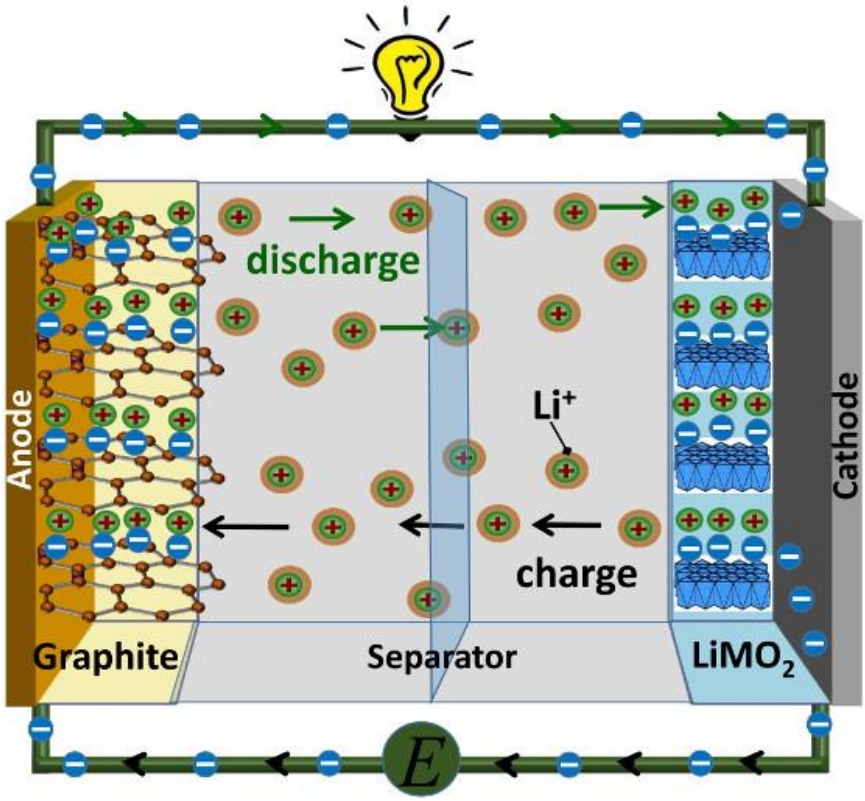

Figure 1.2 Schematics of Li-ion battery system.[7]

Although LIBs are one of the most promising energy storage technologies, it faces degradation problems such as the capacity and energy decay over cycling. Figure 1.3 provides a schematic of cell degradation mechanisms in LIBs, including the problems rooted from the cathode, the anode, the electrolyte, and the cell crosstalk.[8] For example, metal oxide cathode may undergo structure disordering and surface phase transformation during cycling, leading to particle crack formation and transition metal dissolution. The anode side have issues such as graphite exfoliation, Li dendrite formation, Cu cracking and contact loss. The electrolyte in LIBs also experiences degradation such as salt and solvent decomposition, acidic species generation, which in turn causes the corrosion of solid-electrolyte-interphase (SEI) and cathode-electrolyte-interphase (CEI). The electrolyte decomposition and its damage on SEI and CEI promotes the

issues rooted from cathode or anode side and lead to cell crosstalk such as transition metal re-deposition on the graphite and cell level Li inventory loss. The different reaction mechanisms make LIB degradation an extremely complicated issue that requires suitable analytical characterization tools from a variety of length and time scales.

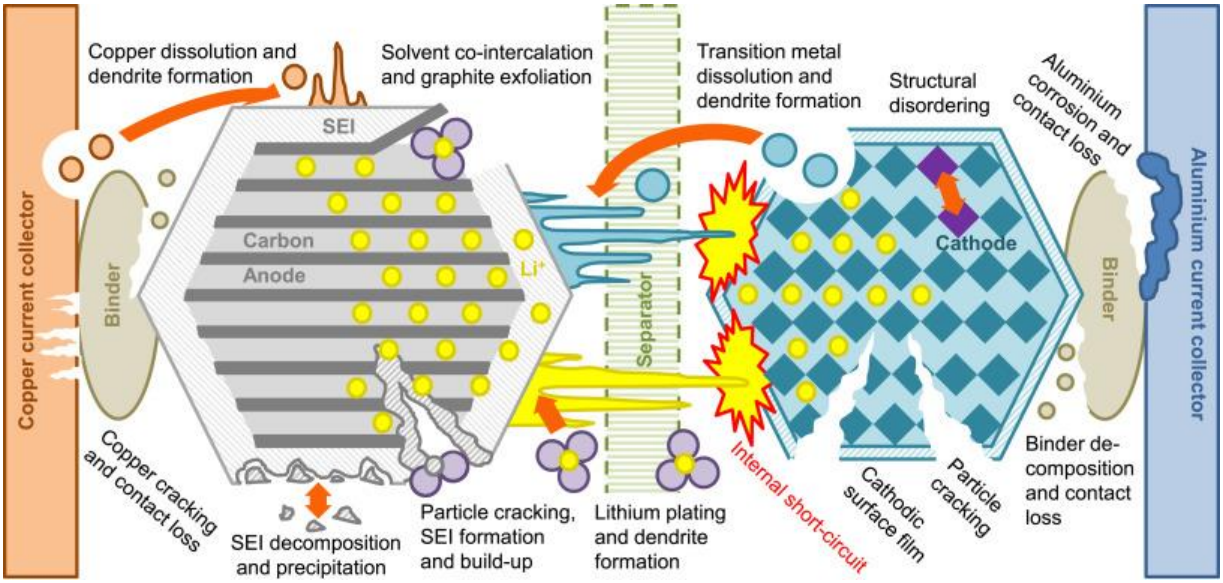

Figure 1.3 Degradation mechanisms in Li-ion batteries.[8]

1.2 Cathode Materials in Li-ion Batteries

Cathode active materials usually take about 40% of the cost of the cell and have large influence on the overall cell performance.[9,10] Thus, the study on the structure and properties of cathode materials has always been one of the most important directions in the battery field. In the 1970s, Whittingham brought up the concept of intercalation compounds using a TiS_2 cathode paired with a lithium metal anode.[11] In the 1980s, Goodenough and co-workers discovered $LiCoO_2$ (LCO) cathode and found that a large number of Li-ions can be extracted from the cathode at the voltage range of 3-4.3 V versus Li^+/Li^0.[12] Ever since then, the cathode research was mostly driven

by the need for developing materials with higher capacity and higher energy density to suit the rapid growth of the electronics and the EV market. In recent years, due to the price increase of Co and Ni, the consideration of cost-effectiveness and the research interest in designing Co-free materials also greatly increased.

1.2.1 Crystal Structure of Cathode Materials

Most of the cathode materials studied nowadays are metal oxides consisting of close-packed oxygen planes with metal ions occupying the octahedral sites formed by oxygen ions. Figure 1.4 shows the three major structural groups of cathode materials in state-of-art LIBs, which are olivine $LiTMPO_4$, layered $LiTMO_2$, and spinel $LiTM_2O_4$ (TM = Mn, Co, Ni, or other transition metals).[13] Although containing similar atoms such as Li, O, and TM, the periodic arrangement for the atoms is intrinsically different in these three structures. The Li-ion transport dimensionality is different in these three structures, where olivine structure has a one-dimensional Li^+ diffusion channel, and layered structure holds a two-dimensional Li^+ transport pathway, and spinel structure occupies a three-dimensional Li^+ transport framework. These structural differences and its influence on the material properties will be further discussed in the following paragraphs.

Lithium iron phosphate $LiFePO_4$ (LFP) is a typical example of the olivine structure which consists of corner-shared FeO_6 octahedra and edge-shared LiO_6 octahedra as well as PO_4 tetrahedra with Li^+ diffuse through the [010] direction. In LFP, the oxygen atoms are strongly bonded with P and Fe atoms, resulting in an improved structure stability and safety of LFP compared to LCO or other layered oxide materials, especially at high temperature.[14] However, LFP also exhibits relatively low electronic conductivity due to the strong covalent nature of oxygen bonds. The 1D pathway also leads to sluggish Li^+ diffusion and limit the ionic conductivity of LFP. The Fe dissolution also leads to capacity decay over cycling.[15] In summary, LFP shows advantages in

cycling stability, safety, and cost-effectiveness, but has drawbacks such as low operating voltage and low energy density. Some other phosphates materials such as $LiCoPO_4$ (LCP), $LiMnPO_4$ (LMP), and $LiNiPO_4$ (LNP) have been developed and occupies much higher operating voltage (4.8 V vs. Li^+/Li^0 for LCP, 5.1 V vs. Li^+/Li^0 for LNP). Compared to LFP, these materials offer much higher energy density. However, these materials also post significant challenges to the designing of novel electrolytes to handle the side reactions triggered at high voltage.

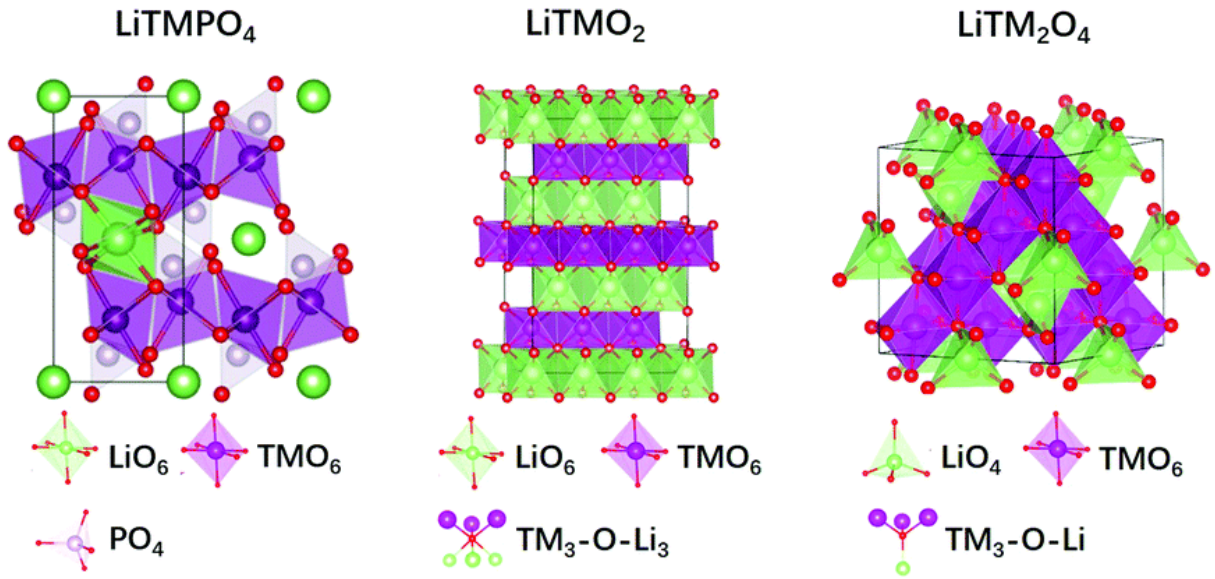

Figure 1.4 The major structural groups of cathode materials (olivine $LiTMPO_4$, layered $LiTMO_2$, and spinel $LiTM_2O_4$) in LIBs.[13]

Unlike olivine structure with corner-shared TMO_6 octahedra, layered oxide materials contain edge-shared TMO_6 octahedra. In a layered structure with O3 phase, LiO_6 octahedra also shares edge with TMO_6 octahedra, forming the R-3m structure with Li layers and TM layers on top of each other. The layered structure allows the 2D diffusion of Li^+ within the (001) plane from one LiO_6 octahedral site to another, bringing in much higher ionic conductivity than olivine structure. Many of state-of-art cathode materials belong to the layered structure, including LCO,

$LiNi_xMn_yCo_{1-x-y}O_2$ (NMC), $LiNi_xMn_yAl_{1-x-y}O_2$ (NCA), and many other compounds. During charge and discharge, these materials experience the redox of $TM^{3+/4+}$ or $TM^{2+/3+/4+}$ with simultaneous extraction/insertion of Li^+. One special category of layered oxide materials is the Li-rich layered oxide material (LRLO), denoted as a single phase solid solution $Li[Li_xTM_{1-x}]O_2$, or a nano-composite $xLi_2MnO_3 \cdot (1-x)LiTMO_2$. In this type of materials, the cationic redox alone is not sufficient to enable the large capacity observed in LRLO materials. Thus, oxygen activity, or commonly referred to as anionic redox activity, is considered providing a significant portion of the large capacities in LRLO. This category of materials will be further discussed in section 1.2.2. Compared to olivine or spinel materials, layered oxides deliver higher capacity and higher energy density as well as better ionic and electronic conductivity. High-nickel NMCs are especially known for its high specific capacity due to the large amount of Ni redox. However, layered oxides are generally less stable and safe than LFP since the Li slabs and TM slabs are only connected by oxygen atoms and the TM slabs can easily shift during high de-lithiation states.[16] Li-Ni anti-site defects, particle crack formation, surface side reactions also contribute to the capacity decay in NMC materials.[17]

Spinel $LiTM_2O_4$ belongs to the cubic Fd-3m space group with face-shared LiO_4 tetrahedra and face-shared TMO_6 octahedra. In this structure, a 3D Li-diffusion framework is accessible when some of the Li^+ occupies the empty octahedral sites during Li^+ insertion. $LiMn_2O_4$ (LMO) and $LiNi_{0.5}Mn_{1.5}O_4$ (LNMO) are representative spinel compounds. The 3D diffusion framework allows them to generally have a good ionic conductivity, thus good rate performance and power performance. Especially LNMO has attracted wide attention since the high operating voltage (4.7 V) in this material ensures the delivery of high energy density. More importantly, LNMO is a cost-effective cathode material since it is Co-free and does not contain excessive amount of Ni.

However, the disproportion reaction of Mn causes severe Mn dissolution problem in LNMO accompanied by rapid capacity decay during cycling, especially at elevated temperature (>45 °C).[18] In addition, the high operating voltage in LNMO also leads to severe side reactions in the cell system such as electrolyte decomposition and SEI/CEI corrosion, which may cause the fast decay of the cell and raise safety issues.[19]

1.2.2 Anionic Redox Activities

As mentioned in the last section, the cationic redox reaction is no longer the only form of energy storage for batteries. Recent discoveries of anionic redox materials such as LRLO or Li-rich disordered rocksalt material (DRS) have boosted the cathode material capacity to over 300 mAh g^{-1}.[20,21]

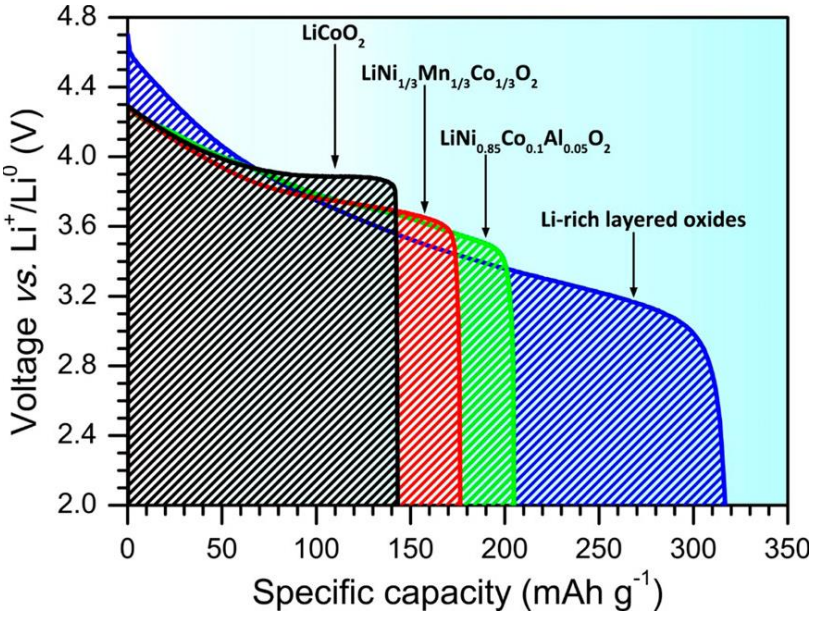

Figure 1.5 Discharge capacity in different layered oxides.[21]

Figure 1.5 compares the typical discharge voltage curve of a series of different layered oxide materials, where LRLO shows slightly lower average discharge voltage but the highest discharge capacity among these materials. As mentioned before, there are two ways to denote

LRLO in the literature: one is a nano-composite structure as $xLi_2MnO_3 \cdot (1-x)LiTMO_2$ proposed by Thackeray et al.,[22] another is a single phase solid solution as $Li[Li_xTM_{1-x}]O_2$ proposed by Dahn et al.[23] Many mechanisms have been proposed to explain the anionic redox in layered alkali transition metal oxides, mainly fall into three categories involving peroxo-like species, the formation of oxygen electron holes, or bulk O_2 molecules. Sathiya *et al.* observed the formation of peroxo-like (O_2^{n-}) species in $Li_2Ru_{0.75}Sn_{0.25}O_3$ and proposed the anionic redox between O^{2-} and O_2^{n-}.[24] McCalla *et al.* further determined the limits on the value n to be 3.0 - 3.3 for O_2^{n-} species.[25] However, Luo *et al.* pointed out that the formation of localized oxygen electron holes is the key to promote the localization, but not the formation, of O_2^{2-} peroxide species in $Li_{1.2}Ni_{0.13}Mn_{0.54}Co_{0.13}O_2$.[26] In the same material, Zhao *et al.* detected a localized oxygen lattice distortion through neutron PDF and proposed that there is a π-type overlap between the oxidized oxygen ions.[27] More recently, House *et al.* proposed the formation of molecular O_2 inside the solid as the source of oxygen redox, and those molecules reform O^{2-} in the discharge process.[28] Figure 1.6 summarizes the distinct redox mechanisms for LRLO. However, up to date there is still no certain answer or agreement on the detailed oxygen redox processes reached in the field. Although LRLO materials are known for its high capacity, it suffers from severe capacity and voltage decay problems during cycling, accompanied by structure degradation such as oxygen vacancy formation, TM migration, phase transformation, and accumulation of defects or microstrain. Chapter 3 and chapter 4 will be dedicated to understanding the bulk structure degradation and the electrode-electrolyte interphase degradation for LRLO.

Li-excess DRX material with Li and TM cation disorder is another category of materials able to utilize anionic redox. Similar to layered oxide materials, Li and TM cations occupy octahedral sites surrounded by oxygen atoms in DRX materials. In layered oxide materials, the

structure can be indexed into R-3m space group where Li and TM atoms are separated in alternating planes with a well-ordered manner. But DRX materials are indexed into a different Fm-3m space group, where the Li and TM atoms can occupy the octahedral sites randomly, even though sometimes the short-range ordered structure might still exist.[29] For decades, the cation disorder was considered detrimental to the Li^+ transport and herein poor electrochemical performance. Only in recent years, the design of Li-excess DRX materials opens a new door of high energy cathode materials. In DRX compounds, Li^+ migrates through the "O-TM" clusters in which the absence of TMs at the activated state enables facile Li migration.[30] Li-excess DRX materials also utilize anionic redox and can achieve a comparable specific capacity as LRLO materials. Compared to layered oxides which mainly use Ni, Co, and Mn, DRX materials allow the use of a wider range of TM species such as Fe and Ti and could lower down the cost of materials without limiting the energy density. However, this type of material suffers from rapid capacity decay over cycling.[29]

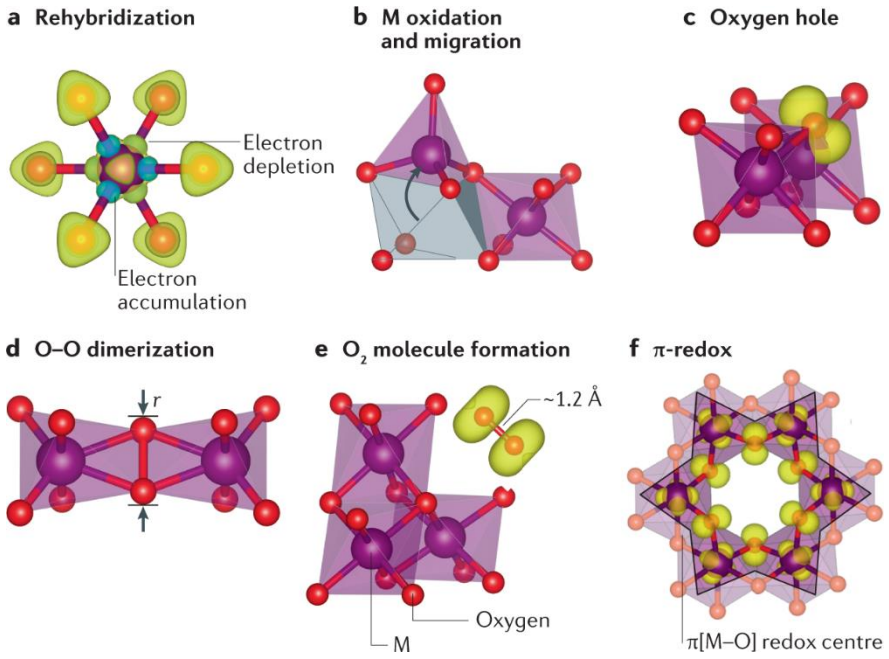

Figure 1.6 Distinct redox mechanisms for Li-rich layered oxides.

1.2.3 Degradation of Layered Oxide Materials

As mentioned in section 1.1, the degradation of a battery is a complicated problem involving many different reaction mechanisms across all the cell components. Note that the cell is a closed system, so different parts of the cell will have impact on each other and cannot be discussed as completely independent individuals. In this section, however, we will try to focus on the main degradation reactions related to layered oxide cathode material or CEI.

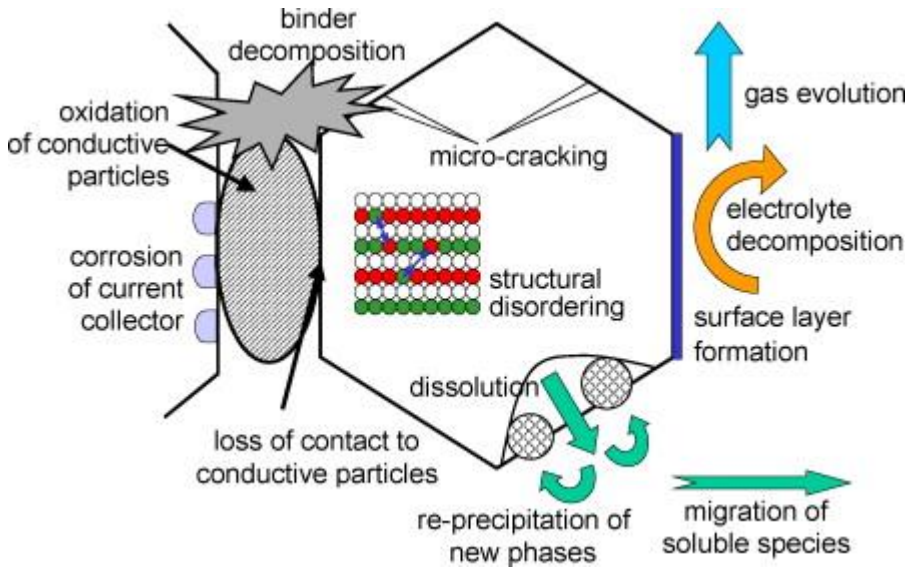

Figure 1.7 Overview of basic degradation mechanisms of cathode materials.[31]

Figure 1.7 shows a schematic of common degradations on the cathode side.[31] To start with, cathode materials may experience structural changes over cycling. For example, cation disordering, TM layer stacking faults, and spinel or rocksalt-like phase transformation (especially on the particle surfaces) are common structural degradation observed in layered oxides.[32,33] These structural changes often time lead to sluggish Li diffusion and limit the capacity in the cathode.[16] In LRLO, specifically, the accumulation of defects and microstrain and the formation of

dislocation network was also reported as one of the origins for the voltage decay.[34] In addition, the anisotropic lattice changes of NMC materials lead to the strain accumulation and the formation of both intragranular and intergranular cracks.[35,36] The crack formation may cause particle breakage and lead to an increase of electrical resistivity in the electrode through the disconnection of charge transport pathways.[35,36] Moreover, the cathode in the cell is not an isolated part. Instead, it is in contact with the electrolyte and needs to form a stable CEI upon cycling. During continuous charge and discharge, the CEI growth may lead to the growth of cell impedance and capacity fade.[31] Electrolyte decomposition, especially at high voltage (> 4.5 V), has also raised wide attention in the battery field. Since $LiPF_6$ salt is used in majority of the commercialized electrolyte nowadays, the generation of acidic species such as HF leads to severe CEI and SEI corrosion, followed by the dissolution of TM into the electrolyte and the redeposition on the graphite.[37] In the case of cathode crack formation and particle breakage, the newly exposed particle surfaces along the cracks cause even more parasitic side reaction with the electrolyte and cause the growth of impedance as well as the continuous Li consumption at the CEI.[38,39] These side reactions cause the loss of active materials as well as the loss of lithium inventory, leading to capacity decay over cycling. In addition, some surface reactions are accompanied by the evolution of gaseous species such as CO_2, CO, or C_xH_y.[40] For LRLO specifically, the irreversible oxygen redox reactions can also lead to the formation of oxygen vacancies or even nano-void in the structure and oxygen gas release can happen at the same time.[41,42] Overall, the gas generation leads to cell swelling and post severe safety concerns to the batteries.[43] Lastly, the inactive materials in the cathode electrode such as binder, carbon, and aluminum (Al) current collector also experience degradation over cycling. For example, the degraded binder causes electrode delamination problem and lead to an increase in cell impedance.[44] The Al foil corrosion may also be triggered at high voltage when the naturally

generated Al_2O_3 layer is not resistive enough.[45] When severe Al corrosion happens, the electronic conductivity and the adhesion of the cathode electrodes are impeded and will also be reflected as capacity decay over cycling.[46]

Many different optimization strategies have been employed to increase the cycling stability of layered oxide materials. For example, surface modification such as Al_2O_3 or TiO_2 coating has been well acknowledged as an effective solution to protect the cathode surface from parasitic side reactions.[7,47] The use of doping elements such as W, Mo, Ru were also heavily explored by many groups since the dopants can alter the electronic structure and stabilize the materials from capacity and voltage fade.[48–50] In addition, the design of novel electrolytes is another promising approach in protecting the CEI, reducing charge-transfer resistance, and improving cycling stability.[51–53]

1.3 Advanced Characterization

In the last section we discussed the state-of-art cathode materials and several degradation reactions happening on the cathode side. To better understand the failure mechanism, advanced characterization tools have been adopted in the field to capture and analyze the changes within the cathode and on the cathode-electrolyte interphase upon cycling. Three aspects of cathode failure identification and the corresponding characterization tools will be discussed in this section, including X-ray diffraction (XRD) and Neutron powder diffraction (NPD) in analyzing cathode bulk structures, pair distribution function (PDF) in probing cathode local ordering, and X-ray photoelectron spectroscopy (XPS) in analyzing cathode-electrolyte interphase.

1.3.1 X-ray and Neutron Diffraction

The structure of the materials affects its properties and performance in a cell in terms of capacity, energy density, rate capability, and cycling stability. XRD and NPD are two important

and widely used tools in analyzing the bulk structure of crystalline materials. The structural information extracted from these diffraction tools includes but not limited to: space group, lattice parameters, unit cell volume, atom site and occupancy as well as possible anti-site defects, microstrain. The two techniques are both non-destructive and work based on the Bragg scattering of X-ray of neutron when the beam is targeted at the sample. For crystalline materials with long range periodicity, the Bragg scattering occurs as regular arrays of waves following the Bragg's law:

$$n\lambda = 2d\sin\theta \qquad (1.3)$$

where n is the diffraction order, λ is the wavelength of the incident beam, d represents the distance between the parallel lattice planes in the crystal, and θ is the scattering angle between the incident beam and the lattice planes.

For the crystals with the same d, the resolution of the diffractometer in terms of θ is determined by the λ. The smaller the incident beam wavelength is, the higher the diffractometer resolution. Lab XRD mostly uses Cu target to generate X-ray with the wavelength of Cu Kα (λ = 1.54 Å). In comparison, synchrotron XRD (with 11-ID-B at Advanced Photon Source as an example) can reach a λ around 0.21 Å, allowing the study of fine features in the cathode materials with high accuracy, such as the Li-Ni anti-site defects, the atom occupancy, and the anisotropic thermal vibrations. In addition, synchrotron X-ray sources can provide more than a billion times higher brilliance than a lab X-ray source. The high beam intensity in synchrotron XRD significantly reduces the data collection time and sample amount requirement, which is beneficial in battery studies where the sample amount from a coin cell is typically around 5~30 mg.

Neutron diffraction follows the same fundamental rules of Bragg scattering in detecting the material structures. One major difference between the X-ray and neutron source is the

scattering cross-section of different elements. Here scattering cross-section is a measure of the scattering probability upon radiation excitation. A higher scattering cross-section reflects higher strength of the scattering. Since X-ray scattering largely depends on the electronic interactions between X-ray and the material, the scattering cross-sections of different elements increase as the atomic number increases, as shown in Figure 1.8.[54] As a result, X-ray scattering is not very sensitive to light elements such as Li or O. In comparison, neutrons interact with atomic nuclei via short range forces, leading to a seemingly random manner of the scattering cross-sections for different elements and isotopes. For LIB studies, especially LRLO studies, neutron diffraction is extremely useful because of the large scattering cross-section of O. The probing of site and occupancy of Li and O is thus enabled in NPD.[55] During my PhD work, sXRD and NPD are two important tools to understand the bulk structure of all different kinds of cathode materials. Rietveld refinement was conducted on most of the diffraction patterns to extract the rich structural information and will be further discussed in the following chapters.

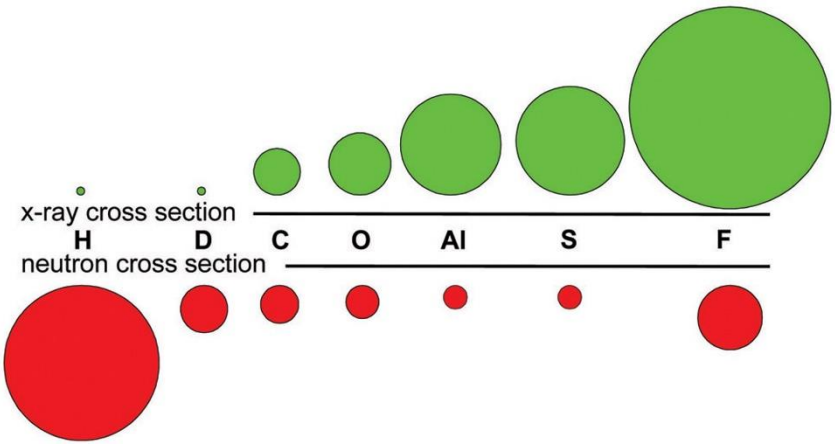

Figure 1.8 Schematic of the relative total scattering cross sections for neutrons and X-rays for several elements and isotopes.[54] (Courtesy of Muhammad Arif, NIST.)

1.3.2 Pair Distribution Function

XRD or NPD detects the long-range ordering in the materials through Bragg scattering. In comparison, PDF is another scattering technique that focuses on probing the local environment of materials through total scattering (both Bragg and diffuse scattering). XRD or NPD are effective tools in elucidating the bulk crystal structures such as space group, lattice parameters, atom sites and occupancies. However, these tools are limited when it comes to understanding the short-range ordering in the material such as M-O, M-M, O-O distances, amounts, and the degree of their orderings (M = Li or transition metals). This information is embedded in the diffuse scattering which is orders of magnitude weaker than the Bragg scattering and thus often time thrown away as background noise.[56] PDF takes both Bragg and diffuse scattering into consideration through the Fourier relationship between the real-space atomic pair density and the Q space total scattering intensity.[57] The information from PDF allows the deeper understanding of local structure in LIB materials, especially the nano-phase quantification, anionic redox reaction mechanisms, and the lithium storage mechanisms.[55,58,59] PDF are interpreted as the atomic pair distribution function G(r):

$$G(r) = 4\pi r\,[\rho(r) - \rho_0] \qquad (1.4)$$

$$G(r) = (2/\pi)\int Q[S(Q) - 1]\sin(Qr)dQ \qquad (1.5)$$

Where r is the distance between the two given atoms, ρ_0 is the average atomic number density, and $\rho(r)$ is the local atomic number density. From eq (1.4), PDF gives the probability of finding two atoms at a given inter-atomic distance r. G(r) can also be directly calculated from the measured total scattering function S(Q) through Fourier transformation, as indicated by eq (1.5).

Q is the amplitude of the transferred momentum calculated by the difference between the scattered and incident wavevector. [56]

For both Bragg diffraction and PDF techniques, enabling the measurement at *in-situ* or *operando* conditions is a heated direction in the technique development. At *ex-situ* conditions, the characterization techniques can provide a lot of valuable structural information for cathode materials as mentioned above. However, *ex-situ* tests only represent a thermodynamic trend in cathode materials and limit the detection of the rich kinetic information of the structural changes during cycling or reactions, such as the dependence of SOC, the formation and/or the disappearance of intermediate stages. For *operando* tests with electrochemical cycling, allowing the beam penetration without interfering the electrochemical reaction is the biggest challenge. As shown in Figure 1.9d,[60] AMPIX cell is one of the most used tools to enable such tests at synchrotron beamlines.[61] The cell contains a free-standing working electrode, a Li metal or Na metal anode, and two cylindrical stainless-steel parts as the current collector and "cell container" to hold the entire cell design. The window used in this design is Sigradur-(G), an electrically conductive dense glassy carbon that is amorphous and light, which allows X-ray penetration without creating extra signals in the scattering pattern. Other common cell designs are also shown in Figure 1.9, including modified coin cell with Kapton tape window,[62] "Coffee bag" type cell originated from pouch cell,[63] 18650 cell for high energy beams with direct penetration of the stainless-steel container,[64] Swagelok type cell with Be window,[65] and RATIX cell based on Kapton capillaries.[66] These operando cell designs enable an accurate and real-time reflection of the structural changes in the cathode materials during reaction or cycling. During my PhD work, PDF was mainly used to characterize the local ordering of cathode materials, and majority of the *in-situ* or *operando* experiments were carried out with the AMPIX cells.

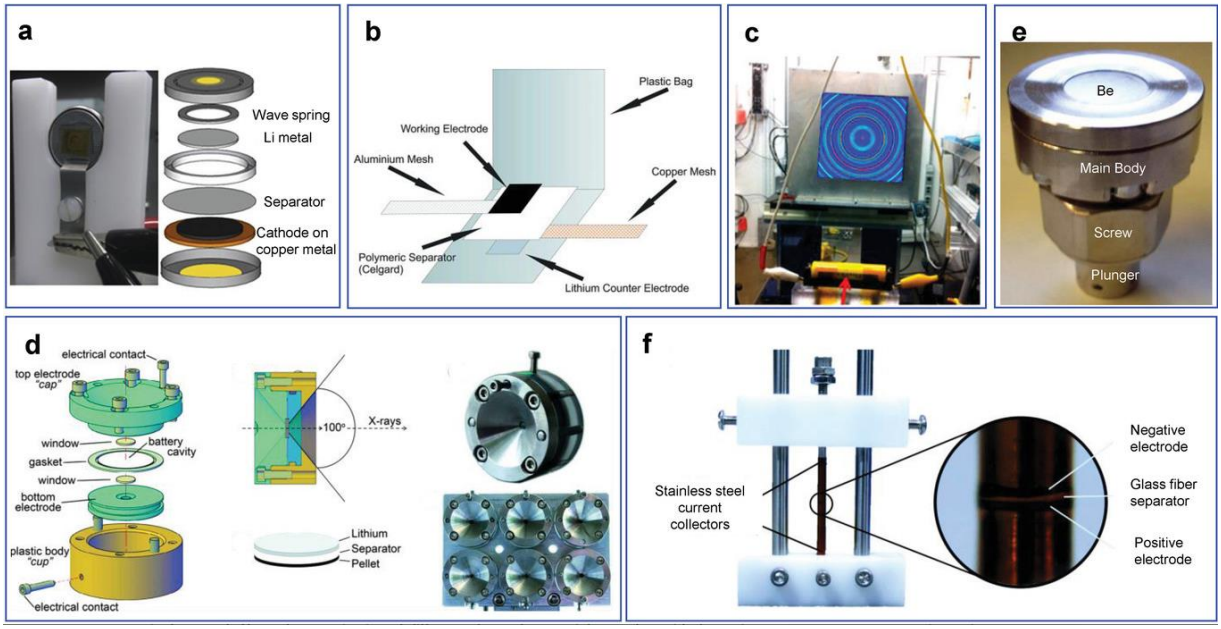

Figure 1.9 Schematics and images of the cell configuration for in-situ X-ray microscopy measurement.[60] a) Modified coin cell. b) "Coffee bag" type cell. c) 18650 cell. d) AMPIX cell. e) Swagelok type cell. f) RATIX cell.

1.3.3 X-ray Photoelectron Spectroscopy

Bragg diffraction or PDF are heavily used in deconvoluting the material structures. Different from them, XPS is a surface characterization technique that allows the study of surface chemical environment of materials. XPS can provide a lot of valuable information such as elemental composition and its dependence on the depth, chemical states of each element, and the bonding information of these elements. XPS works through the photoelectric effect:

$$BE = h\nu - (KE + \Phi_{spectrometer}) \qquad (1.6)$$

Where BE is the binding energy of the electron relative to the chemical potential, $h\nu$ represents the energy of the X-ray photons irradiating the sample surface with h being the Plank constant and ν being the frequency of the electromagnetic radiation, $\Phi_{spectrometer}$ represents the work

function of the spectrometer, and KE is the kinetic energy of the electron as measured by the XPS instrument.

XPS instrument runs under ultra-high vacuum (~10^{-10}mbar) with magnetic shielding.[67] The X-ray beam can be generated from Al Kα, Mg Kα, or synchrotron source with a known *hv*. The X-ray photons then irradiate the sample surface and emit photoelectron. The ejected photoelectrons are filtered in hemispherical energy analyzers which disperse these electrons based on the measured KE. The work function term $\Phi_{spectrometer}$ is another known term in practice that accounts for a few eV of photoelectron KE absorbed by the detector. The BE of photoelectrons are then calculated from eq (1.6) and related to different elements and chemical states. Figure 1.10 shows the schematic of a typical XPS spectrometer.

XPS is a surface sensitive tool which makes it a suitable technique to study the CEI for cathode materials. Since the photoelectrons of interest in XPS have relatively low KE, the detection limit of the sample depth are usually limited to within 5 nm from the surface. To overcome this limitation, XPS depth profiling is enabled by combining XPS with ion sputtering with Ar^+ or other ion beams. In this type of experiments, XPS spectra is first recorded for the sample surface without any etching, then ion beam is applied to etch layers of the surface or surface contamination, revealing subsurface information. The etching time is tuned to control the etching depth. However, different samples may have different response to the etching so that the depth is often time an estimated number. In addition, the XPS sample preparation for most of the cathode materials needs to be down in Ar-filled glovebox because the CEI is extremely sensitive to air and water. In my PhD work, XPS was mainly used to characterize the chemical information of CEI and SEI in the cells. All XPS samples were transferred at ultra-high vacuum to avoid any contamination.

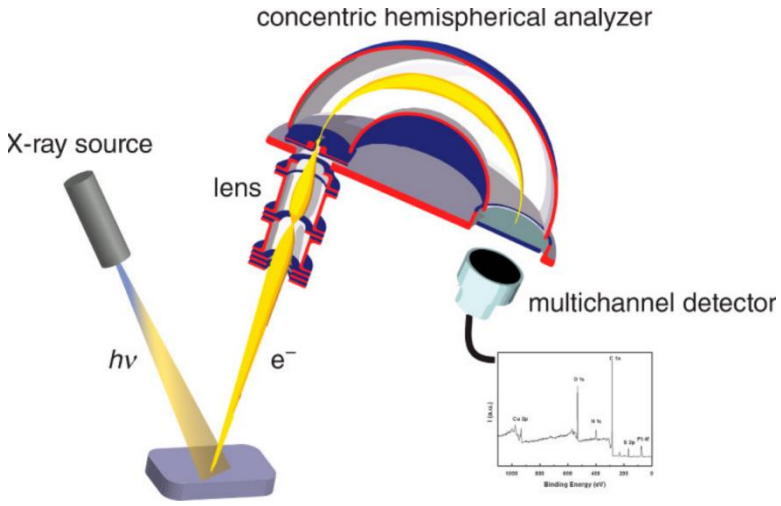

Figure 1.10 Schematic of a typical XPS spectrometer.[68]

1.4 Thesis Scope and Outline

Energy, especially electricity, is the foundation of the modern industrial society. Fossil fuels induce large amount of greenhouse gases emission during the electricity production and have limited remaining that's projected to run out within this century. As a result, there is a strong drive to developing cleaner and more sustainable energy sources such as solar and wind energy. Energy storage thereby becomes a heated topic due to the intermittent nature of these renewable energy sources. In addition, the world has experienced the rapid market growth of 3C electronic devices as well as EV industry in the past several decades. LIBs, as an energy storage device, can effectively bridge the disconnect between the intermittent renewable energy generation and the distribution of energy consumption. Compared to lead-acid and/or nickel-hydride batteries, LIBs provide more than a two-fold increase in terms of energy and power density, which makes them the most suitable choice for portable electronic devices and EVs. Ever since the commercialization

of LIBs, the scientific community has devoted to developing batteries with higher energy density, longer cycle life, lower manufacturing cost, and better safety.

Among all the cell components, cathode active material can take up to 40% of the cell cost and to a large extent determines the overall performance of the cell. Current generation of commercial batteries mainly uses LCO, NMC, NCA, or LFP materials as the cathode. The increasing price of Co and the relatively low practical capacity in LCO (~ 140 mAh g^{-1}) makes it less favorable in price-sensitive or energy-sensitive applications. LFP, although coming with low manufacturing cost, also only delivers about 150 mAh g^{-1} specific capacity, which cannot satisfy the demand of high energy batteries. The development of NMC layered materials (especially with high Ni content) thereby becomes the major direction in exploring high energy cathode materials since they can deliver over 200 mAh g^{-1} capacity. In addition, LRLO materials with much higher capacity (over 250 mAh g^{-1}) also attracted a lot of attention and are considered one of the most promising next-generation high energy cathode materials. These two materials both belong to the layered structure constructed by alternating Li layer and TM layer on top of each other. Compared to NMC materials containing only TM in the TM layer, LRLO materials have extra Li atoms occupying some of the 3a site within the TM layer. Despite the high capacity and high energy provided in NMC or LRLO, both suffer from material degradation as well as compromised cycling stability.

In this thesis, I mainly focus on understanding the degradation mechanisms of lithium transition metal layered oxides as cathode materials for LIBs. Different optimization strategies were also applied to the cathode materials and will be discussed in detail. A series of advanced characterization tools were applied in my study to understand the structure and/or interphase changes in layered oxide materials including XRD, NPD, PDF, XPS, extended X-ray absorption

fine structure (EXAFS), scanning transmission electron microscopy coupled with electron energy loss spectroscopy (STEM-EELS), nuclear magnetic resonance (NMR), scanning electron microscopy with energy dispersive X-ray analysis (SEM-EDX), and inductively coupled plasma (ICP).

My PhD thesis consists of 5 chapters. **Chapter 1** provides a general introduction to this thesis starting with the function mechanism for LIBs, followed by the structure and performance of different cathode materials. Specifically, the different degradation mechanisms and the corresponding advanced characterization tools for layered oxide materials are also included in the introduction.

In **Chapter 2**, we studied twin-boundary (TB) defect engineering as an effective strategy in mitigating the anisotropic volume expansion and addressing the capacity degradation in classical layered NMC materials. The radially aligned TB defects act as a rigid framework that mitigates anisotropic changes in NMC during cycling, thus lead to enhanced electrochemical performance.

In the following chapters, I will move forward to discuss LRLO materials, which delivers a high specific capacity over 300 mAh g^{-1} but suffers from both capacity and voltage fade. In **Chapter 3**, mild heat treatment was applied to cycled LRLO materials to recover the decayed voltage. Through various analytical tools, TM reordering and the recovery of honeycomb superlattice was identified as the key factor for the structure and voltage recovery. An ambient-air relithiation was also conducted along with the heat treatment to the cycled LRLO to regenerate both the voltage and capacity.

In **Chapter 4**, we shifted the research focus from cathode bulk properties to cathode-electrolyte interphases. Lithium bis-(oxalate)borate (LiBOB) was used as an electrolyte additive

to improve the cycling stability in high voltage LRLO/graphite full cells. The HF scavenger effect of LiBOB was identified through the characterization of B-F species in the cycled electrolyte. Due to less HF corrosion on both electrode interphases, a reduced amount of TM dissolution and redeposition on the graphite has been proved, thereby mitigating the capacity decay in LRLO/graphite full cells.

Chapter 5 as the last chapter summarizes the overall work and provides the perspectives for the future research.

Chapter 2. Mitigating Anisotropic Changes in Classical Layered Oxide Materials by Twin Boundary Defect Engineering

2.1 Introduction

Li-ion battery (LIB) technology holds the key to the future of electric vehicles (EVs) as cost, safety, driving range, and battery lifetime are determining factors of a user's experiences with EVs.[69] Among the existing cathodes in LIBs, $LiNi_xMn_yCo_{1-x-y}O_2$ (NMC) is one of the most popular choices in the EV market due to their high reversible capacity, good rate capability, and relatively low cost. Dahn's group showed that an NMC/graphite cell has the ability to power an EV for over 1 million miles, suggesting that driverless robotaxis, long haul trucks, and city buses can be potentially powered by batteries.[70] The energy density in NMC can be further improved by delithiating the cathode using a higher voltage cutoff (>4.5 V), but the inherent structural instability of NMC in such a highly delithiated state will accelerate material degradation and compromise the cycle life.[71,72] For instance, highly delithiated NMC yields large amounts of Ni^{4+} with high reactivity, which easily reduces to the more stable rocksalt-like NiO structure (especially on the surface of the particles), hindering Li diffusion pathways as cycling proceeds.[32,33] Parasitic side reactions between the electrode and electrolyte are also accelerated in high voltage such as HF corrosion on electrode-electrolyte interphases and transition metal (TM) dissolution from NMC and redeposition on the graphite.[3773] Furthermore, anisotropic volume expansion (contraction) in NMC during Li intercalation (deintercalation) leads to disintegration and contact loss between the cathode active material, conductive carbon black, and the current collector at high voltage.[74] Additionally, cracks can form within the NMC secondary particles and propagate through the primary particle boundaries.[75] Such progressive intergranular separation results in the eventual loss of electrical contact, which promotes infiltration of electrolyte along the grain

boundaries into the particle interior and accelerates surface degradation as well as Li inventory loss, eventually leading to the capacity fade.

Over the past few decades, diverse strategies have been adopted to overcome some of these disadvantages in NMC, including lattice doping, surface modification, tuning the material composition, synthesizing in single crystals forms, and building concentration gradient architectures.[32,70,76,77] However, designing structure defects in NMC such as controlled twin boundaries (TB) were often time neglected as a mitigating strategy to achieve better cycling performance. In this work, the unique properties of controlled TB defects in the as synthesized NMC layered materials will be studied in the following sections, especially the enhanced surface stability and structure robustness in NMC at high voltage cycling. Previous literature mainly focused on the negative effects of many different types of defects generated during electrochemical cycling. For example, Li/Ni mixing (or named as Li/Ni anti-site defect) is a common defect in layered materials which hinders Li transport during cycling and causes capacity decay.[78] At high voltage cycling, the formation of dislocation network was also reported in Li-rich NMC layered oxides and recognized as one of the origins for voltage fade.[34] Stacking faults (SF, lateral displacements of the layers) are also reported to cause sluggish Li diffusion in layered oxides and lead to electrochemical irreversibility over cycling.[79] In addition, anti-phase boundaries (APB) and TB were reported to propagate after cycling, resulting in the increase of cation disordering and increased resistance for Li ion extraction and intercalation.[80]

Although SF, APB, and TB are often time mentioned together and reported to hinder Li diffusion in the cycling, these three defects are intrinsically different and their influence on the electrochemical performance should be viewed separately. Figure 2.1 shows the schematics comparing these three defects. Figure 2.1a shows a layered NMC structure without defects, where an ABCABC oxygen stacking sequence presents, known as O3 phase. In O3 phase, the LiO_6 octahedra share edges with the TMO_6 octahedra.[81] However, the ABCABC stacking sequence may be disordered during synthesis or at highly delithiated state due to layer gliding.[82] These regions with lateral displacements of the layers are SF. Figure 2.1b gives an example of O1-like SF, where BCBC stacking appears as part of the structure. In this SF region, the LiO_6 octahedra and TMO_6 octahedra are face-sharing in this SF region. The altered O1 stacking near SF can act as a

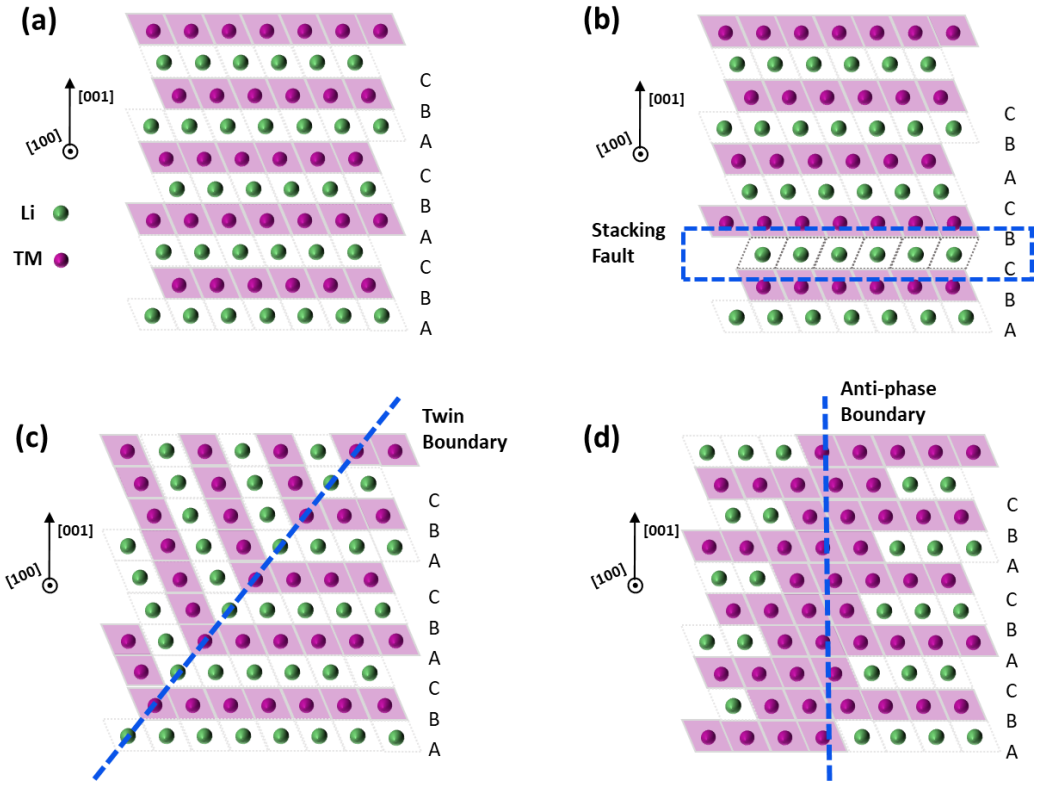

Figure 2.1 Side-view schematics of layered oxide crystals without defects and with different types of defects. a) No defects; b) stacking fault defect; c) twin boundary defect; d) anti-phase boundary defect. Li ions are green circles and TM ions are purple circles. LiO6 and TMO6 octahedra are depicted as parallelograms with Li or TM in the center.

preferential nucleation site for rock-salt transformation and lead to electrochemical irreversibility.[79] [82] This O3 to O1 phase transition leads to the fast capacity decay in NMC materials.[16] Similar behavior was also reported in sodium-ion intercalation compounds as the P2-O2 phase transition and the related poor material durability.[83] In comparison, the ABCABC stacking sequence are well preserved on both sides of the TB or APB, as depicted in Figure 2.1c and 2.1d. Figure 2.1c shows a crystallographic TB, a plane of lattice points where the grains on two sides of the TB possess mirror symmetry. Figure 2.1d shows an APB where a translation shift along the c direction separates the structure into two sides. The translation shift causes the Li layer at one side of APB to be continued with the TM layer at the other side of the APB. APB decreases local Li diffusion coefficient and increases cathode impedance since it hinders the Li diffusion pathway along the (003) planes.[84] In comparison, the Li diffusion pathway is still well connected along the two sides of the TB in NMC.

Among the defects discussed above, TB is a unique defect type that does not hinder the Li diffusion and can potentially be beneficial to the electrochemical performance in NMC. In previous literature reports, defects are mostly observed after cycling or exists at pristine state and then largely increase after cycling. Thus, the generation of defects are usually correlated with the cell performance decay in NMC materials. In this work, however, we report a novel strategy of utilizing highly coherent TB defects to mitigate the structural and performance degradation in NMC particles. The detrimental defects reported in the literature are usually heterogeneous and the formation of the defects are not well controlled. In contrast, the TB defects reported in this work is introduced to the pristine material by designing and fabricated through a controlled synthesis, thus functioning as a mitigating strategy in improve the cycling stability of NMC materials.

The designed TB defects in this work are created through a polyol synthesis method in a series NMC nanoparticles such as $LiNi_{1/3}Mn_{1/3}Co_{1/3}O_2$ (TB-NMC111), $LiNi_{0.4}Mn_{0.4}Co_{0.2}O_2$ (TB-NMC442), and $LiNi_{0.6}Mn_{0.2}Co_{0.2}O_2$ (TB-NMC622). Despite the vast number of studies conducted for layered oxide cathode materials, TB defects have not been reported much in the literature because their presence and abundance heavily depend on the synthesis method to produce the material. For example, in hydroxide co-precipitation, precursors obtained from the reaction are TM hydroxides with a hexagonal ($P\bar{3}m1$) crystal structure. During heat treatment, the precursor will eventually transform into a layered structure ($R\bar{3}m$), but the two structures – hexagonal ($P\bar{3}m1$) and rhombohedral ($R\bar{3}m$) – should be compatible with each other since they both belong to the same trigonal crystal system. This compatibility may reduce the chance to form twins during the phase transition. In contrast, during polyol synthesis, precursors obtained from the initial reaction consist of Ni-Co alloys with a cubic structure.[85] Although they also transform into the layered structure ($R\bar{3}m$) during heat treatment, polyol-synthesized NMC goes through a unique phase transition from cubic ($Fm\bar{3}m$) to rhombohedral ($R\bar{3}m$), which are the structures with much less compatibility. In addition, the phase transformation for polyol synthesis is accompanied by particle size growth from around 5 nm to 138 nm. It is likely that twins in TB-NMC materials form during this particular phase transformation and particle size growth process.

Using scanning transmission electron microscopy (STEM), we analyzed the crystallographic structure at TBs and the types of surface facets that formed adjacent to the TBs. Our results show that radially-aligned TBs observed in TB-NMC materials can maximize the presence of the (003) plane in pristine particles, which is more stable than other planes. Furthermore, the structural changes observed using *operando* XRD verify that TB-NMC442 experiences less *c*-lattice expansion and contraction during charge and discharge. Our results

suggest that the rocksalt-like region formed along the TBs can serve as a rigid framework that mitigate the changes in the *c*-lattice during cycling. As a result, TB-NMC materials show enhanced electrochemical performance with better long-term cycling retention compared to commercial NMC samples.

2.2 Experimental Methods

2.2.1 Electrochemistry

Synthesis of TB-NMC nanoparticles was carried out following a procedure detailed in a previous study.[85] Using tetraethylene glycol (Aldrich) solvent, all the transition metal acetates - $(NiCH_3COO)_2{\cdot}4H_2O$ (Acros), $(MnCH_3COO)_2{\cdot}4H_2O$ (Acros), and $(CoCH_3COO)_2{\cdot}4H_2O$ (Acros)– and $LiOH{\cdot}H_2O$ (Sigma-Aldrich) were mixed with citric acid (Sigma-Aldrich). All the salt precursors were dissolved when the mixture was heated to 230°C for 3 h in a round-bottom flask connected to a reflux. Once the mixture cooled down to room temperature, the precipitate was washed with ethanol, dried overnight, and heat-treated at 450°C for 12 h in air. The powder was then ground with agate mortar and pestle, pelletized, and then heat treated at 850°C for 5 h in air. Commercial NMC442 and commercial NMC622 (Toda) powder was heated to 500°C in air to remove proton-containing surface species.[86] All the NMC powders were stored in an Ar-filled glovebox (MBraun, <1ppm H_2O). Table 2.1 summarizes the coin cell configuration used for our study. For both TEM and FIB characterization, all cells were cycled at a rate of C/10. For long-term electrochemical results, C/10 was used for the first two formation cycles, while a rate of 1 C or C/3 was used for subsequent cycles. Cycling was performed in the voltage range of 2.5 - 4.7 V with the theoretical capacity defined as 200 mAh g^{-1}. The galvanostatic cycling tests were conducted with an Arbin BT2000 cycler (Arbin instruments, USA).

Table 2.1 NMC/Li half cell coin cell testing specifications.

Active material	NMC – 80 %
Conductive agent	SPC65 – 10 %
Binder	HSV900 – 10 %
Counter electrode	Li metal chip (Thickness: 1 mm, diameter: 15.4 mm)
Separators	Celgard 2325
Electrolyte type	1M $LiPF_6$ in EC:DMC = 3:7 vol. %
Electrolyte amount	55 µl
Cell type	CR2032
Coin cell setup	0.5 mm-thick spacer and one spring at the anode side
Voltage range	2.5 - 4.7 V
Test protocols	Rest for 6 h after assembling, then 20 mA g^{-1} (C/10) for first 2 cycle, the rest cycling at 66.7 mA g^{-1} (C/3) or 200 mA g^{-1} (1C) at room temperature

2.2.2 Material Characterization (TEM, FIB, SEM, XPS, ICP, XRD)

High-resolution STEM images for NMC442 and NMC111 materials were taken using the double aberration-corrected scanning TEM (TEAM 0.5) at the Molecular Foundry at Lawrence Berkeley National Laboratory. The STEM was operated at an acceleration voltage of 300 kV. All annular dark-field STEM micrographs were recorded with a convergence angle of 30 mrad and a probe size of < 1 Å after fine-tuning of the probe corrector at 300 kV. High-resolution STEM images for 622 material was performed on JEOL JEM-ARM300CF at 300 kV, equipped with spherical aberration correctors. The morphologies of the particles were identified using a Zeiss Sigma 500 scanning electron microscope (SEM) with an accelerating voltage of 5 kV. Cross-sectional images of commercial NMC were collected from focused ion beam (FIB) using the FEI Scios™ DualBeam™ FIB. The chemical composition of NMC materials were confirmed by ICP-MS (iCAP RQ, ThermoFisher Scientific) and listed in Table 2.2 and Table 2.3. X-ray

photoelectron spectroscopy (XPS) was performed using a Kratos AXIS Supra with an Al anode source operated at 15 kV. High-resolution spectra were calibrated using the hydrocarbon C 1s peak at 284.5 eV. Lab-based X-ray diffraction (XRD) was collected on Rigaku SmartLab Diffractometer with Cu Kα source. *Operando* XRD experimental details will be shared in the following section.

Table 2.2 ICP-MS result of the NMC442 Cathode.

Sample	Ni : Mn : Co	Li : (Ni+Mn+Co)
TB-NMC442	0.400 : 0.400 : 0.200	1.008:1
Commercial NMC442	0.396 : 0.398 : 0.206	1.034:1

Table 2.3 ICP-MS result of the NMC622 Cathode.

Sample	Ni : Mn : Co	Li : (Ni+Mn+Co)
TB-NMC622	0.590 : 0.196 : 0.214	1.035:1
Commercial NMC622	0.610 : 0.198 : 0.193	1.062:1

2.2.3 Operando X-ray Diffraction

Electrode pellets were prepared by mixing the NMC powders with carbon black (Timcal Super C65) and polytetrafluoroethylene (PTFE) powder (Sigma-Aldrich, 1 μm particle size), in a 7:1:2 weight ratio. Approximately 6 mg of the mixture was pressed in a 3 mm diameter die to form ~400 μm-thick pellets. The NMC electrode pellets were assembled into modified RATIX electrochemical cells[87] using lithium foil (MTI Corp) as

a counter electrode, and two layers of glass fiber (Whatman GF/B) as the separator. The electrolyte used was 1 M $LiPF_6$ dissolved in a mixture of ethylene carbonate (EC) and dimethyl carbonate (DMC) in a 1:1 volume ratio (Sigma-Aldrich). All preparations were carried out in an argon-filled glovebox containing <1 ppm O_2 and H_2O. Electrochemical measurements were carried out at a rate of 18.58 mA g^{-1} of NMC between 4.8 and 2.7 V, with a 2 h potentiostatic hold at each voltage limit followed by a 2-hour rest period (Bio-logic BCS-810).

Operando synchrotron X-ray diffraction data were recorded during electrochemical measurements using high-energy X-rays (λ = 0.1668 Å) provided by beamline 28-ID-1 at the National Synchrotron Light Source II (NSLS-II) at Brookhaven National Laboratory. Each diffraction image was obtained from a 30 s summed exposure recorded in transmission geometry as the electrode was scanned horizontally in transverse mode, gauging the whole diameter of the electrode. XRD patterns were obtained from integration of the images using the GSAS-II software[88] and using LaB_6 (NIST SRM 660c) as a standard for calibration.

2.2.4 Refinements

Rietveld refinements to the XRD data (pristine state) were performed with Topas-Academic V6 using a model based on the $R\bar{3}m$ space group, with TM site (3a) and O site (6c) occupancy based on the nominal composition, and Li site (3b) occupancy based on the electrochemical data. Refined parameters included lattice parameters (*a*, *c*), Li-Ni antisite mixing (3a-3b site exchange), O *z* coordinate, scale factor, isotropic atomic displacement parameters (B_{iso}) for TM and O (fixed to 1 $Å^2$ for Li). Background and additional peaks from the glass tube container and PTFE additive were fit using a 6-coefficient Chebyshev polynomial function and a pseudo-

Voigt function, respectively. The lattice parameters during cycling were obtained from LeBail refinements using the $R\bar{3}m$ space group and the same peak profile function as the one used for the Rietveld refinement. The refined parameters for pristine NMC442 and NMC622 samples are shown in Table 2.4 and Table 2.5.

Table 2.4 Lattice parameters, degree of Li/Ni cation mixing, and R factors from Rieveld refinement for NMC442 syncrotron XRD patterns.

Sample	TB-NMC442	Commercial NMC442
a = b (Å)	2.86868(4)	2.87265(2)
c (Å)	14.2304(3)	14.2692(1)
V (Å^3)	101.417(4)	101.975(2)
O z coord.	0.2589(1)	0.25841(6)
Ni-Li mixing	0.0566(8)	0.0510(5)
R_{wp} (%)	3.470	2.233

Table 2.5 Lattice parameters, degree of Li/Ni cation mixing, and R factors from Rietveld refinement for NMC622 XRD patterns.

Sample	TB-NMC442	Commercial NMC442
a = b (Å)	2.8704(3)	2.8692(3)
c (Å)	14.2301(2)	14.2407(2)
V (Å^3)	101.797 (1)	101.534(2)
O z coord.	0.2437(1)	0.2480(1)
Ni-Li mixing	0.053(3)	0.048(3)
R_{wp} (%)	1.957	2.807

2.3 Results and Discussion

2.3.1 Twin Boundary Defects in Pristine TB-NMC

Nanosized TB-NMC111, TB-NMC442, TB-NMC622 materials are synthesized with a polyol method as described in the Experimental Section. The high-angle annular dark-field (HAADF)-STEM images of the TB-NMC materials are shown in Figure 2.2. The STEM images are taken along the [010] zone axis and exhibits the bonding of two domains across a (104) plane, forming an atomically sharp boundary that can be universally observed in three NMC materials with different compositions. Each domain has the well-defined layered structure as seen in the literature.[89] The interface, as marked by the blue dotted line in Figure 2.2a, 2.2f, and 2.2g, was identified as a crystallographic TB. In TB-NMC materials, TB forms in a radial direction, extending from the center to surface of the particle with two (003) planes from the two domains converging to form a 110º angle. Here we want to point out that this 110º angle is related to the intrinsic angle between the (003) and (104) plane in a layered structure, which is 55º. The two (003) planes from the two sides of the (104) plane TB cause the angle between the two (003) planes to add up to 110 º. This 110 º angle was also observed in other TB in layered oxide reported previously.[80,90] The symmetry along the TB was further confirmed by Fourier transform (FT) images obtained in two areas (indicated by (i) and (ii) on Figure 2.2a). The results were compared to the simulated diffraction patterns of $LiCoO_2$ (LCO) with zone axis of [010] and $[0\bar{1}0]$ since NMC has the same space group ($R\bar{3}m$) and similar lattice parameters as those of LCO.[91] The FT images in Figure 2.2b and 2.2c match closely with the simulated diffraction patterns in Figure 2.2d and 2.2e, respectively, confirming the 180º rotational symmetry observed in the STEM image.

Figure 2.2h, the Fourier-filtered image of Figure 2.2a, more clearly illustrates the atomic structure formed along the TB. At the bottom of this image, the line intensity profile that runs across the TB

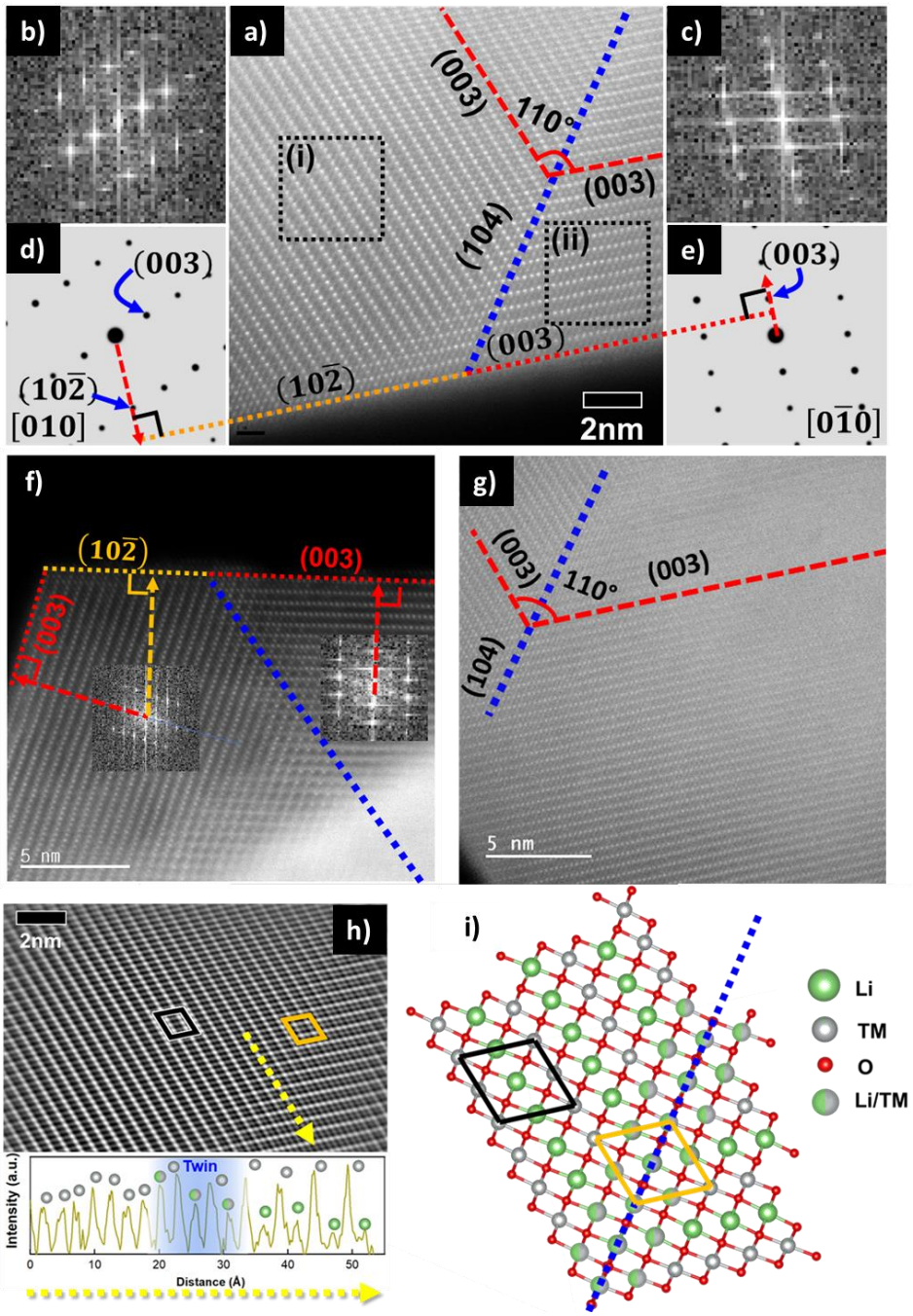

Figure 2.2 a) STEM image of a TB-NMC442 particle. The angle between two (003) planes (indicated by red dotted line) divided by the twin boundary (TB, blue dotted line) is 110°. Comparison of Fourier transform patterns from b) region (i) and c) region (ii) (as shown on Figure 1a) and simulated diffraction patterns of $LiCoO_2$ with d) [010] and e) [0$\bar{1}$0] zone axis. f) STEM image of a TB-NMC111 particle. g) STEM image of a TB-NMC622 particle. h) Fourier filtered image of Figure 1a, which clearly exhibits transition near the TB. i) Atomic structure near the TB indicated by blue dotted line. Black and orange boxes in h) and i) indicate unit cells without and with cation mixing, respectively. Cation disordering is schematically represented as split color circle of Li (green) and TM (grey).

was collected along the yellow arrow. High and low intensity peaks in the line profile represent the location of TM and Li, respectively; the difference in atomic mass between them leads to Z-contrast. Following the yellow arrow starting on the left domain of the TB, similar intensity peaks are observed at about 2.5 Å spacing since the arrow is on the (003) plane. As the line profile approaches the TB, each alternating peak decreases in intensity as more Li starts to occupy the alternating TM location. Such disordering is gradually alleviated past the TB where Li and TM are then alternatively arranged on the $(10\bar{2})$ plane. Severe cation disordering observed on the TB and the sites adjacent to it can be viewed as a phase transition, as illustrated by the unit cells denoted by the orange boxes in Figure 2.2h and 2.2i. The atomic structure in the orange box is comparable to the rocksalt structure. This rocksalt-like phase clearly contrasts with the pristine layered structure observed in a unit cell located away from the TB (denoted with a black box in Figure 2.2h). The cation disorder observed here is different from the cation disorder frequently observed in layered oxide materials (after high-voltage cycling, which is confined to the few atomic layers at the surface of particles).[92] Here, a few atomic layers of the rock-salt like phase are aligned radially, propagating from the center to the surface of the particle along the TBs.

It is important to note that the formation of TBs is a universal phenomenon in classical layered oxides synthesized by the polyol method. The existence of TB has been confirmed by the STEM images from three different TB-NMC compounds (NMC442, NMC111, and NMC622) in Figure 2.2a, 2.2f, and 2.2g, as well as more particles sharing the same traits in Figure 2.3 with both high and low meg STEM images. All the TBs are formed in the radial direction and the presence of rocksalt-like phase along the TB are observed. The facet planes near the TB on TB- NMC442 were identified as $(10\bar{2})$ and (003) by their reciprocal vectors on Figure 2.2d and Figure 2.2e (as indicated by red dotted arrows). Other TB-NMC particles in Figure 2.2f and Figure 2.3 all provide

similar observations, showing that TB-NMC particles are commonly terminated with $(10\bar{2})$ and (003) planes. It is generally accepted that TBs form in the material in order to minimize the total surface energy per volume; studies by Howie and Marks showed that TBs lead to the surface with even lower energy than surfaces developed by the Wulff construction in nano crystallites.[93–95] Thus, the observed surface facets exposed due to TBs, $(10\bar{2})$ and (003), are low surface energy facets in layered oxide materials. According to a previous report, (003), (104), and $(10\bar{2})$ for LCO (whose crystal structure is identical to NMC), all have a low surface energy of ~1 J/m^2 in contrast to planes such as (110) and (100), which have higher surface energies of 2.41 J/m^2 and 2.943 J/m^2, respectively.[96] The similarities in surface energy values between LCO and NMC are expected due to their structural similarities. A few regions without TBs in NMC442 particles were also observed as shown in Figure 2.4. Here, without TBs, the particles display facets with high order planes such as $(1\bar{1}8)$, $(1\bar{1}2)$, and (107), which are correlated with higher surface energies.[97] In summary, TB is universally present in polyol synthesized NMC materials. TB-NMC particle surface is more likely terminated with low surface energy planes such as (003) and $(10\bar{2})$ with limited structural degradation, which will be further discussed in the following sections.

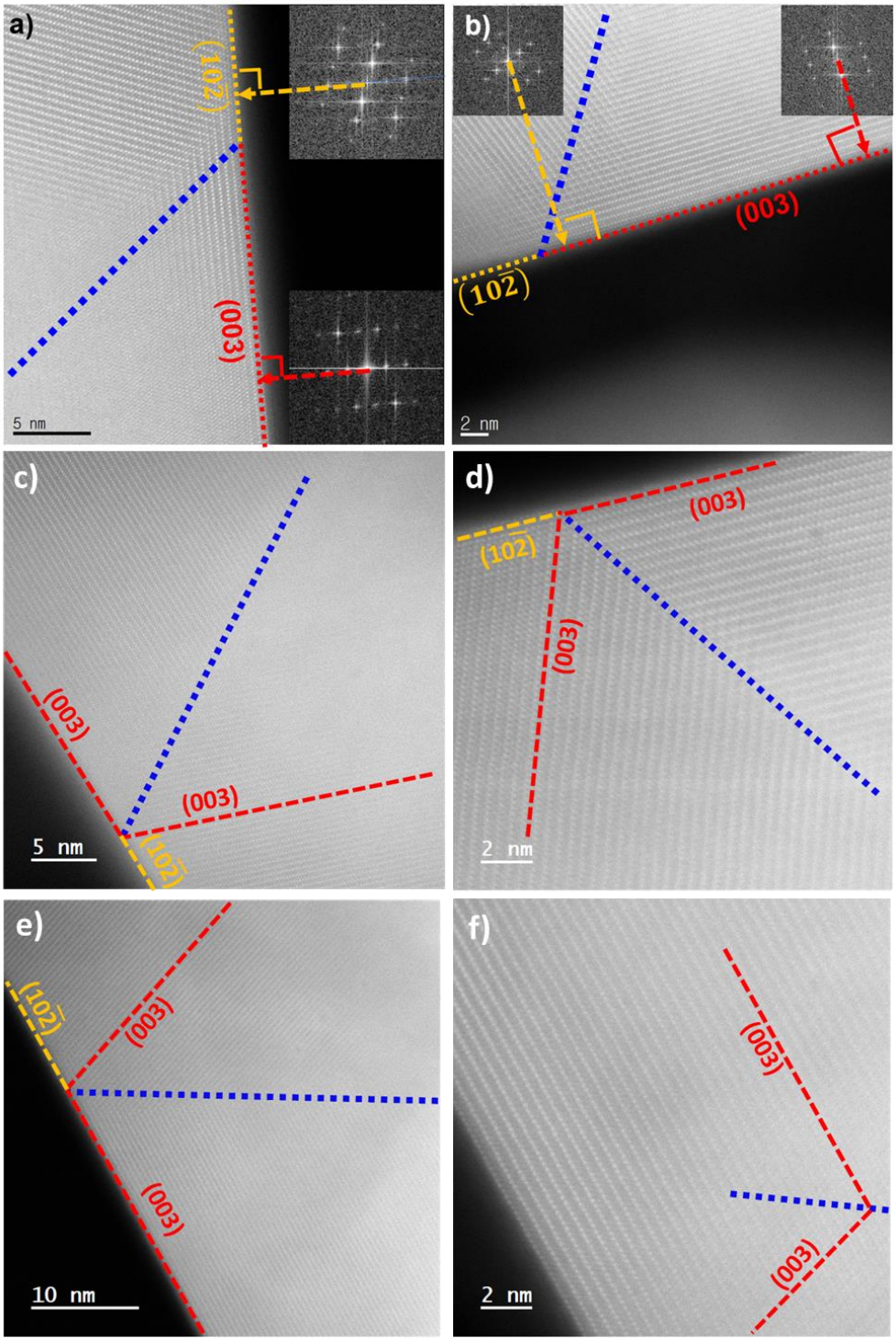

Figure 2.3 More STEM images of TB-NMC with the twin boundary marked with a blue line. a) and b) TB-NMC442, c)- f) TB-NMC622. The surfaces of the particles were terminated by (003) and $(10\bar{2})$ planes.

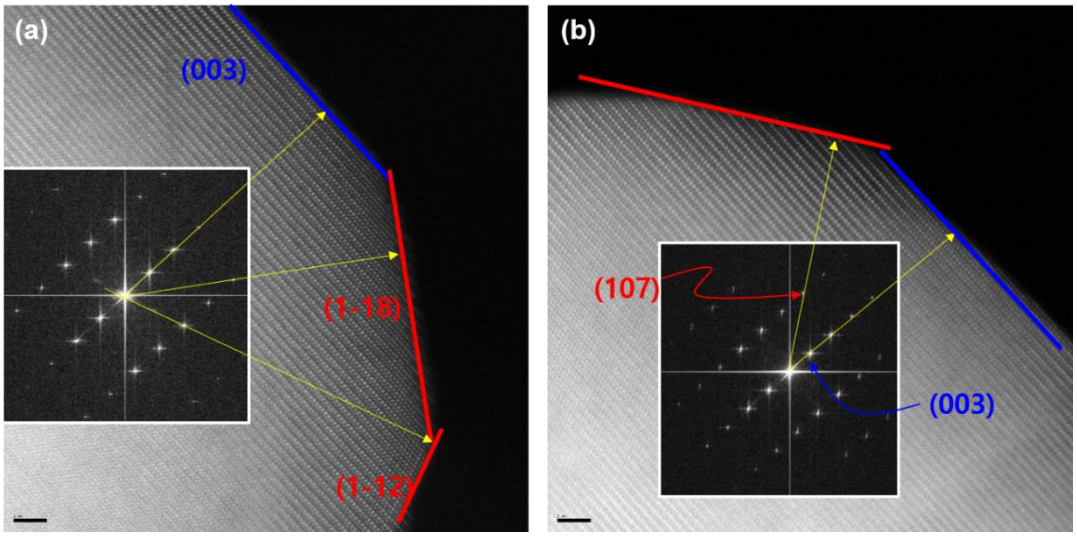

Figure 2.4 Two STEM images of areas without a twin boundary in TB-NMC442. The insets show the FFT images of the particles. The FFT patterns confirm that surfaces of the particles were terminated by (a) (003), $(1\bar{1}8)$, and $(1\bar{1}2)$ planes and (b) (003) and (107) planes.

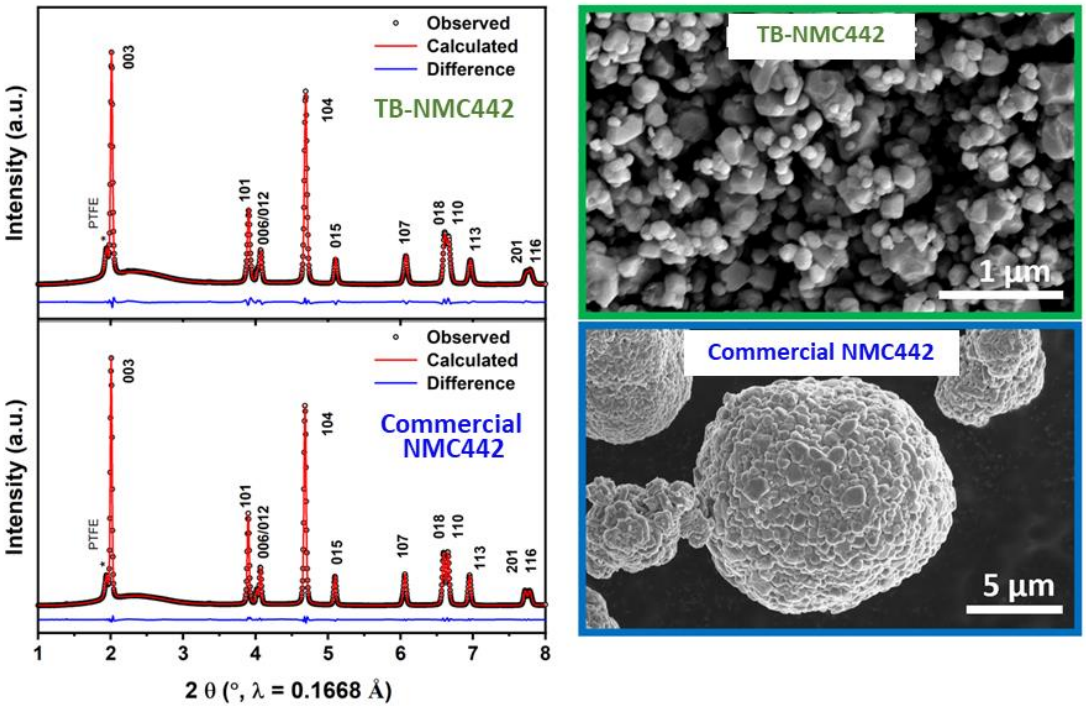

Figure 2.5 Rietveld refinements of high-resolution synchrotron XRD data and the corresponding morphology of the pristine electrode mixture prepared with TB-NMC442 (top, green) and commercial NMC442 (bottom, blue), respectively.

2.3.2 Electrochemical Performance Comparison

To evaluate the performance of the NMC material with the controlled TB defects, TB-NMC442 and a commercially available NMC442 were first tested and compared. SEM images of both samples are shown in Figure 2.5. TB-NMC442 has a dispersed nanoparticle morphology without agglomeration while commercial NMC442 consists of tightly packed micro-sized aggregates. Both TB-NMC442 and commercial NMC442 were tested with a high voltage cutoff (2.5 – 4.7 V) and the results are shown in **Figure 2.6**. Such a high voltage cutoff is used to evaluate the material stability near the completely delithiated state (theoretical capacity ≈ 274 $mAh \cdot g^{-1}$). As expected, both materials show the typical behavior of layered oxide materials at high voltage cutoffs: high initial capacity but rapid capacity decay with prolonged cycling.[71] Initially, TB-NMC442 has a charge capacity of 284 mAh g^{-1} compared with a capacity of 250 mAh g^{-1} for commercial NMC442. Since TB-NMC442 is a nano-sized material, it has a relatively large surface area of 2.83 m^2 g^{-1}, which is 5 times larger than commercial NMC442 (0.5 m^2 g^{-1}).[98] Thus, more CEI may form in the first cycle and contribute to additional charge capacity in TB-NMC442. In addition, a small plateau above 4.5 V in the first charge curve can be observed in TB-NMC442. It is suspected that a high concentration of TB defects in TB-NMC442 activates a small amount of oxygen redox in the structure which can be induced by the possible Li-O-Li configurations along the TB.[99] In summary, the side reactions with the electrolyte due to the large surface area and the potential activation of oxygen redox or oxygen gas release would contribute to the additional first charge capacity of TB-NMC442, but it remains mainly irreversible as both samples show a similar first discharge capacity (214 mAh g^{-1} for TB-NMC442 and 209 mAh g^{-1} for commercial NMC442).

When both NMCs were repeatedly charged and discharged for a long time with high voltage cutoff, TB-NMC442 shows much improved capacity retention compared to commercial

NMC442, especially at high C-rate. After 100 cycles, TB-NMC442 retains a capacity of 116 and 124 mAh g^{-1} at C/3- and 1 C-rate, respectively, compared to 98 and 85 mAh g^{-1} for commercial NMC442. Moreover, an average efficiency of 99.7% (from the 3rd to the 100th cycle) of TB-NMC442 compared to 99.4 % of commercial NMC442 is observed at 1 C-rate.

The cycling stability improvement is again universally seen in TB containing materials. Figure 2.7 provides the XRD and SEM for pristine NMC622. Similar to the TB-NMC442 sample, TB-NMC622 are nano particles with 50~200 nm grain size, while commercial NMC622 are micro-

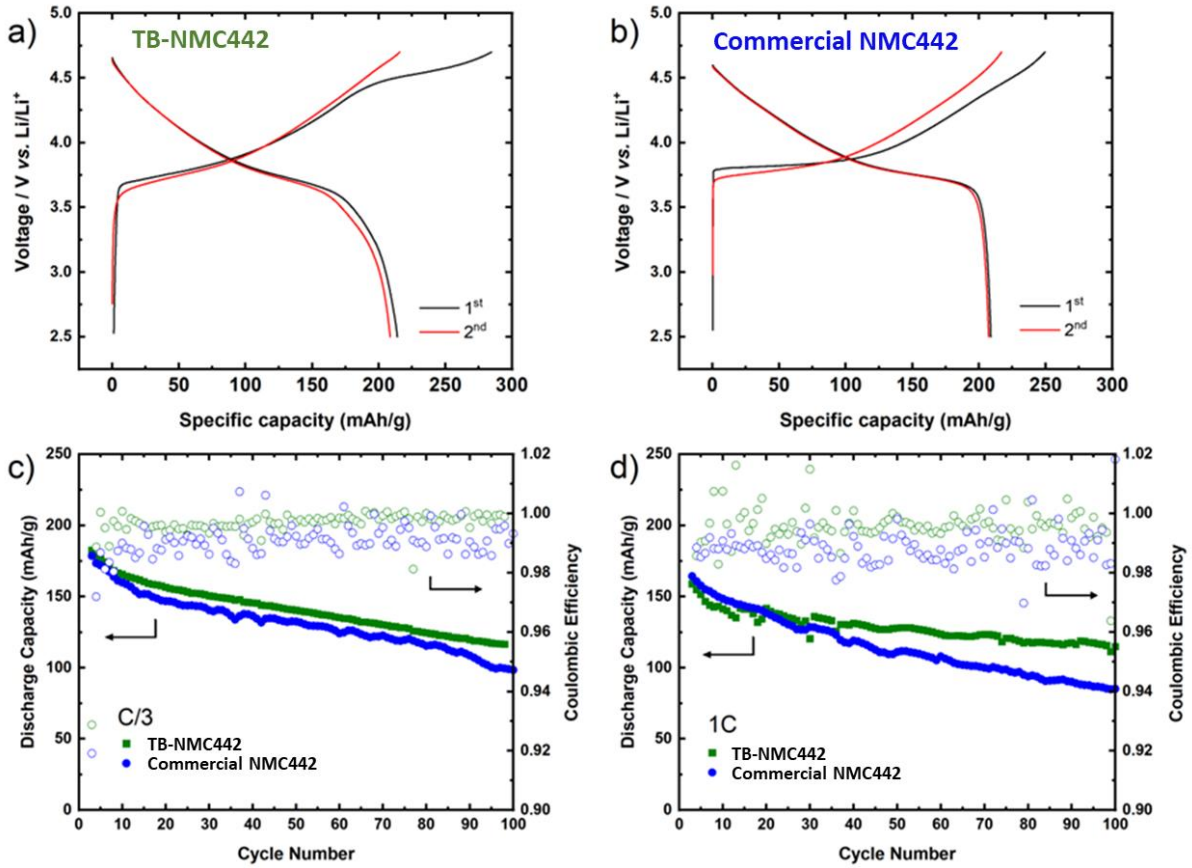

Figure 2.6 Electrochemical performance of TB-NMC442 and commercial NMC442. a, b) Respective voltage profile of the first and second cycle and c, d) Respective cycling performance in the voltage range of 2.5-4.7 V.

sized polycrystalline spherical particles. Rietveld refinement was applied to the XRD pattern for both TB-NMC622 and commercial NMC622 and the detailed parameters are listed in Table 2.5, showing that both samples have a pure phase which can be well indexed to $R\bar{3}m$ space group. Figure 2.8 compares the electrochemical performance for TB-NMC622 and commercial NMC622. At initial cycle, TB-NMC622 delivers a discharge capacity of 184 mAh g^{-1} and commercial NMC622 delivers a discharge capacity of 186 mAh g^{-1}. After 500 cycles, 14.8~14.9% higher capacity retention is seen in TB-NMC622 compared to commercial NMC622 with both C/3-rate and 1 C-rate. In addition, an average Coulombic efficiency at 99.0% (from the 3rd to 500th cycle) is observed in TB-NMC622 at 1 C-rate, compared to 98.7% in commercial NMC622. The electrochemistry data in NMC622 shows that an improved cycling stability is observed in TB-NMC622 compared to commercial NMC622, in phase with the NMC422 data.

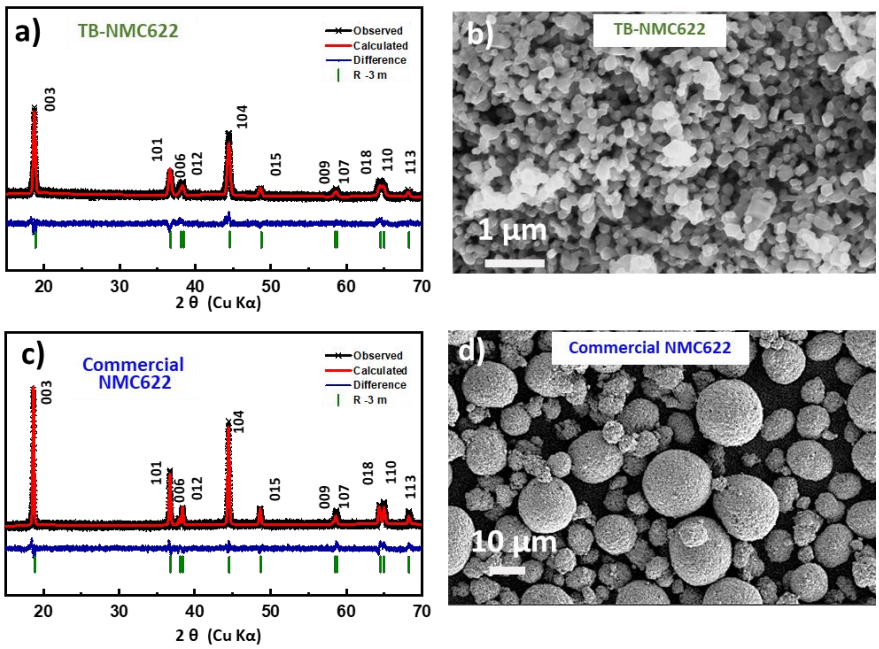

Figure 2.7 Rietveld refinements of XRD pattern and the corresponding morphology of the pristine NMC622 samples. a) and b) TB-NMC622; c) and d) commercial NMC622.

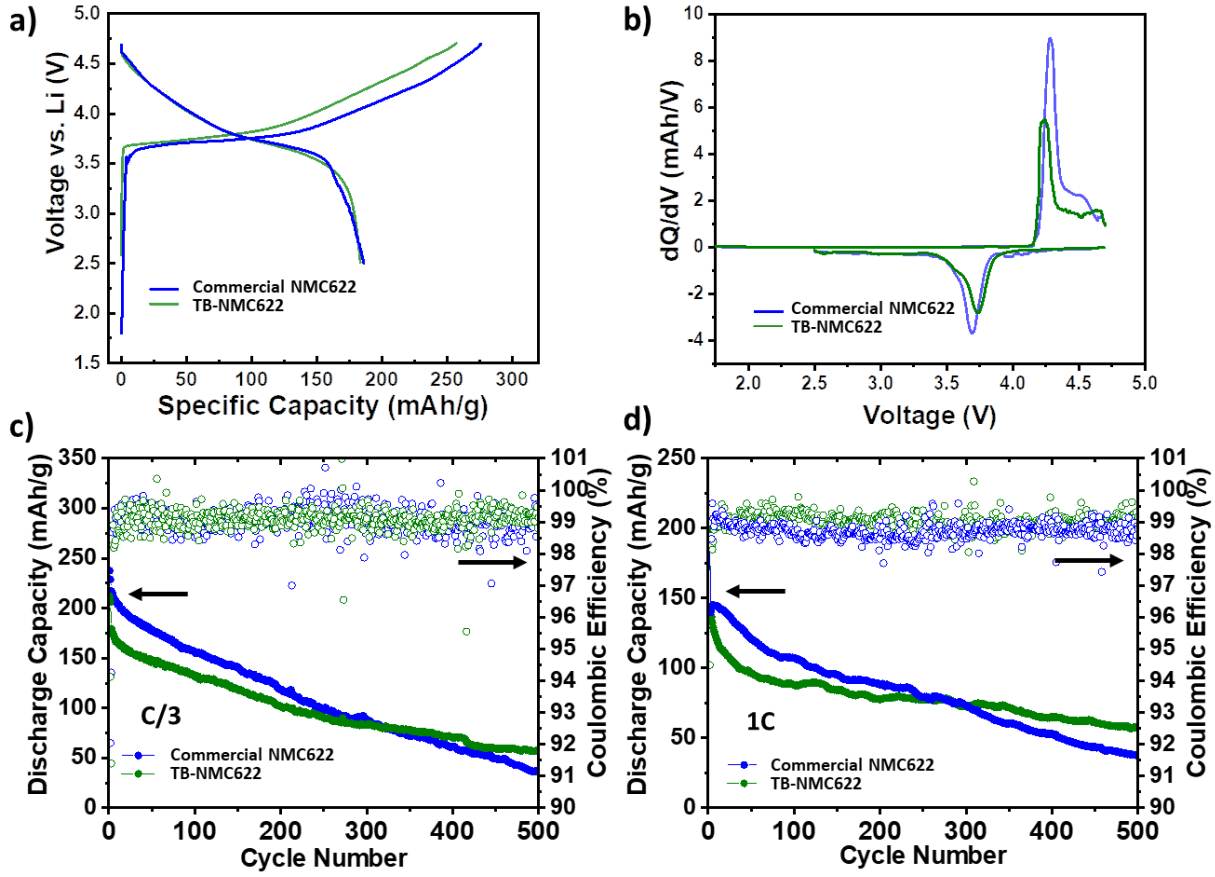

Figure 2.8 Electrochemistry performance of TB-NMC622 and commercial NMC622 in the voltage range of 2.5-4.7 V. a) the charge-discharge voltage profile of initial cycle at C/10-rate, cells continued with 1 C cycling as shown in figure c; b) dQ/dV plot of the initial cycle; c) capacity and Coulombic efficiency of NMC622 over 500 cycles at C/3-rate; d) capacity and Coulombic efficiency of NMC622 over 500 cycles at 1 C-rate.

Traditionally, it was reported that a high concentration of defects and increased side reactions with the electrolyte adversely affect the electrochemical performance of the material. However, the enhanced electrochemical performance for TB-NMC indicates that there are other factors that need to be considered to depict the full picture. Our hypothesis for improved cycling performance in TB-NMC comes from TB's effects on both the surface reconstruction and the bulk structure evolution. Firstly, as shown in the STEM analysis earlier, radially aligned TBs in TB-NMC442 increase the exposure of surfaces terminated by (003) planes and thus limit the degree

of structural degradation on the surface. Surface reconstruction from a layered to a rock-salt like structure is a common degradation pathway in layered oxides. Studies suggest that more severe reconstruction is observed from surfaces terminated with non-(003) planes or when Li diffusion channels are exposed to the electrolyte.[71,100] The degree of reconstruction on the surfaces terminated by the (003) plane, on the other hand, are much more limited (only 2-3 atomic layers). Our study is consistent with such expectations that minimal surface reconstruction was observed for cycled TB-NMC442 samples.[85] Furthermore, TBs in TB-NMC442 can affect bulk structural evolution as discussed in more detail in the following section.

2.3.3 Structural and Morphological Evolution in TB-containing NMC

Synchrotron XRD (sXRD) and Rietveld refinement was performed on both TB-NMC442 and commercial NMC442 electrodes, as shown in Table 2.4 and Table 2.5. For both samples, all peaks can be indexed to the α-$NaFeO_2$-type structure (with $R\bar{3}m$ space group) or to the PTFE binder additive. The refined lattice parameters of TB-NMC442 have a slightly smaller *a* and *c* lattice parameter – *a* of 2.86868(4) Å and *c* of 14.2304(3) Å – compared to *a* of 2.87265(2) Å and *c* of 14.2692(1) Å in commercial NMC442. A slightly larger degree of Li/Ni mixing of 5.66(8)% for TB-NMC442 was also observed compared to the 5.10(5)% of commercial NMC442. After the characterization of the pristine states, both NMC samples were charged to 4.8 V and discharged to 2.7 V with *operando* sXRD. Figure 2.9a and 2.9c are 2D image plots of the 003 and 110 reflections during the first charge-discharge cycle, which are strong indications for the lattice changes occurring along the *c*- and *a*-directions, respectively. Consistent with previous studies of other layered oxides,[101] the (003) peak shifts to higher angles during charge as oxygen atoms in TM layer repulse with one another after Li diffuses out of the structure. Meanwhile, the *a*-lattice

contracts at a high state of charge, consistent with other low-Ni content NMCs observed in the literature.[101]

Figure 2.9b and 2.9d represent the relative changes in the refined lattice parameters and the total volume (obtained from LeBail refinements) as a function of the specific capacity obtained from the electrochemistry data for both NMC442 materials**.** Nonetheless, both results confirm that TB-NMC442 experiences less relative *c*-lattice expansion and contraction during the charge and discharge process even though both samples have identical composition (as confirmed by ICP result in Table 2.2). When comparing the total

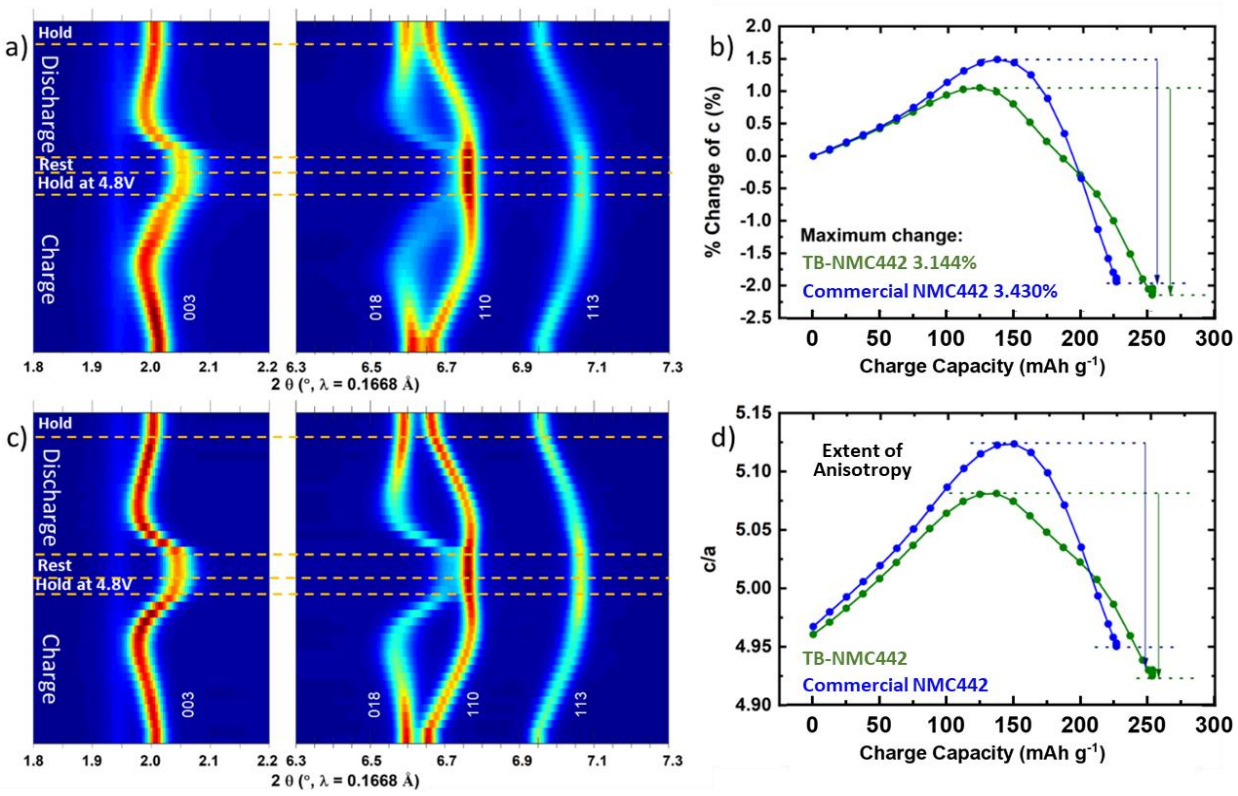

Figure 2.9 *Operando* X-ray diffraction results of TB-NMC442 and commercial NMC442. Contour plot of the diffraction peak evolution of (003), (018), and (110) planes during the first cycle of a) TB-NMC442 and c) commercial NMC442. Comparison of the corresponding calculated lattice parameters along b) the *c*-axis and d) the *c*/*a* ratio, showing the degree of anisotropic lattice changes as a function of the specific capacity during charge to 4.8 V (followed by 2 h hold at 4.8 V and rest for 2 h).

percentage of the *c* lattice parameter change during charge (i.e., from peak to trough), TB-NMC442 experiences a 3.14% change compared to the 3.43% change experienced by commercial NMC442. Here we want to emphasize that in principles the commercial NMC442 should have much smaller *c* lattice change since the obtained capacity is smaller than TB-NMC442. However, the observed opposite trend that commercial NMC442 shows larger c lattice change clearly show that the TB in NMC can mitigate the anisotropic changes.

Repeated anisotropic changes (expansion in *c*, contraction in *a*)[101–103] causes strain in lattice dimensions during Li extraction and insertion, which has been generally considered to be the major cause of particle cracking in the layered oxide materials. Such cracks are widely suspected to contribute to NMC degradation at high voltage. The cracks weaken the connections between materials and cause increased impedance as well as reduced electrochemical contact.[104] Furthermore, they allow electrolyte penetration into the

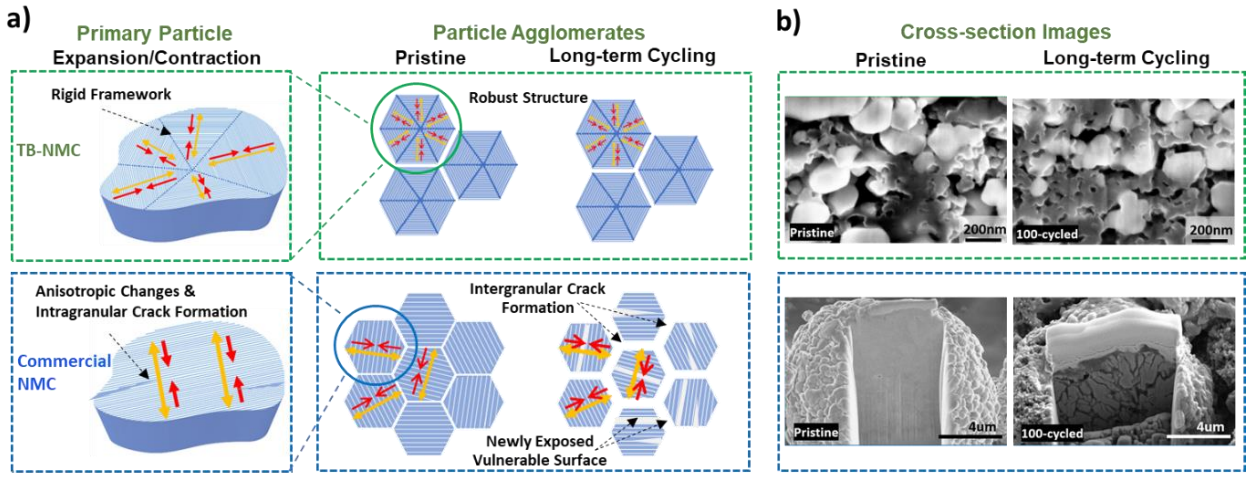

Figure 2.10 a) Schematic of the proposed mechanism showing how TBs can alleviate *c*-lattice changes during cycling and mitigate intragranular and intergranular crack formation in NMC materials; b) Cross sectional images of pristine and 100-cycled TB-NMC442 (green frames) and commercial NMC442 (blue frames).

interior of the cycled particles, which leads to severe parasitic reactions and irreversible phase transformation.[38,39] In our sXRD refinement results, the reduced *c* lattice expansion results in smaller anisotropic changes for TB-NMC442, indicating that TB-NMC442 is subjected to much less strain (Figure 2.9d) during cycling, thus showing an improved high voltage cycling stability.

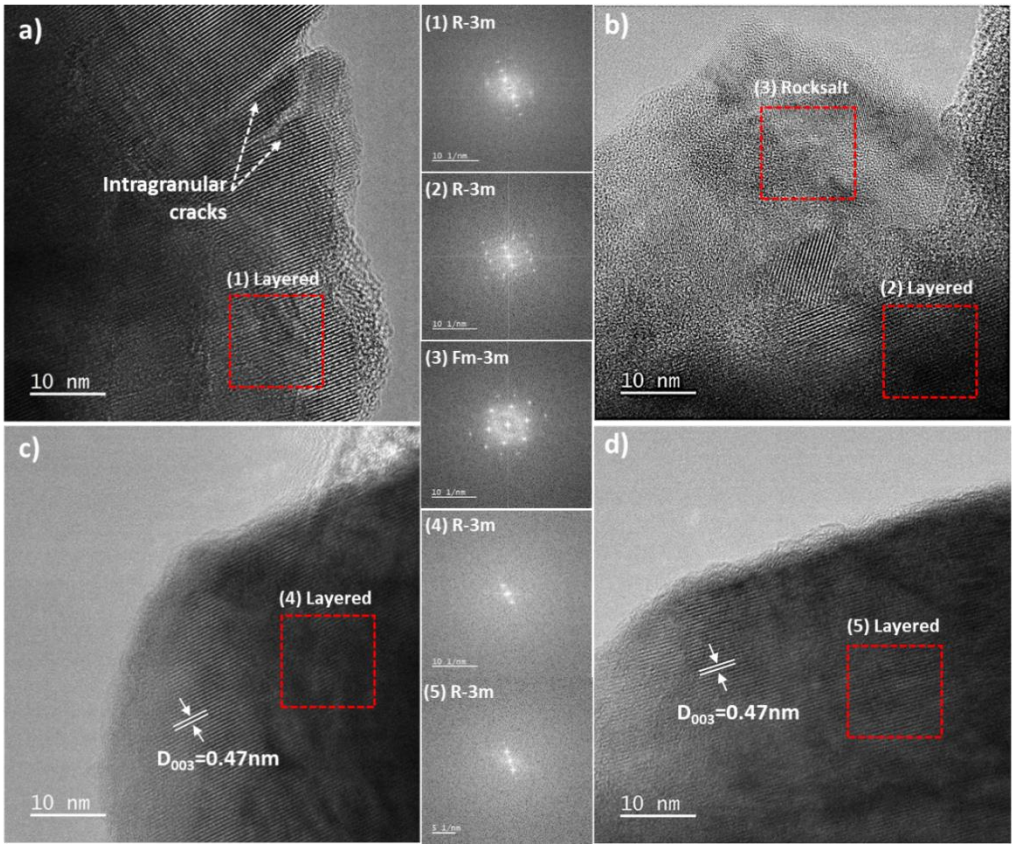

Figure 2.11 HR-TEM images of 500-cycled NMC materials. a) and b) commercial NMC622; c) and d) TB-NMC622.

Based on the results above, Figure 2.10a presents a schematic of the proposed mechanism showing how TBs can alleviate *c*-lattice changes, mitigate intragranular and intergranular crack formation, and improve cycling stability for NMC materials. In

commercial NMC, the primary particles experience expansion and contraction during cycling, especially along the *c*-direction. Intragranular cracks are easily formed and propagate during long term cycling with the continuous *c*-lattice changes, as suggested by STEM images of cycled NMC particles in many previous reports.[35,36] In this work, such intragranular cracks were also captured by HR-TEM images of 500-cycled commercial NMC622, as shown in Figure 2.11a. During long-term cycling, the primary particles could eventually break, and intergranular cracks can also form in the densely packed secondary particles as a result of continuous primary particle expansion/contraction. Severe intergranular cracks are observed in commercial NMC442 after cycling, shown in Figure 2.10b. The intragranular and intergranular crack formation will lead to the exposure of additional surfaces where parasitic reactions with the electrolyte will occur, resulting in the increase of electrical resistivity by disconnecting the charge transport pathway in the electrode. This will contribute to the capacity degradation in commercial NMC as cycling proceeds. It is important to note that the facets that are newly exposed during both intragranular and intergranular cracking may be more vulnerable to reacting with the electrolyte compared to the original surface facets of the secondary particles in commercial NMC. This comes from the differences in the formation of the interior and exterior primary particles during synthesis. While the exterior particles form surface facets with the minimized surface energy, interior particles form surface facets with minimized grain boundary energy. Grain boundary energy is decided by the relative crystallographic orientation between the neighboring primary particles. A lower misorientation angle generally leads to lower grain boundary energy. However, the minimization of the misorientation angle (and the lower grain boundary energy) does not guarantee lower

surface energies. Thus, it is expected that the surface of newly exposed interior particles is more likely terminated by non-(003) planes.[105] The non-(003) planes in the newly exposed particles are subjected to more vulnerability to side reactions. Thus, a combination of increased surface area and increased vulnerability will accelerate the capacity degradation of commercial NMC. In the HR-TEM images of cycled commercial NMC622 shown in Figure 2.11b, clear surface rocksalt phase transformation was observed, indicating the poor surface stability of commercial NMC622 samples.

In comparison, the benefit of having the designed TB in NMC mainly comes from two aspects: (1) Pristine TB-NMC particles are mostly terminated with more stable planes, preventing the parasitic side reactions between cathode and electrolyte. The surface stability of TB-NMC is evaluated with HR-TEM, where the layered structure was well maintained after 500 cycles and no intragranular cracking was observed. (2) In long-term cycling, the existence of TB alleviates the intragranular crack formation and new surface exposure to the electrolyte, as illustrated in Figure 2.10. In TB-NMC, the radially aligned TBs and the rocksalt-like phase formed along the TBs act as a rigid framework that does not expand and contract during cycling. This rigid framework in TB-NMC leads to a relative robust structure compared to commercial NMC, alleviating anisotropic changes and intragranular crack formation. Note that this alleviation effect does not necessarily require multiple TBs presenting in one grain. Even just one TB along the particle would mitigate the changes in *c* lattice. In addition, it is expected that TB-NMC442 has higher fracture toughness due to its smaller particle size. Previous studies have shown that layered oxide materials have a critical particle size below which crack formation can be prevented during cycling.[106,107] The critical particle size is about 200 nm for $LiNi_{1/3}Mn_{1/3}Co_{1/3}O_2$ and

80 nm for $LiNi_{0.80}Co_{0.15}Al_{0.05}O_2$,[107] comparable to the particle size of TB-NMC442 (138 nm).[85] Thus, the robust structure and the higher fracture toughness in TB-NMC mitigates the formation of intragranular and intergranular cracks. Consistent with these hypotheses, Figure 2.10b shows two contrasting morphological trends observed for TB-NMC442 and commercial NMC442. While almost no change in morphology is observed in TB-NMC442, but severe microcracks are observed in commercial NMC442 after 100 cycles. Similar morphology comparison in TB-NMC622 and commercial NMC622 after 500 cycles is shown in Figure 2.11, where severe intergranular cracks are seen in commercial NMC622.

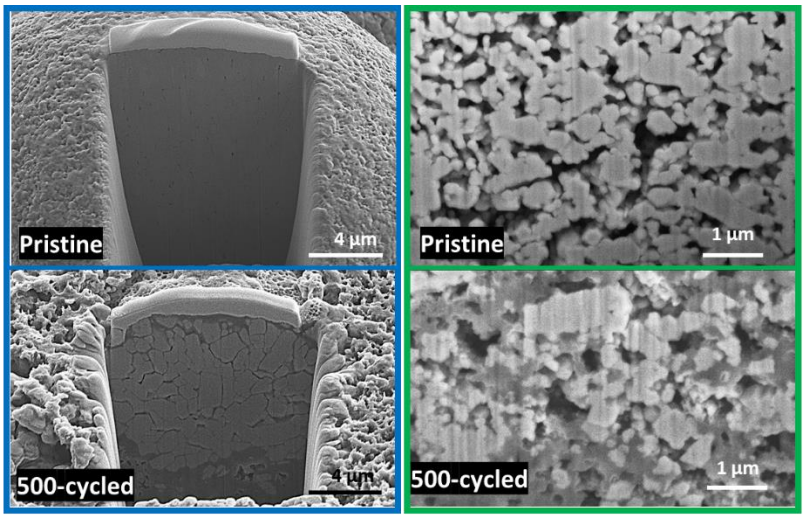

Figure 2.12 Cross sectional images of pristine and 500-cycled commercial NMC622 (blue frame) and TB-NMC622 (green frame).

2.4 Conclusions

In this work, TB defects are designed and introduced to NMC oxide materials through polyol synthesis method. The existence of the radially aligned TB defects is confirmed through high resolution STEM in a series of layered NMC materials. Compared

to commercially available NMC samples, multiple TB-NMC materials show an improved cycling stability at high voltage and high rate. For TB-NMC442 cycled at 1 C-rate between 2.5 – 4.7 V, it shows 17.3% more capacity retention compared to commercial NMC442 after 100 cycles. For TB-NMC622 with the same voltage cutoff and rate, it also shows 13.8% more capacity retention compared to commercial NMC622 after 500 cycles. An atomic scale analysis of the TB defects and its relationship with the enhanced electrochemical performance is presented in this study with advanced characterization tools. Two beneficial features of the designed TB defects are deconvoluted: Firstly, TB-NMC particles are mostly terminated with the (003) plane, which is a more stable surface against the electrolyte. Thus, TB-NMC prevents the parasitic side reactions between NMC cathode and electrolyte during cycling. Secondly, a rocksalt-like phase formed along the TBs can act as a rigid framework that mitigates the anisotropic changes and intragranular crack formation during cycling. In TB-NMC, the increased surface stability and high fracture toughness originated from the designed TB defects can effectively mitigate the structural degradation and capacity fade in NMC materials. This work sheds light on defect engineering as a novel and universal strategy for the future design of cathode materials for high voltage LIBs with ultra-long cycling life.

Chapter 2, in full, is a reprint of the material, as it appears in: Chung, H.*, **Li, Y.***, Zhang, M., Grenier, A., Mejia, C., Cheng, D., Sayahpour, B., Song, C., Shen, M.H., Huang, R., Wu, E.A., Chapman, K.W., Kim, S.J., and Meng, Y.S., 2022. Mitigating Anisotropic Changes in Classical Layered Oxide Materials by Controlled Twin Boundary Defects for

Long Cycle Life Li-Ion Batteries. Chemistry of Materials, 34(16), pp.7302–7312. The dissertation author was the co-primary investigator and co-first author of this paper.

Chapter 3. Regeneration of degraded Li-rich Layered Oxides Materials through Heat Treatment-Induced Transition Metal Ordering

3.1 Introduction

Rechargeable lithium-ion batteries (LIBs) have been widely studied over the last several decades.[108] The recent boost of electric vehicles and scale level energy storage has put even more challenge on the development of LIB cathode materials with high energy density and high power density.[109] The study of many conventional LIB cathode materials including $LiCoO_2$ (LCO), $LiFePO_4$ (LFP), and $LiNi_{1/3}Mn_{1/3}Co_{1/3}O_2$ (classical NMC) have been pushed to their theoretical limits, yet those materials cannot provide a specific capacity over 274 mAh g^{-1}.[110] LIB cathode materials delivering higher capacity are vital to meet the growing energy density requirements.[111] Among all the candidates, Lithium-rich layered oxides (LRLO) are considered one of the most promising next-generation high energy LIB cathodes due to their large specific capacity (over 300 mAh g^{-1}).[112] The LRLO materials are denoted in two ways in the literature: one is a nano-composite structure as $xLi_2MnO_3 \cdot (1-x)LiMO_2$ (M= Ni, Co, Mn or other transition metals (TMs)) proposed by Thackeray et al.,[22] another is a single phase solid solution as $Li[Li_xM_{1-x}]O_2$ proposed by Dahn et al.[23] Both denotation represents the same category of material. In LRLO materials, lithium ions intersperse into both the lithium layer and the TM layer of close packed oxygen framework, typically arranged as an O3 layered structure.[113] Within the TM layer, the Li atoms and TM form a honeycomb superstructure where Li sits at the center of each hexagon.[23] During charge and discharge, LRLO materials experience the redox of $TM^{3+/4+}$ or TM $^{2+/3+/4+}$ with simultaneous extraction/insertion of Li ions, which is similar to classical NMC layered oxides. However, the cationic redox alone is not sufficient to enable the large capacity observed in LRLO

materials. Thus, oxygen activity, or commonly referred to as anionic redox activity, is considered providing a significant portion of the large capacities in LRLO.

Although LRLO is known for its high capacity, the practical applications of LRLO materials are limited by several drawbacks, such as large irreversible capacity loss (20%−30%) at the initial cycle as well as the continuous capacity and voltage decay in the extended cycling.[114] In the applications that require stable voltage such as electric vehicles, the voltage fade in LRLO is especially detrimental.[115] The performance limitations of LRLO are usually correlated to the structure degradation and defects generation during cycling.[116] The structure degradation has been discussed through many different aspects such as the formation of oxygen vacancies,[114] the migration of TM atoms,[117] the formation of spinel phase,[118] and the accumulation of defects and microstrain.[119] To mitigate the voltage decay problem, many modification methods have been explored in the field. Coating layers such as Al_2O_3 and graphene oxide were introduced to LRLO materials to protect it from the harmful surface-electrolyte reaction and to restrict oxygen evolution and the subsequent TM migration.[120] The use of doping elements such as Al, Mg, Mo were also explored by many groups and proved to be able to alter the electronic structure and stabilize the voltage and capacity fade.[121] In addition, novel electrolytes with salt additives also show promising results through the improved charge-transfer resistance and cycling stability.[51]

Different from those modification strategies which mostly works on the pristine material, our group proposed a mild heat treatment method on the cycled material.[122] Our work revealed that the metastable state of cycled LRLO rooted from structural defects is responsible for the voltage decay, and that a structure and voltage recovery can be established by driving the metastable state to stable state with thermal energy. The reappearance of the honeycomb structure and Li migration from Li layer to TM layer was also observed in the heat treated sample. However,

the recovery mechanism of the honeycomb structure was not well elaborated in our previous study. In this work, the TM reordering is identified as the key step for the reappearance of the superlattice honeycomb ordering as well as the voltage recovery, and a clear reordering pathway is calculated. This work employs a series of in-situ characterization tools to view the structure evolution under real heating and cooling process and to understand the recovery from the TM environment perspective. In addition, heat treatment itself only recovers the voltage, but not the capacity in cycled LRLO. To solve this problem, an ambient-air relithiation was conducted on cycled LRLO materials to recover the Li loss induced capacity decay. The structure and voltage recovery induced by heat treatment, and the capacity recovery achieved through relithiation, together provide a pathway for the regeneration of the cycled LRLO materials.

The information in this article is discussed in the following major segments: (1) the structure recovery in LRLO is characterized through the increased Li occupancy in TM layer, the reappearance of the superlattice structure, and the improved ordering in the TM environment; (2) a comparison to classical layered oxides without TM superstructure is performed to validate the hypothesis of structure recovery driven by TM reordering; (3) based on the findings in the experimental characterization, a potential TM reordering pathway in cycled LRLO under heat treatment is proposed and proved by first-principles calculations; (4) the heat treatment induced voltage recovery is combined with an ambient-air relithiation process to enable cycled LRLO regeneration.

3.2 Experimental Methods

3.2.1 Preparation of Cycled Materials

$Li[Li_{0.144}Ni_{0.136}Co_{0.136}Mn_{0.544}]O_2$ (denoted as LR-NCM114) was synthesized through co-precipitation method. The detailed synthesis procedure can be found in our previous publication.[41] $LiNi_{0.8}Mn_{0.1}Co_{0.1}O_2$ (denoted as NMC811) was a commercial sample purchased from Shenzhen Beiterui Battery Materials Co., Ltd. Cycled LR-NCM114 powders were obtained from pouch cells with graphite anode. The cathode electrode was formed by active material: conductive agents: PVDF with a weight ratio of 94.5:3:2.5. The graphite anode has a mass ratio of graphite: conductive agent: binder = 95:2:3. The LR-NCM114 cell was cycled between 2.0-4.65 V; the NMC811 cell was cycled between 2.6 V and 4.3 V. The cells were stopped after the initial cycle. After cycling, the full cells were disassembled in an Ar filled glovebox. The cathode electrodes from each cell were washed with DMC to remove the extra $LiPF_6$ salt on the surface, and then the active materials were scratched from the electrode and dried in vacuum at room temperature overnight. All materials were stored in the glovebox for further characterizations.

3.2.2 Regeneration of Cycled Materials

Cycled LR-NCM114 materials were hand mixed with an excess amount of a eutectic Li salt mixture in mortar and pestle for 30 minutes. The Li salt mixture contains $LiNO_3$ and $LiOH{\cdot}H_2O$ with a molar ratio of 3:2. The mixture was heated at 300 °C for 15 hours for regeneration, and washed with deionized water to remove the excess amount of Li salts. The regenerated LR-NCM114 was dried in vacuum oven at 50 °C overnight.

3.2.3 Electrochemistry Tests

The pristine material was mixed with polyvinylidene fluoride (PVDF, HSV900, Kynar) and conductive agent (Super C65, TIMCAL) with a ratio of 8:1:1 to prepare the electrode. The cycled material containing 3% conductive agent and 2.5% PVDF was mixed with appropriate amount of Super C65 and PVDF to have a final mass ratio between cycled material: PVDF: Super C65 = 8:1:1. The mix was then well dissolved in a proper amount of N-Methyl-2-pyrrolidone (NMP, ≥ 99%, Sigma-Aldrich)) and mixed through the mixer (ARE-310, Thinky Corporation, Japan) in a plastic jar with 4 ZrO_2 beads to form the slurry. The slurry was casted onto Al foil and dried at 80 °C in vacuum oven for 12 hours. The electrode was punched into cathode discs with 14 mm diameter with a loading around 4 mg/cm^2. CR2016 coin cells were assembled in the glove box under argon atmosphere, with lithium metal as anode, Celgard 2325 as separator, and 1M LiPF6 in EC:DMC = 3:7 (V:V) as electrolyte (Gotion, USA). LR-NCM114 cells are cycled between 2.0-4.8 V with C/20 for the initial cycle and C/10 for the rest of the cycles (1C=250 mA g^{-1}). NMC811 cells are cycled between 2.5-4.7 V with C/10 for the first two cycles and C/3 for the rest of the cycles (1C=180 mA g^{-1}). All cells are rested for 6 h before testing. The electrochemical performances of the assembled coin cells were tested at room temperature either by Neware Battery Test System (Neware Technology Ltd., China) or Arbin BT2000 instruments (Arbin instrument, USA).

3.2.4 Neutron Powder Diffraction

High quality neutron powder diffraction (NPD) with *in-situ* heating and cooling were conducted at POWGEN beamline at the Spallation Neutron Sources (SNS) in Oak Ridge National Laboratory (ORNL). 500 mg of the cycled LR-NCM114 were placed in the beam. Quartz tube was used as the sample container to reduce the background signal. A gas environment containing 80%

nitrogen and 20% oxygen was used during the experiment. The SNS was operating at a nominal of 1100 kW. The center wavelength for the data collection was 1.5 Å. Neutron diffraction data were collected while simultaneously heating the material from 50 °C to 400 °C and cooling from 400 °C to 80 °C. At each 25 °C interval, a one-hour data collection was performed to acquire diffraction data. The neutron diffraction patterns were characterized using Rietveld refinement with GSAS-II[123] software to extract structural changes.

3.2.5 Synchrotron X-ray Diffraction and Pair Distribution Function

Ex-situ synchrotron XRD (sXRD) and pair distribution function (PDF) data were collected at 11-ID-B in Advanced Photon Source (APS) at Argonne National Laboratory with a wavelength of 0.2115 Å. Around 20 mg of each powder samples were loaded into Kapton capillaries and 5 min total scan time were collected for each sample. GSAS-II was used to extract the XRD pattern as well as performing Rietveld refinement to the collected data. PDF 2D data was calibrated and integrated with GSAS-II. The calibration was done with CeO2. PDF suite[124] was used to extract PDF patterns and to process G(r) functions. The Q-max used for the Fourier transfer is 20.5 $Å^{-2}$.

3.2.6 Transmission Electron Microscopy

The powder samples were dispersed on TEM lacey carbon grid inside Ar glovebox. The loading and transferring grids to transmission electron microscopy (TEM) were carefully executed to prevent air exposure. TEM was performed on a field emission gun JEOL2800 at 200kV with Gatan OneView Camera (full 4K*4K resolution). Scanning transmission electron microscopy (STEM) and energy dispersive spectroscopy (EDS) was performed on primary particles using a JEOL2800 at 200 kV in ADF mode.

3.2.7 X-ray Absorption Near Edge Structure and Extended X-ray Absorption Fine Structure

Temperature-dependent Mn, Ni, & Co K-edge X-ray absorption near edge structure (XANES) and extended X-ray absorption fine structure (EXAFS) measurements were performed on cycled LR-NCM114and cycled NMC811 material at beamline 12-BM at APS. The beamline is equipped with a Si (111) double crystal monochromator. Edge measurements were performed concurrently and in steps up to 400 °C under normal atmosphere conditions. Edge measured were done in tandem with their reference foils used for energy calibration. A 5-minute rest period for each temperature step was implemented to ensure an equilibrated temperature. ATHENA software from the IFEFFIT package[125126] was used to carry out the data processing. A model function was generated by performing ab-initio calculations using the code FEFF8.2[127] and least-squares fit to the data using ARTEMIS software from the IFEFFIT package.

3.2.8 Computation Methodology

The energy states of cycled LR-NCM114and heat-treated LR-NCM114were performed in the spin polarized GGA+U approximations to the Density Functional Theory (DFT) as implemented in the Vienna ab initio simulation package (VASP).[128] The same effective U value as applied in our previous report was used to enforce the effect of localized d electrons of the transition-metal ions.[49] We used the PBE exchange correlation, and a plane-wave representation for the wave function with a cutoff energy of 520 eV.[129] The Brillouin zone was sampled with a dense k-points mesh by Gamma packing. The crystal structure of $Li_{14}Ni_3Mn_7O_{24}$ was used as a starting point in the simulation. A specific $Li_{12/14}$ concentration with one oxygen vacancy was chosen to simulate the discharged state obtained experimentally. The full range of different configurations for the unit cell of $Li_{12}Ni_3Mn_7O_{23}$ were tested in our previous work. The lowest

energy model with one Li vacancy in Li layer and the other Li vacancy in TM layer was employed in this work. And then transient state was simulated by moving the neighboring TM to the Li vacant site in TM layer. The nudged elastic band (NEB) method was used to find the minimum-energy path and the energy barrier for lithium and TM migration.

3.3 Results and Discussion

3.3.1 Bulk Structure Recovery of Cycled LRLO

The electrochemistry performance of pristine LR-NCM114 is shown in Figure 3.1. In the first cycle, the low initial Coulombic efficiency of 83.8% indicates the structure degradation along with electrochemistry reaction.[114] The oxygen plateau disappears after first cycle, leading to a huge drop in the average discharge voltage and the overall energy density. In the following cycles, more decrease in discharge capacity and discharge voltage is observed, indicating continuous structure degradation with cycling.[130] As shown in Figure 3.2a, heat treatment was conducted on initially cycled LR-NCM114 with different temperatures, and the voltage recovery is observed in heat

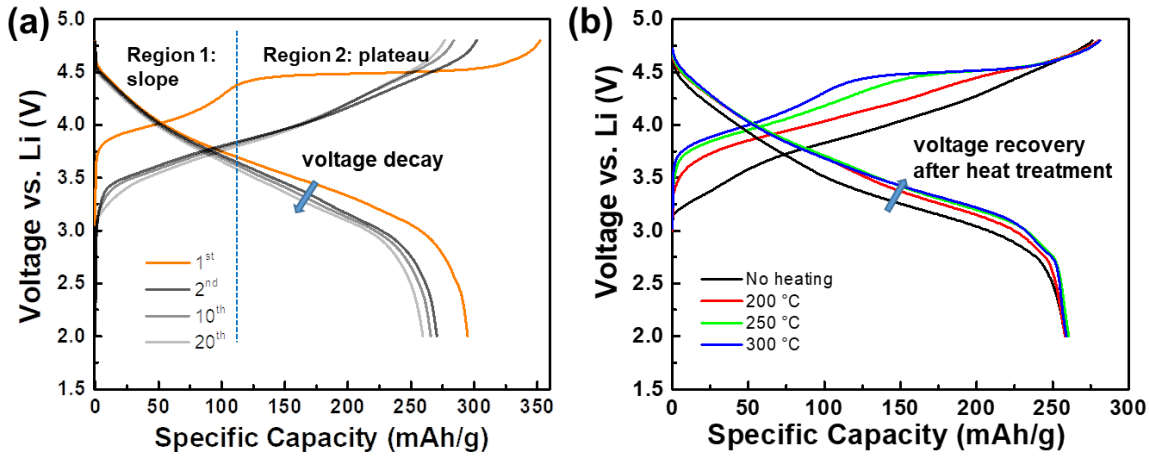

Figure 3.1 (a) Voltage profiles of pristine LR-NCM114; (b) The 51st voltage profile comparison of cycled LR-NCM114 before and after heat treatment. Pristine LR-NCM114 is labeled as No heating, and the LR-NCM114 samples that cycled for 50 cycles then received heat treatment are labeled with the different heating temperature.

treated samples. The four samples with different annealing temperatures all deliver similar amount of discharge capacity since no extra amount of Li was introduced to the samples during heat treatment. The plateau region also reappears in the 300 °C heat-treated sample. This plateau originates from the Li-O-Li configuration between Li layer and Transition metal (TM) layer.[131] The reappearance of the plateau indicates structure recovery of cycled LR-NCM114 after heat treatment. Similar trend is observed with the LR-NCM114 after long cycling. Heat treatment was performed to 50-cycled LR-NCM114 and the electrochemistry performance comparison of heated and unheated samples are shown in Figure 3.1b. The plateau region in the voltage profile reappears in the 300 °C heat-treated sample too. All heat-treated samples in the following part of this work are heated at 300 °C for 1 hour since it shows the best performance in the electrochemistry testing.

To investigate the origin of this voltage and structure recovery, synchrotron X-ray diffraction (sXRD) and neutron powder diffraction (NPD) were used to characterize the structural changes of cycled LR-NCM114over the heat treatment. Figure 3.2b shows the superlattice peak region of the sXRD pattern of the collected samples. After just the first cycle, the superlattice peak of LR-NCM114almost disappears, implying severe degradation of the honeycomb structure. The superlattice peak appears again after heat treatment, representing the structure reordering in TM layer. NPD with in-situ heating and cooling was conducted to the initially cycled LR-NCM114 to further explore the recovery of structure. Due to the nature of neutron-atomic nuclei interaction and neutron-unpaired electrons interaction, NPD is believed to be more suitable and capable than XRD in probing light elements such as Li.[132] The contour plot of NPD patterns with different temperatures is shown in Figure 3.2c. No additional peaks were developing during the heat treatment, indicating that the bulk structure maintains well under the heating. It can be clearly seen

that most changes happen after 200 °C, meaning that there is a threshold of the temperature needed to recover the voltage and structure in the cycled LR-NCM.

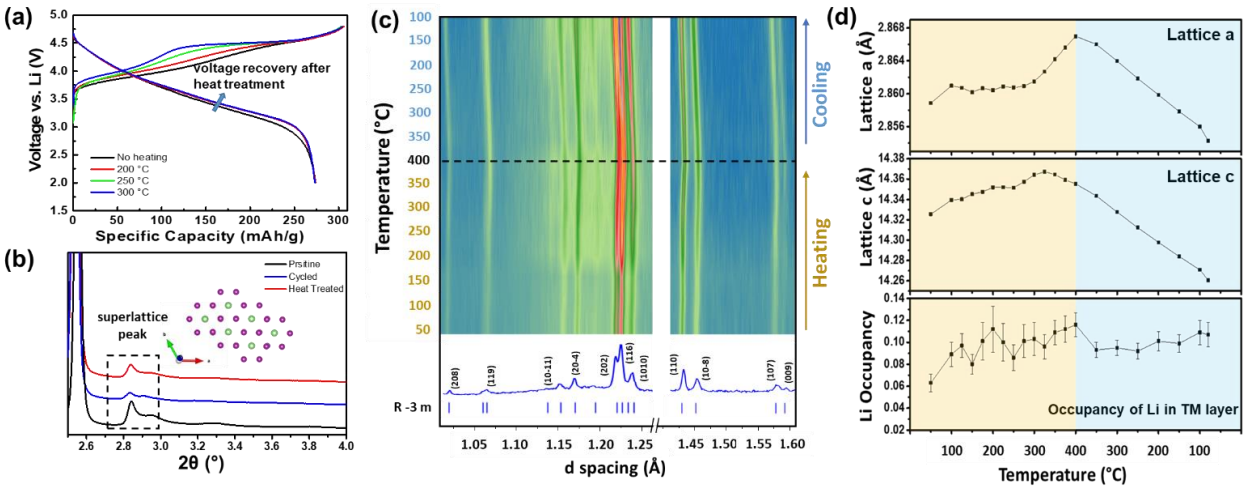

Figure 3.2 (a) The 2nd cycle voltage profile of LR-NCM114 after initial formation cycle before and after heat treatment; (b) *Ex-situ* sXRD data of pristine LR-NCM114, initially cycled LR-NCM114, and cycled LR-NCM114 after heat treatment; (c) Contour plot of the NPD data with in-situ heating and cooling; (d) Rietveld refinement results of the NPD patterns, giving the *a* and *c* lattice parameters and the Li occupancy in the TM layer.

Rietveld refinement was performed on the collected NPD patterns to quantify the structure changes of LR-NCM114 over the heat treatment. Figure 3.3b shows a representative refined pattern of the initially cycled LR-NCM. The NPD pattern can be well indexed to R-3m space group, with lattice parameter a = 2.859 Å and lattice parameter c = 14.326 Å. The obtained refinement results for the whole in-situ heating and cooling process are plotted in Figure 3.2d. Both lattice parameter *a* and *c* show a non-linear increase in the heating and rapid linear decrease in the cooling, indicating that the heating process is a combination of thermal expansion and structure transformation. After heat treatment, both lattice *a* and *c* are relaxed to an even lower value than the ones before heating. The irreversible lattice parameter expansion of LR-NCM114 during cycling is usually assigned to the increased structure disorder coming from the strain

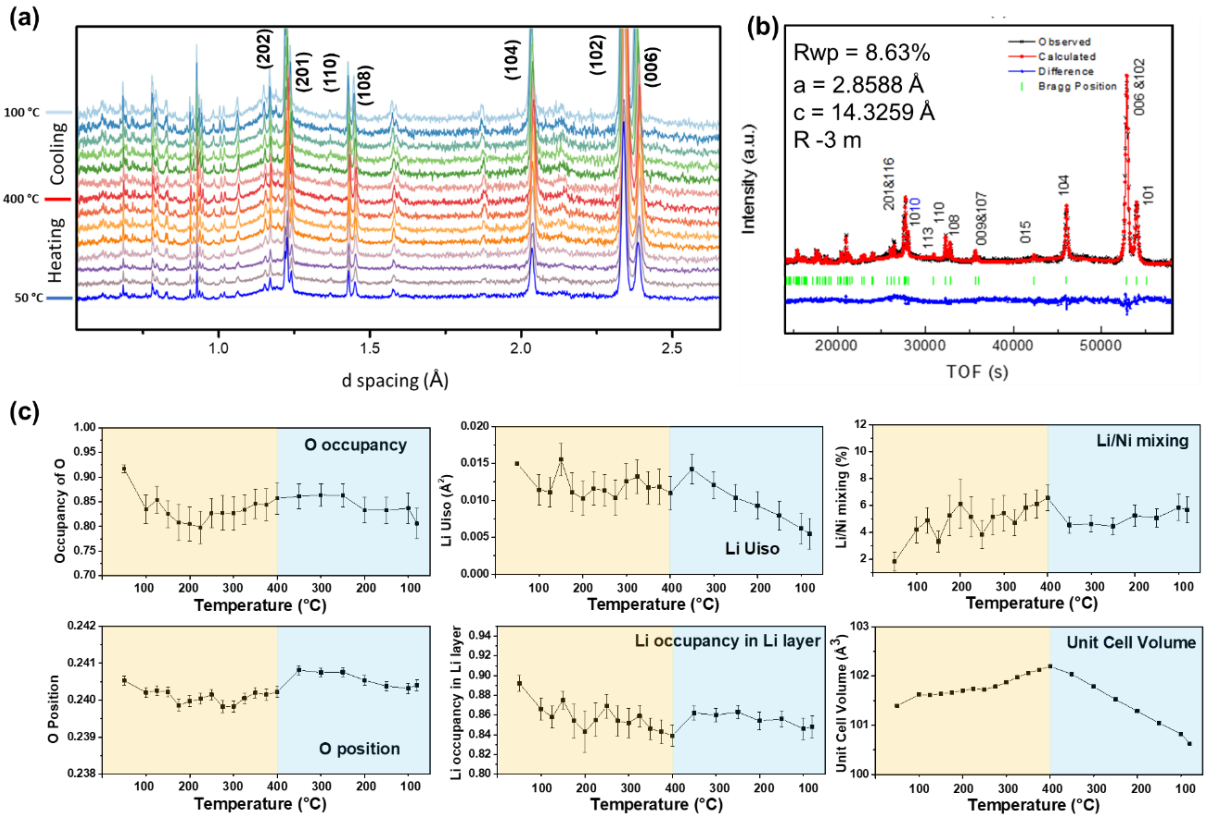

Figure 3.3 (a) NPD patterns collected during the in-situ heating and cooling experiment; (b) NPD pattern of cycled LR-NCM114 at room temperature with Rietveld refinement; (c) Rietveld refinement results including O occupancy, O position, U_{iso} of Li, Li occupancy in Li layer, Li/Ni mixing, and unit cell volume.

accumulation, lithium deficiency, or formation of new phases such as spinel or other layered structures.[133] The shrinkage in lattice parameters after heat treatment indicates the structure recovery of the layered Li-rich materials. More importantly, a change in the occupancy of Li atoms in the TM layer is observed from the in-situ NPD. With the increase of temperature, the Li amount in the TM layer increases from 0.063 to 0.116 (with the designed value of 0.144). During the cooling process, the occupancy of Li in TM layer decreases slightly but stabilizes around 0.107 at the end of the cooling. The changes in the Li occupancy indicate that during the heating process, Li atoms could go to the TM layer from Li layer. In the meantime, Li vacancies could form in the

Li layer, causing a decrease of Li occupancy in Li layer as well as an increase of Li/Ni mixing in the structure after heat treatment (Figure 3.3c).

To summarize the findings in sXRD and NPD, an increased occupancy of Li in the TM layer is observed after heat treatment, along with the contraction of lattice parameters and the reappearance of the superlattice peak. Those changes mostly happen during the heating process instead of the cooling, showing that temperature is an essential factor enabling the structure recovery. In this structure, the increased amount of Li in the TM layer could re-create the Li excess environment and thus re-enable the oxygen plateau and oxygen activities in the following cycling. With Li atoms going back to the TM layer, the electrostatic repulsion between TM atoms becomes alleviated, causing the decrease in lattice *a*. Furthermore, the increase of the Li occupancy in the TM layer should be viewed and analyzed with the reappearance of superlattice peak. It is known that such peaks come from the short-range ordering of Li and TM atoms on a $\sqrt{3}a_{hex.} \times \sqrt{3}a_{hex.}$ superlattice within the TM layer. The reappearance of superlattice peak indicates that Li atoms have site preference when they go to the TM layer, which can be characterized by the changes in TM atoms environment.

3.3.2 Local Structure Evolution During Heat Treatment

To further investigate the changes in the TM environment during the heat treatment, in-situ X-ray absorption near edge structure (XANES) and extended X-ray absorption fine structure (EXAFS) were conducted on the initially cycled LR-NCM114. Figure 3.4a shows XANES spectra at Mn K-edge. Compared to pristine state, a slight shift to lower energy is observed in cycled LR-NCM114, corresponding to a slight reduction of Mn which might be a result of some loss of oxygen during the initial cycle. No obvious edge shift is observed during the heat treatment, meaning that heating is not causing any oxidation state changes. The magnified pre-edge features

are also shown in Figure 3.4a as an inset. The pre-edge region is believed to be very sensitive to the TM-O local structure, where the deviation from centrosymmetry can largely impact the pre-edge environment. The loss of local ordering coming from TM migration and TM-O bond distortion are all proved to contribute to the pre-edge intensity increase in many studies.[134] In our case, the Mn K-edge pre-edge intensity significant decreases, which can be attributed to the increased centrosymmetry after heat treatment. The EXAFS spectra at Mn K-edge is shown in Figure 3.4b, where a large increase of the first shell Mn-O intensity and Mn-TM intensity is observed in the cycled LR-NCM114 after heat treatment, indicating the restoring of superlattice structure as well as the increased ordering in the structure.[135] The Mn-TM and Mn-O peak intensity increases should be viewed together with the increased Li amount in the TM layer and the reappearance of the superlattice structure. After first cycling, irreversible Li loss in the TM layer could cause some Li vacancies. The broken honeycomb ordering could also indicate an uneven distribution of positive-charged TM ions in the structure, leading to an overall distortion between

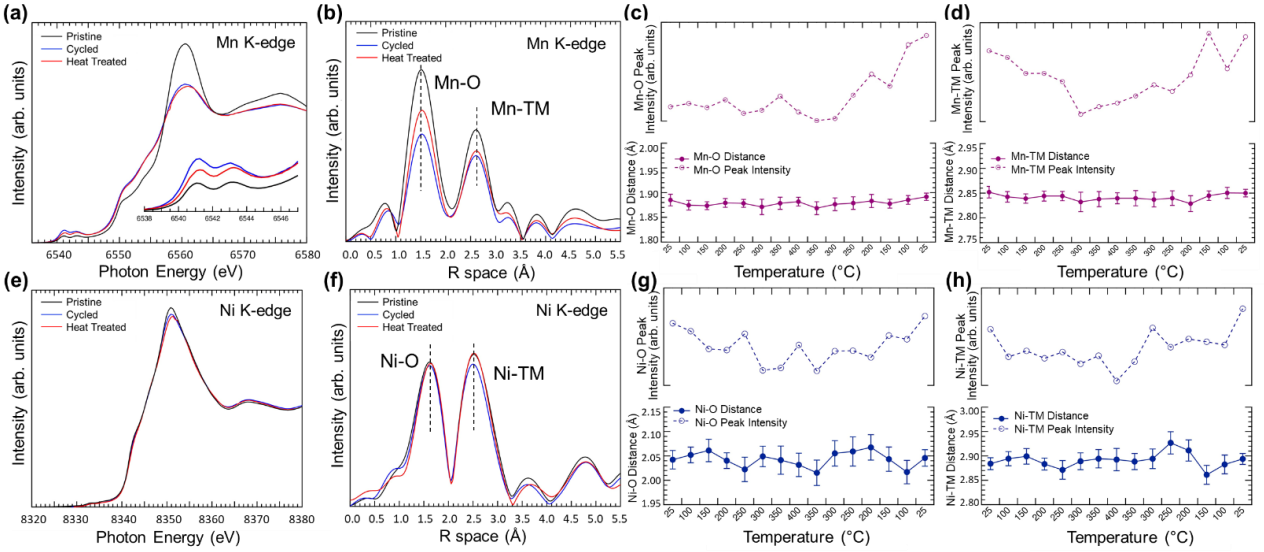

Figure 3.4 XAS analysis of initially cycled LR-NCM114 with in-situ heating and cooling: (a) XANES spectra at Mn K-edge with the magnified pre-edge features; (b) EXAFS spectra at Mn K-edge; (c) Fitting results for Mn-O bond; (d) Fitting results for Mn-TM bond; (e) XANES spectra at Ni K-edge; (f) EXAFS spectra at Ni K-edge; (g) Fitting results for Ni-O bond; (h) Fitting results for Ni-TM bond.

TM and O as well as the decrease of Mn-O intensity in EXAFS. After heat treatment, the vacancies in TM layer are filled with Li again and the honeycomb ordering is restored. The restored honeycomb ordering in TM layer leads to an increased Mn-O bond length distribution symmetry in EXAFS, reflected by the increased Mn-TM and Mn-O peak intensity.

Figure 3.5 and Table 3.1 shows the data and corresponding Mn K-edge EXAFS fits of LR-NCM114 before and after heat treatment, with the rest of the data analyzed using the same method. Figure 3.4c and 3.4d shows the fitting results of Mn-O bond and Mn-TM bond obtained from the EXAFS Mn K-edge spectra to quantify the changes of Mn oxidation state and Mn environment ordering during the heat treatment. During the in-situ heating and cooling, no obvious changes can be observed in the Mn-O peak position. The stable peak position validates the conclusion from XANES that Mn remains the same oxidation state during the heat treatment. The Mn-O peak height obtained from the EXAFS fluctuates around its staring point during the heating process, then increases rapidly during the cooling. As discussed above, the peak height depends on the system ordering as well as Debye-Waller factor. As the temperature increases, there is an increase in the Mn environment ordering, which increases the EXAFS signal. However, the Debye-Waller factor also increases with temperature, which decreases the EXAFS signal.[136] The result is competing factors causing the peak height a bit erratic during the heating. After cooling down to room temperature, Mn-O bond shows a clear increase in its intensity. Similarly, an erratic behavior of the Mn-TM peak height is observed at high temperature, and a large increase is observed at the end of the cooling. Intensity increase in both Mn-O bond and Mn-TM bond clearly indicates the reordering of the Mn environment as a result of the increased Li amount in TM layer and the recovery of the honeycomb structure reordering.

The XANES and EXAFS spectra as well as fitting results at Ni K-edge are shown in Figure 3.4e-3.4h as well as Figure 3.6 and Table 3.2. The XANES spectra shows no oxidation state change in Ni. Similar to the Mn K-edge EXAFS, the Ni-O and Ni-TM intensity also shows an increase after heat treatment, indicating the reordering of Ni environment. The changes of Ni-O and Ni-TM peak position and peak height are quantified through fitting results, where a fluctuation is also observed at high temperature range. The sigma squared value of the TM and O positions obtained through EXAFS fitting are shown in Table 3.1 and 3.2. After heat treatment, the sigma squared value for both Mn K-edge and Ni K-edge is much smaller than cycled state, which also indicates less disordering.

Table 3.1 Fitting results for the cycled and heat treated LR-NCM114 at Mn K-edge obtained from in-situ EXAFS.

Fit Parameter	Space Group	Ni	Co	Mn	Space Group	Mn			
	R3-m LCO	0.166667	0.166667	0.16666667	C2/m Li2MnO3	0.5			
1st Shell	Mn-O (Å)	ss(Å^2)	Mn-TM(Å)	ss(Å^2)	dE	CN	Δk (1/Å)	R-range	R-factor
Cycled	1.8849	2.64E-03	2.8519	3.37E-03	7.9	6	3.8 - 10	1.0 - 5.0	0.0091
Heat Treated	1.8916	4.60E-05	2.8499	2.44E-03	8.8	6	3.8 - 10	1.0 - 5.0	0.0091

Table 3.2 Fitting results for the cycled and heat treated LR-NCM114 at Ni K-edge obtained from in-situ EXAFS.

Fit Parameter	Space Group	Ni	Co	Mn					
	R3-m LCO	0.333333	0.333333	0.33333333					
1st Shell	Ni-O (Å)	ss(Å^2)	Ni-TM(Å)	ss(Å^2)	dE	CN	Δk (1/Å)	R-range	R-factor
Cycled	2.0422	6.55E-03	2.8841	5.41E-03	5.5	6	3.0 - 8.8	1.0 - 5.2	0.0112
Heat Treated	2.0458	6.45E-03	2.8937	4.33E-03	6.1	6	3.0 - 8.8	1.0 - 5.2	0.0078

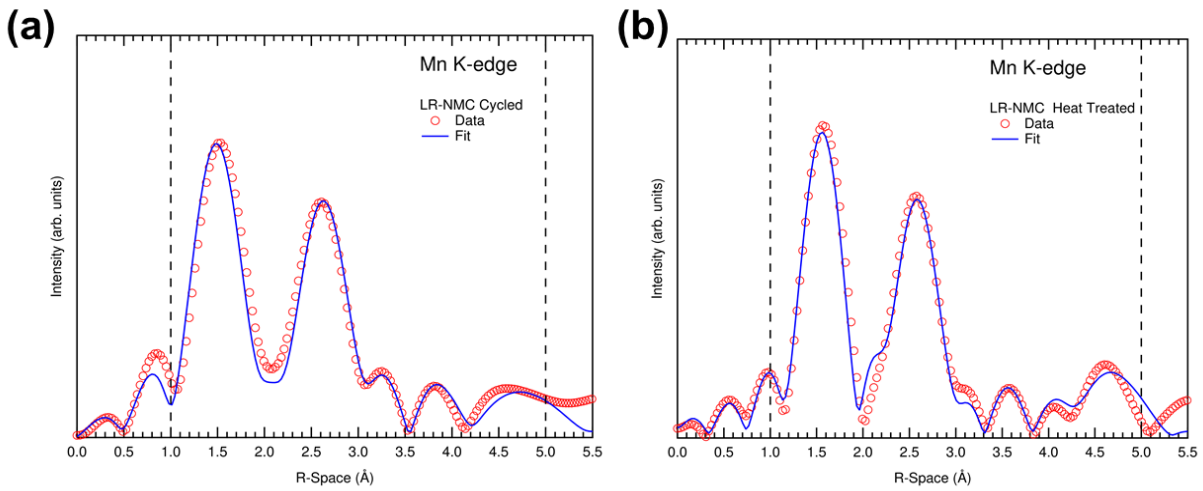

Figure 3.5 Mn K-edge EXAFS raw spectra and fitting results of (a) cycled LR-NCM114 and (b) heat-treated LR-NCM.

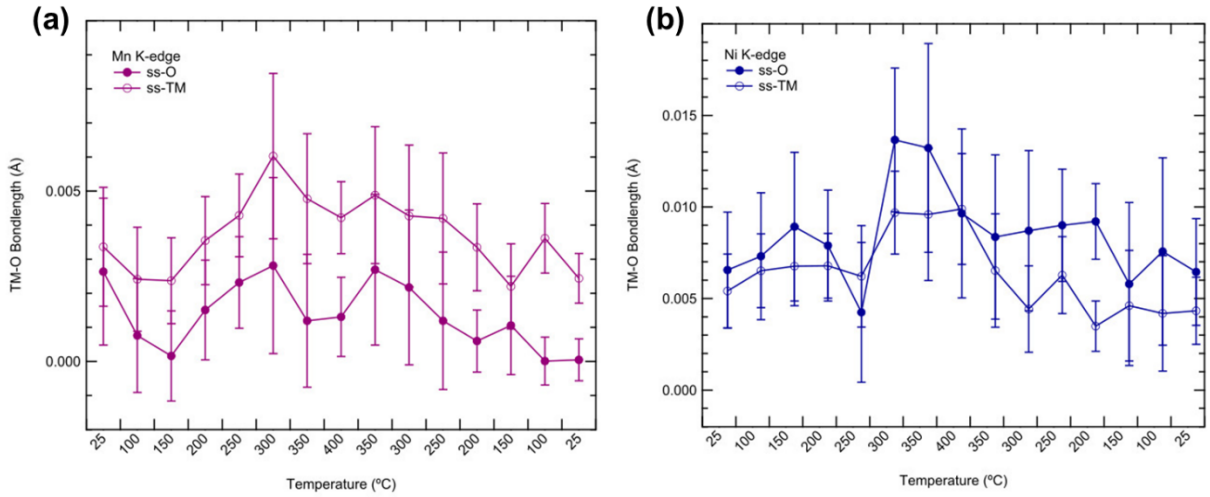

Figure 3.6 (a) sigma squared value of the TM and O position obtained through EXAFS fitting of the (a) Mn-K edge and (b) Ni K-edge.

Confirmed by XANES and EXAFS, TM atoms in the sample is showing an increased ordering in the first shell coordination. Ex-situ Pair Distribution Function (PDF) is conducted on LR-NCM114 samples to capture the changes of local TM environment in both the short range and the intermediate range. The electron density pair distribution function G(r) was obtained from the

synchrotron X-ray total scattering (both Bragg and diffuse) with high real space resolution. The PDF pattern of pristine LR-NCM114, initially cycled LR-NCM114, and initially cycled LR-NCM114 after heat treatment are collected and compared in Figure 3.7a. The overall structure of three samples are identical with no additional peaks found in any sample, indicating that TM framework maintains well in the heat treatment. Based on the distances of different atom-atom pairs, the PDF patterns are divided into two regions as short range (first coordination shell) and intermediate range (larger than first coordination shell). In the short range, peaks at a distance shorter than 1.9 Å do not correspond to any atom-atom pairs since those peaks are just termination ripples from the Fourier transform at a finite Q.[137] The first peak around 2 Å is assigned to the TM-O pair, where TM corresponds to the cations in the TM layer. Figure 3.7b shows the magnified TM-O correlation regions in both the short range and the intermediate range. These regions are chosen because the TM-O pair length has lowest overlap with TM-TM atom pairs within these range. Compared to the pristine state, the intensity of TM-O peaks dropped largely after first cycle, showing an increased displacement. In line with EXAFS result, PDF also shows that the TM-O peak intensity of the cycled LR-NCM114 increased after heat treatment, indicating an increased ordering of the TM environment. However, the TM-O peak intensity of the heat treated sample is still lower than the pristine state, meaning the partial structure recovery by heat treatment. Figure 3.7c shows the magnified regions of TM-TM correlations, where an increase of TM-TM peak intensity is observed after heat treatment. The increase of TM-TM intensity is directly related to the reappearance of the superlattice peak, indicating the reordering of Li atoms and TM atoms in the TM layer. PDF results are in good agreement with EXAFS data and the increase in TM-TM and TM-O peaks confirm the increased ordering of TM environment in both short range and intermediate range.

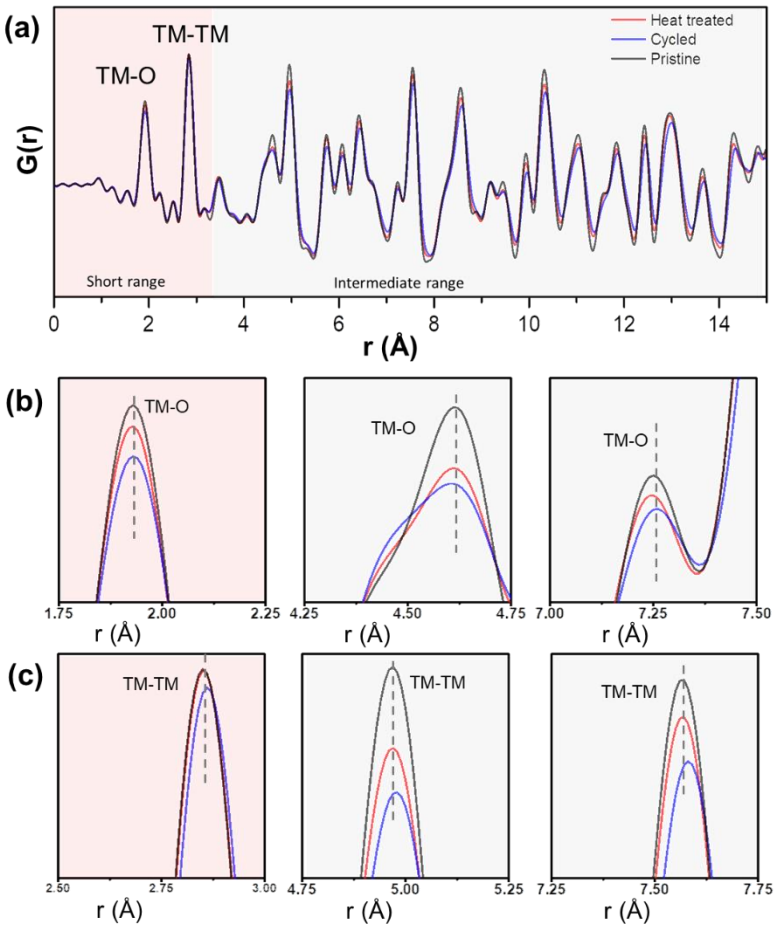

Figure 3.7 (a) PDF data of pristine LR-NCM114, initially cycled LR-NCM114, and cycled LR-NCM114 after heat treatment; (b) Four magnified regions showing TM-O (re)ordering in pristine sample and after heat treatment; (c) Four magnified regions showing TM-TM (re)ordering in pristine sample and after heat treatment.

3.3.3 Calculation of the Structure Recovery Pathway

As suggested by a series of characterization tools, heat treatment can successfully induce structure and voltage recovery in cycled LRLO, with an increased amount of Li back to TM layer and an increased ordering in the TM environment. To further understand the mechanism behind this structure recovery, computation effort was introduced with a proposed TM reordering pathway. Figure 3.8a presents a schematic energy map of cycled LRLO materials under heat

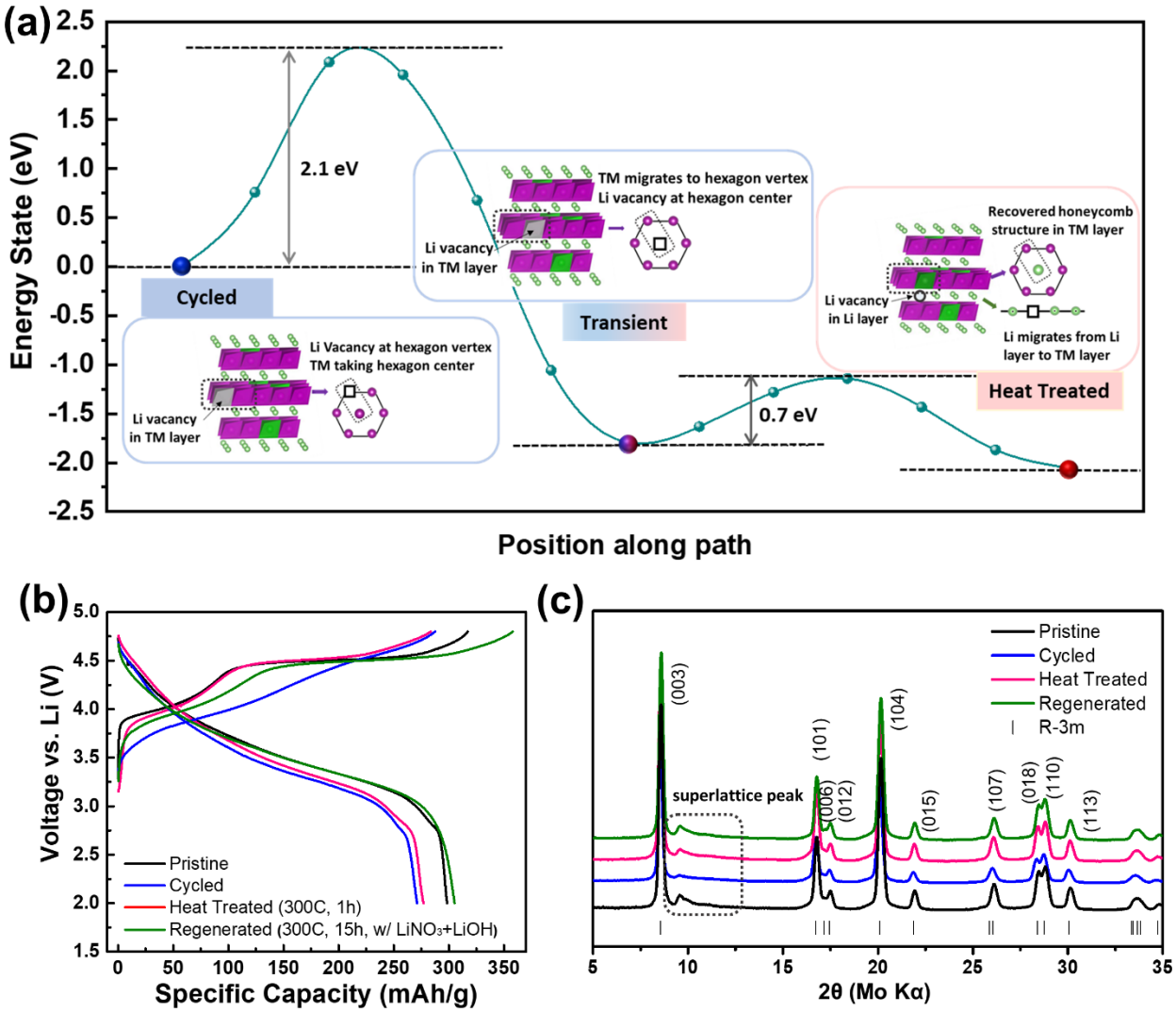

Figure 3.8 (a) Schematic energy map of cycled LRLO materials under heat treatment. The energy of three different states (cycled, transient, heat treated) were calculated, the kinetic energy barriers between each state are also shown in the figure. (b) Voltage profiles and (c) XRD patterns of the 1cycled LR-NCM114 under different regeneration conditions are also compared.

treatment. Three different states (cycled, transient, and heat treated) are shown in this map, and the kinetic energy barriers are calculated between each state. The simplified local structure of each proposed state is also presented in this Figure. At the "cycled" state, an irreversible Li loss happens in the TM layer, and some of the TM ions will move from the vertex of the hexagons to the Li

vacancy spot at the center of the hexagons, disrupting the ordered superlattice structure. Such migration happens continuously with increased cycle numbers, leading to the disappearance of the superlattice peak after long cycling. After heat treatment, the occupancy of Li in the TM layer increases and the superlattice ordering reappears. To achieve the "heat treated" state from "cycled' state, a necessary step will be moving the center TM ion in the hexagon back to the vertex, leaving the center site as a vacancy in the TM layer for the Li ions to insert from Li layer, and this state is named as "transient" state.

The calculated "transient" state is 1.8 eV (per calculation supercell) lower than the "cycled state"; the calculated "heat treated" state is also 0.3 eV lower than the "transient" state, which confirms our hypothesis on the three energy states in the structure recovery. Thermodynamically speaking, this TM reordering pathway should be able to happen spontaneously, bringing in a question mark on the necessity of heat treatment. However, it will be a different story if we take kinetic factors into consideration. After calculating the kinetic barrier needed between each step, it can be clearly seen that a huge kinetic barrier around 2.1 eV appears before the "transient" step. Compared to the step from "cycled" to "transient" state, the kinetic energy needed from "transient" to "heat treated" state is relatively low, around 0.7 eV. Heat treatment provides necessary energy for the migrated TM ions to overcome the kinetic barrier to go back to the vertex of each hexagon. Such a high kinetic barrier also partly explains why the cycled LR-NCM114 only exhibits partial recovery instead of full recovery under short time heat treatment. Longer heating time might help achieve better TM reordering. Besides that, the irreversible Li loss also makes it impossible for the structure to fully return to the initial TM ordering without introducing any extra Li to the TM layer, which also explains why the heat treatment itself can only recover the voltage, but not the capacity in cycled LRLO materials.

3.3.4 Capacity Recovery through Ambient-air Relithiation

To explore the possibility for fully regenerating cycled LRLO (recovering both the voltage and the capacity), ambient-air relithiation was conducted on initially cycled LR-NCM114 together with the heat treatment at 300 °C. The relithiation agent is a mix of $LiNO_3$ and $LiOH \cdot H_2O$ with a molar ratio of 3:2, explored in our previous work.[138] The heating time was prolonged to 15 h for TM ions to better overcome the kinetic barrier between "cycled" state and "transient" state. The initially cycled LR-NCM114 after 1h heat treatment at 300 °C is still denoted as "Heat Treated", while the cycled LR-NCM114 after 15 h heat treatment with relithation agent is denoted as "Regenerated". Figure 3.8b presents the voltage profile of initially cycled LR-NCM114 under different heating or regeneration conditions, with cell configuration details in Table 3.3. ICP-MS results and the electrochemistry performance of those samples are listed in Table 3.4. In the heat treated sample, the Li/TM ratio is similar to the cycled LR-NCM114. However, a large increase of Li/TM ratio is seen in the regenerated sample, representing the successful relithiation. In Figure 3.8b, the red line represents the heat treated sample, while the green line represents the regenerated sample. Compared to the cycled state, both heated samples show the oxygen plateau in the charge curve again. The average discharge voltage also increases from 3.49 V in the cycled LR-NCM114 to 3.52 V in the regenerated sample. The voltage and structural recovery from heat treatment is not affected by the presence of relithiation salt. The heat treated sample without relithiation delivers similar capacity (~272 mAh g^{-1}) as the cycled sample before heat treatment. But the regenerated sample delivers 305 mAh g^{-1} discharge capacity, showing very similar discharge curve as the pristine material represented by the black line**.** Figure 3.8c compares the XRD pattern of cycled LR-NCM114 under different heating or regeneration conditions, where no impurity peaks are found. It also clearly shows that the superlattice peak grows even higher in the regenerated

sample compared to the heat treated sample, as a result of the prolonged heating time. Overall, the computation results match well with the proposed TM reordering pathway, showing that heat treatment can successfully recover the TM ordered structure by overcoming the kinetic barrier of moving TM ions back to hexagon arrangement and forming Li vacancies in the TM layer for Li atoms to insert from Li layer. Guided by the calculated TM recovery pathway, prolonged heating time with relithiation was performed to cycled LR-NCM114 and can achieve full regeneration of cycled LR-NCM114.

Table 3.3 LR-NCM114 Cell Testing Conditions.

	Cell Specification
Counter electrode	Li metal chip (Thickness: 1mm, diameter: 15.4 mm)
Voltage range	2.0 – 4.8 V
Test protocals	Rest for 6 h after assembling, then 12.5 mA g^{-1} for one cycle, 25 mA g^{-1} for the rest
Separators	Celgard 2325
Electrolyte type	1M $LiPF_6$ in EC:DMC =3:7 vol%
Electrolyte amount	50 µl
Cell type	CR2016
Active material loading	3.5 - 4.0 mg cm^{-2}

Table 3.4 ICP-MS and Electrochemistry Comparison of cycled LR-NCM114 after different regeneration conditions.

	Li/TM ratio (from ICP-MS)	**Ch Cap. (mAh/g)**	**DCh Cap. (mAh/g)**	**ICE (%)**	**Average Ch V (V)**	**Average Dch V (V)**	**Average V diff (V)**
Pristine	1.39	318	299	94.1	4.37	3.55	0.83
Cycled	1.26	287	271	94.3	4.19	3.49	0.69
Heat Treated	1.26	284	277	97.6	4.36	3.54	0.82
Regenerated	1.37	357	305	85.2	4.35	3.52	0.83

3.4 Conclusions

Cycled LRLO materials show voltage and structure recovery after heat treatment. In this work, the mechanism of the voltage and structure recovery was investigated from the perspective of TM reordering. sXRD and NPD experiments proved Li migration from Li layer to TM layer, recreating the local Li-excess environment, accompanied by the reappearance of superlattice ordering and the contraction of overall lattice. EXAFS and PDF confirmed the increased ordering of TM environment in both the short range and the intermediate range. A TM reordering pathway was proposed and evaluated with computation methodology, where a kinetic barrier to move TM ions to reform the honeycomb frame is believed to be the controlling step in this heat induced structure and voltage recovery. Guided by the computation effort, regeneration of cycled LRLO was achieved through heat treatment and ambient-air relithiation at one step, recovering both the voltage and the capacity. The findings in this study shed light on the possibility of utilizing other energy forms such as pressure or photon to induce structure and voltage recovery in cycled Li-rich materials. The underestimated role of TM ordering also directs the rational design of future LRLO materials where a stable TM ordering environment is preferred.

Chapter 3, in full, is a reprint of the material, as it appears in: **Li, Y.**, Zuba, M.J., Bai, S., Lebens-Higgins, Z.W., Qiu, B., Park, S., Liu, Z., Zhang, M., Piper, L.F. and Meng, Y.S., 2021. Regeneration of degraded Li-rich layered oxide materials through heat treatment-induced transition metal reordering. Energy Storage Materials, 35, pp.99-107. The dissertation author was the primary investigator and first author of this paper.

Chapter 4. Elucidating the Effect of Borate Additive in High Voltage Electrolyte for Li-rich Layered Oxide Materials

4.1 Introduction

Rechargeable lithium-ion batteries (LIBs) are considered to be one of the most important energy storage devices.[139] With the rapid growth of the electric vehicles market, the demand for high energy density LIBs is increasing.[109] Lithium-rich layered oxide (LRLO) as a high-energy cathode material has attracted many interests due to its large specific capacity (over 300 mAh g^{-1}).[140] Accompanied by Li extraction/insertion during charge and discharge, LRLO experiences not only the transition metal (TM) redox but also the oxygen redox which contributes a large portion to its high capacity.[25] Despite its high capacity, the practical deployment of LRLO is hindered by voltage fade and capacity decay during electrochemical cycling.[141] These two issues are correlated to the activation of oxygen redox at high voltage (> 4.5 V vs. Li^+/Li^0), which leads to surface and structure degradation during cycling, such as the formation of oxygen vacancies and irreversible oxygen loss,[114] the migration and the dissolution of TM,[117] the formation of spinel-like phase,[118] and the accumulation of microstrain.[119] Intensive materials modification efforts have been devoted to addressing the capacity and voltage decay issues in LRLO. Surface coating with oxides or fluorides such as Al_2O_3 and AlF_3 were applied to reduce the oxygen release and protect the surface from acidic species in the electrolyte.[120] Both cation and anion doping such as Mg, Mo, F were also designed to mitigate the capacity and voltage decay through the altering of electronic structure and the suppression of structural degradation.[142] Heat treatment and re-lithiation on cycled LRLO materials were also studied to recover the capacity and voltage decay after electrochemical cycling through the recovery of the honeycomb ordering in the TM layer.[122]

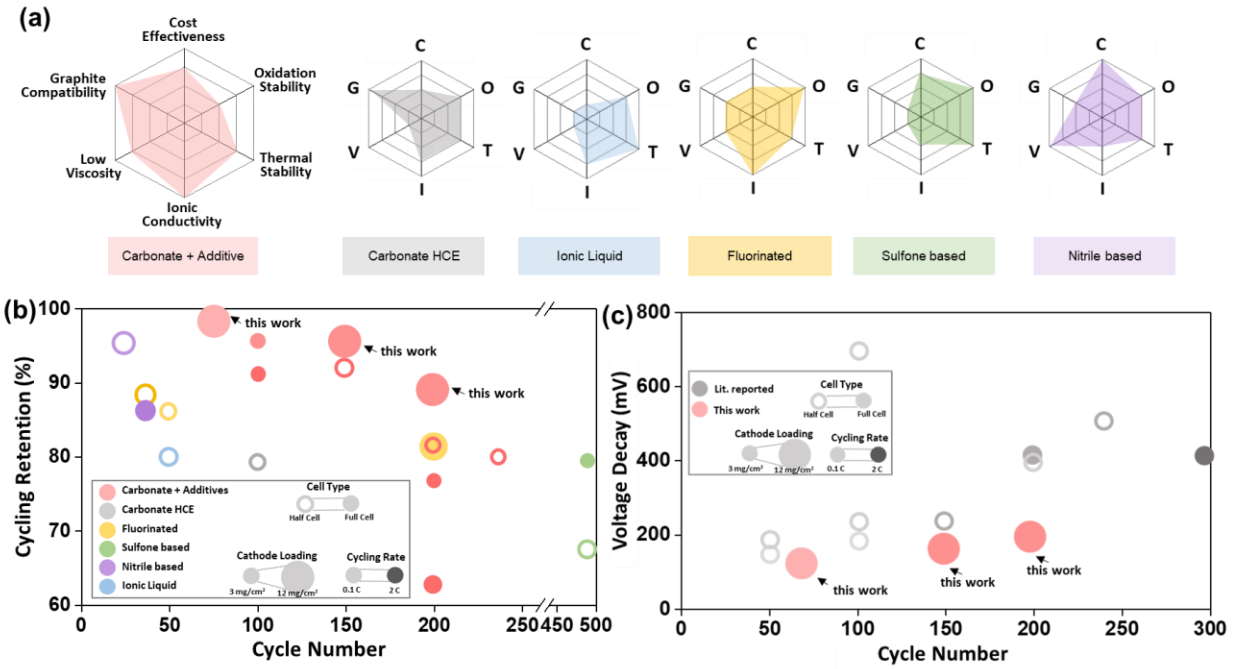

Figure 4.1 (a) Performance metrics comparison of different types of novel high-voltage electrolytes; (b) Literature summary of electrochemical performance of layered oxide materials cycled over 4.5 V in different novel electrolytes; (c) Literature summary of the voltage decay for unmodified LRLO materials over long-term cycling.

Besides the modification on active materials, many cell components have also been optimized for high voltage operation such as the binder and conductive agents.[143] However, the compatibility of the electrolyte with the charged state of LRLO is often neglected in the literature. The activation step ubiquitously seen in anionic redox materials occurs at 4.5 V versus Li^+/Li^0. For the commonly used carbonate-based liquid electrolytes, when the voltage is pushed above this limit (4.5 V), the electrolytes decompose through the following processes: carbonate-based organic solvents such as ethylene carbonate (EC) oxidize and decompose at high voltage, accompanied by dehydrogenation reaction as the protons attached to the carbon in the carbonate solvents are dissociated.[144] The protons may further attack the cathode surface, binding with the oxygen on the cathode surface and generating H_2O.[145] Meanwhile, the autocatalytic decomposition of $LiPF_6$ leads

to the formation of LiF and PF_5. The trace amount of H_2O from the fresh electrolyte and from carbonate solvent decomposition will then further react with PF_5 or $LiPF_6$ to produce acidic species such as HF.[146] In full cells with high voltage cathode and graphite anode, the produced HF will corrode the interphase between electrode and electrolyte, followed by the dissolution of TM from the cathode and its redeposition on the graphite.[37] These problematic behaviors from electrolyte decomposition significantly limit the lifetime of the high voltage batteries. Many different strategies have been explored in the designing of high-voltage electrolytes as shown in Figure 4.1a. Inorganic and organic electrolyte additives were utilized in carbonate-based solvents since the decomposition of such additives may form stable CEI (cathode-electrolyte interphase) and SEI (anode-electrolyte interphase) to avoid further decomposition.[147] This strategy is cost-effective as the amount of additive is usually very low (0.5~5%).[148] Good compatibility with graphite is also observed with this type of high-voltage electrolytes.[149] The utilization of high salt concentration electrolyte (HCE)[150] and the development of ionic liquids as electrolytes[151] have also been explored for high-voltage electrolytes, but both suffer from the high viscosity of electrolyte and in turn the bad wettability with thick electrodes. Fluorinated carbonates were also developed and used as the solvent for high-voltage electrolytes due to their high oxidation stability and thermal stability.[152] However, such fluorinated carbonate solvents are usually more expensive and may bring up the total cost of electrolytes compared to carbonate solvents.[153] Replacement of carbonate-based solvents was also studied for high voltage systems including the utilization of or sulfone-based solvents[154] and nitrile-based solvents[155]. Those solvents are carbonate-free and generally have very high oxidation stability. However, the practical implementation of these electrolytes is challenging, due to the high viscosity in sulfone-based electrolytes and the low ionic conductivity in nitrile-based electrolytes, which make these electrolytes difficult to use for thick

electrodes with high areal capacity loading.[156] As shown in Figure 4.1a, carbonate solvents with electrolyte additives show a balanced performance in different performance metrics required for high-voltage cells, while other strategies come with one or several weaknesses such as poor graphite compatibility, high viscosity, low ionic conductivity, low cost-effectiveness, etc.

In this work, lithium bis-(oxalate)borate (LiBOB) as an additive in the carbonate-based electrolyte was evaluated in LRLO/graphite full cells with thick electrodes (over 3 mAh cm^{-2} areal capacity loading). LiBOB was first synthesized by Xu *et al.*[157] and Lishka *et al.*[158] in two laboratories independently.[159] It shows many promising properties such as high thermal stability, ability to passivate aluminum substrates, and competence to form a stable SEI on graphite anode.[160] Recently, improved cycling stability was observed in many studies when LiBOB additive is utilized for high voltage cathode materials such as $LiNi_{0.5}Mn_{1.5}O_4$ (LNMO),[161,162] $LiCoPO_4$,[163] and LRLO.[164,165] The performance improvement has been attributed to the formation of a passivation CEI containing borate species, which would inhibit the HF attack and electrolyte oxidation at high voltage.[152,166,167] In studies with LRLO/Li cells using LiBOB-containing electrolytes, other mechanisms have also been proposed such as the reduced amount of Li_2MnO_3 phase generation,[51] and the capturing of active oxygen species from the cathode surface.[164] However, the beneficial role of LiBOB for high voltage battery system was mainly studied as its effect on the CEI so far. Not many works on full cells with graphite anode have been reported, not to mention a systematic evaluation of the full cell system including the cathode, the anode, and most importantly, the electrolyte. This is also because most of the literature reported work are conducted in coin cells, which makes it extremely hard to collect any cycled electrolyte for analysis.

In this work, we report the use of LiBOB in an LRLO/graphite full cell system with 3 mAh cm^{-2} capacity loading, in both coin cell and pouch cell formats. A comparison of cell cycling performance with layered oxide materials cycled over 4.5 V between our results and literature reports is shown in Figure 4.1b with detailed information listed in Table 4.1. Our designed full cell shows no capacity decay after 70 cycles at C/10. It also shows a capacity retention of 95.5% after 150 cycles and 89.5% after 200 cycles at C/5. Compared to most of the cells reported in literature with C/2 or even higher rate cycling, our cells with C/10 or C/5 were tested with prolonged time at high voltage, showing its superior cycling stability under extreme conditions. Moreover, the average discharge voltage decay of unmodified LRLO materials is compared between our results and literature reports, shown in Figure 4.1c with detailed information listed in Table 4.2. Our cell shows a voltage decay of 196 mV for 200 cycles (1.0 mV per cycle), which is lower than other reported LRLO materials (usually over 1.4 mV per cycle for long-term cycling).[168–170] A detailed and systematic mechanism study was performed on different components from the cycled full cell including the cathode, the electrolyte, and the anode. We propose that the benefit of LiBOB additive in high voltage cycling comes from its scavenger effect with the HF generated in the electrolyte, and thus leading to less HF corrosion on both CEI and SEI. The well preserved CEI also leads to less cathode surface/subsurface phase transformation and slows down the polarization increase in the cell, which all contribute to the alleviated voltage decay in LRLO cell.[171] With the good protection for both CEI and SEI, less graphite poisoning also take place during cycling, accompanied by the reduced amount of TM dissolution and TM deposition, resulting in the improved high voltage cycling stability in LiBOB-containing electrolyte.

Table 4.1 Literature review on high voltage electrolyte for layered oxide materials.

Composition	Category	Cathode	Loading	Anode	Cycle #	Retention	Rate	Voltage	Ref
1M $LiPF_6$ in EC/DMC(3/7) + 2% LiBOB	Carbonate+Additive	LRLO	12mg/cm2	graphite	70	100%	0.1C	2-4.55V	This work
1M $LiPF_6$ in EC/DMC(3/7) + 2% LiBOB	Carbonate+Additive	LRLO	12mg/cm2	graphite	150	95.5%	0.2C	2-4.55V	This work
1M $LiPF_6$ in EC/DMC(3/7) + 2% LiBOB	Carbonate+Additive	LRLO	12mg/cm2	graphite	200	89.5%	0.2C	2-4.55V	This work
1M $LiPF_6$ in EC/DMC(1/2) + 1% HTN	Carbonate+Additive	LRLO	4mg/cm2	Li	150	92.3%	0.5C	2-4.8V	10.1039/D0SE00175A
1M $LiPF_6$ in EC/EMC/DEC (3/5/2) + 1% PVS	Carbonate+Additive	LRLO	N/A	Li	240	80.0%	0.5C	2-4.8V	10.1016/j.jpowsour.2017.06.075
1M $LiPF_6$ in DEC/EC/EMC(2/3/5) + 1% BTMSC	Carbonate+Additive	LRLO	N/A	graphite	200	77.0%	0.5C	2-4.8V	10.1021/acsami.6b09554
1M $LiPF_6$ in EC/DMC/DEC(1/1/1) + 0.01M LiBOB	Carbonate+Additive	LRLO	N/A	Li	100	96.5%	0.2C	2.5-4.7V	10.1021/acsami.9b07441
1.3M $LiPF_6$ in EC/EMC/DMC(3/4/3) +1% LiDFOB	Carbonate+Additive	LRLO	5mg/cm2	graphite	200	62.5%	0.5C	2-4.7V	10.1039/c5ra18520c
1.3M $LiPF_6$ in EC/EMC/DMC(3/4/3) +1% LiDFOB	Carbonate+Additive	LRLO	5mg/cm2	Li	200	81.4%	0.5C	2-4.7V	10.1039/c5ra18520c
1M $LiPF_6$ in EC/DEC(1/1) +0.5%TMSP+ 0.5%HTCN	Carbonate+Additive	LRLO	N/A	graphite	100	91.8%	0.5C	2-4.7V	10.1016/j.jpowsour.2017.04.094
3M $LiPF_6$ in EC/EMC/DMC(1/1/1)	Carbonate HCE	LRLO	2.5mg/cm2	Li	100	79.0%	0.1C	2 - 4.8V	10.1002/adfm.202009192
0.2M LiTFSI-0.8 M EMIFSI	Ionic liquid	LRLO	4mg/cm2	Li	50	80.0%	0.1C	2.5-4.8V	10.1038/s41467-020-17396-x
1M $LiPF_6$ in FEC/FEMC(1/9)	Fluorinated carbonate	NMC532	10mg/cm2	Graphite	200	81.0%	0.5C	2.8-4.7V	10.1016/j.jpowsour.2020.228791
0.1M $LiPF_6$ in DFDEC	Fluorinated carbonate	LRLO	3mg/cm2	Li	50	86.0%	0.2C	2.5-5.0V	10.1149/2.0591701jes
1.3M $LiPF_6$ in FEC/DMC(1/3)	Fluorinated carbonate	LRLO	6mg/cm2	Li	40	88.7%	1C	2.5-4.6V	10.1002/admi.201700483
0.6M $LiPF_6$ + 0.6M LiFSI FEC/EiPS/FE1(3/50/47)	Sulfone-based	LRLO	N/A	SiO	500	67.0%	0.1C	1.5-4.5V	doi.org/10.2172/1351982
1M $LiPF_6$ in DFEC/FMES(3/7)	Sulfone-based	NMC532	N/A	graphite	500	80.0%	0.33C	3-4.6V	10.1149/08010.0291ecst
1M LiDFOB in ADN/DMC(1/1) + 2% FEC	Nitrile-based	NMC111	7.5mg/cm2	Li	26	95.6%	0.5C	3-4.5V	10.1039/c7ee00035a
1M LiDFOB in ADN/DMC(1/1) + 2% FEC	Nitrile-based	NMC111	7.5mg/cm2	graphite	40	86.0%	0.5C	3-4.5V	10.1149/07701.0011ecst

Table 4.2 Literature review on voltage decay for unmodified LRLO materials.

Composition	Electrolyte	Cathode Loading	Anode	Cycle #	Rate	Voltage	V Decay	V Decay per cycle	Ref
1M $LiPF_6$ in EC/DMC(3/7) + 2% LiBOB	Carbonate+Additive	12mg/cm2	graphite	70	0.1C	2-4.55V	125mV	1.8mV	This work
1M $LiPF_6$ in EC/DMC(3/7) + 2% LiBOB	Carbonate+Additive	12mg/cm2	graphite	150	0.2C	2-4.55V	185mV	1.2mV	This work
1M $LiPF_6$ in EC/DMC(3/7) + 2% LiBOB	Carbonate+Additive	12mg/cm2	graphite	200	0.2C	2-4.55V	196mV	1.0mV	This work
1M $LiPF_6$ in EC/DMC(1/2) + 1% HTN	Carbonate+Additive	4mg/cm2	Li	150	0.5C	2-4.8V	220mV	1.5mV	10.1039/D0SE00175A
1M $LiPF_6$ in EC/EMC/DEC (3/5/2) + 1% PVS	Carbonate+Additive	N/A	Li	240	0.5C	2-4.8V	500mV	2.1mV	10.1016/j.jpowsour.2017.06.075
1M $LiPF_6$ in DEC/EC/EMC(2/3/5) + 1% BTMSC	Carbonate+Additive	N/A	graphite	200	0.5C	2-4.8V	420mV	2.1mV	10.1021/acsami.6b09554
1M $LiPF_6$ in EC/DMC/DEC(1/1/1) + 0.01M LiBOB	Carbonate+Additive	N/A	Li	100	0.2C	2.5-4.7V	223mV	2.2mV	10.1021/acsami.9b07441
3M $LiPF_6$ in EC/EMC/DMC(1/1/1)	Carbonate HCE	2.5mg/cm2	Li	100	0.1C	2 - 4.8V	195mV	2.0mV	10.1002/adfm.202009192
0.2M LiTFSI-0.8 M EMIFSI	Ionic liquid	4mg/cm2	Li	50	0.1C	2.5-4.8V	150mV	3.0mV	10.1038/s41467-020-17396-x
0.1M $LiPF_6$ in DFDEC	Fluorinated carbonate	3mg/cm2	Li	50	0.2C	2.5-5.0V	190mV	3.8mV	10.1149/2.0591701jes
1M $LiPF_6$ in EC/DMC/EMC(1/2/2)	Carbonate	2.5mg/cm2	Li	300	1C	2-4.8V	423 mV	1.4mV	10.1149/2.0251504jes
1M $LiPF_6$ in EC/DMC(3/7)	Carbonate	N/A	Li	200	0.2C	2-4.6V	400 mV	1.7mV	10.1038/s41467-021-23365-9
1M $LiPF_6$ in EC/DMC/DEC(1/1/1)	Carbonate	5mg/cm2	Li	100	0.2C	2-4.7V	700 mV	7.0mV	10.1002/chem.201406641

4.2 Experimental Methods

4.2.1 Electrochemistry Tests

Pristine $Li_{1.18}Ni_{0.18}Co_{0.09}Mn_{0.55}O_2$ sample (denoted as LRLO-UM) is provided by Umicore. The pristine material was mixed with polyvinylidene fluoride (PVDF, Arkema Inc.) and conductive agent (Super C65, TIMCAL Ltd.) with a ratio of 8:1:1 to prepare the electrode. The mix was then well dissolved in a proper amount of N-Methyl-2-pyrrolidone (NMP, ≥ 99%, Sigma-Aldrich) and mixed with a Thinky Mixer (Thinky Corporation) to form the slurry. The slurry was casted onto Al foil and dried at 80 °C in a vacuum oven for 12 hours followed by 1 hour of 120 °C drying at elevated temperature. The electrode was punched into cathode discs with 12.7 mm diameter with a loading of active mass around 12 mg/cm^2. Several other LRLO samples were also studied in this work to show the reproducibility of the cycling performance improvement through LiBOB-containing electrolyte, including $Li_{1.144}Ni_{0.136}Co_{0.136}Mn_{0.544}O_2$ (denoted as LRLO-

NIMTE), $Li_{1.12}Ni_{0.35}Mn_{0.53}O_2$ (denoted as LRLO-UMB), $Li_{1.19}Ni_{0.22}Mn_{0.58}Co_{0.01}O_2$ (denoted as LRLO-UMC), and $Li_{1.14}Ni_{0.35}Mn_{0.52}O_2$ (denoted as LRLO-UMD). Here LRLO-NIMTE is provided by Ningbo Institute of Materials Technology & Engineering (NIMTE); LRLO-UMB, LRLO-UMC, and LRLO-UMD are provided by Umicore. For LRLO/Li half cells, a Li metal chip with 1mm thickness was used as the anode and the cells were assembled as CR2016 coin cells. For LRLO/graphite full cells, both CR2032 and pouch cells were assembled. The graphite electrode used in this work is provided by NIMTE with an active mass ratio at 95%. For CR2032 full cells, the graphite electrode was punched into anode discs with 13 mm diameter and the designed N/P ratio was around 1.13. For pouch-type full cells, the cathode size was 44mm*30mm and the anode size was 45mm*32mm. For all the cells, Celgard 2325 was used as the separator. 1M $LiPF_6$ in EC:DMC = 3:7 (vol%) was obtained from Gotion, USA and is denoted as baseline electrolyte in the following sessions. 1M $LiPF_6$ in EC:DMC = 3:7 (vol%) + 2 wt% LiBOB was mixed from baseline electrolyte and the LiBOB salt (Sigma-Aldrich). This electrolyte is denoted as LiBOB electrolyte in the following sessions. All the coin cells were assembled in the Ar-filled glovebox with moisture control (H_2O < 0.5 ppm) and 50 μL of electrolyte was used for each coin cell. The pouch cells were first assembled in the atmosphere without electrolyte. After that, the pouch cell was moved to a heating tray inside the glovebox antechamber and dried at 80 °C overnight under vacuum before the electrolyte injection. After drying, the dry pouches were moved inside the Ar-filled glovebox without air exposure and 500 μL of electrolyte was injected to each cell. The pouch cells with electrolyte were then vacuum sealed inside the glovebox and moved out for further testing. After assembling, the half cells were tested between 2.0 – 4.8 V at C/20 for the first cycle and C/10 for the rest of cycling (1 C = 250 mA g^{-1}). The coin cell and pouch cell full cells were tested between 2.0- 4.7 V at C/20 for the first cycle (1 C = 270 mA g^{-1}) and 2.0 – 4.55

V at C/10 or C/3 for the rest of cycling. The electrochemical performances of all the cells were tested at room temperature either by Neware Battery Test System (Neware Technology Ltd., China) or Arbin BT2000 instruments (Arbin instrument, USA).

4.2.2 Materials Characterizations

The LRLO-UM/graphite full cells were disassembled inside an Ar-filled glovebox after cycling. All the cell components were separated by plastic tweezer to avoid potential cell shortage. For electrolyte-soaked samples, a pristine electrode is soaked in electrolyte overnight for each sample. To preserve the surface species generated on the electrode during cycling or electrolyte soaking, all the electrode samples were not washed with any solvents after cell disassembling or electrolyte soaking. The unwashed electrodes were stored inside the glovebox before further characterization. Scanning electron microscope (SEM) with energy dispersive X-ray spectroscopy (EDX) was conducted with FEI Apreo to characterize the morphology and elemental distribution of the materials. The samples were briefly (<10 s) exposed to air when transferred inside the SEM. The SEM images were taken with Everhart-Thornley Detectors (ETD) detector with an accelerating voltage of 5.0 kV and a working distance of 10 mm. The EDX data were collected with an accelerating voltage of 20.0 kV and a working distance of 10 mm. For each sample, EDX results are collected with at least 3 spots. X-ray diffraction (XRD) patterns of the materials were collected at 11-BM in Advanced Photon Source (APS) at Argonne National Laboratory with a wavelength of 0.4579 Å. Rietveld refinement was applied to the obtained diffraction pattern using GSAS-II[123] software. X-ray photoelectron spectroscopy (XPS) was performed using a Kratos Axis Supra spectrometer with an Al anode source operated at 15 kV. All the XPS samples were prepared inside an Ar-filled glovebox and transferred to the XPS chamber under N_2 atmosphere. Transmission electron microscopy (TEM) was performed on a field emission gun JEOL2800 at

200 kV with Gatan OneView Camera (full 4k x 4k resolution). Scanning transmission electron microscopy (STEM) and electron energy loss spectroscopy (EELS) was performed on primary particles at the annular dark-field (ADF) mode using a JEOL JEM-ARM300CF at 300 kV, equipped with double correctors. To minimize possible electron beam irradiation effects, EELS spectra presented in this work were acquired from areas without pre-beam irradiation. Note that (S)TEM–EELS was carried out under cryogenic temperature (-180 °C) to minimize beam damage influence on CEI structure/chemistry. To prepare TEM samples, powder samples were dispersed on a lacey carbon grid inside the Ar glovebox. The loading and transferring grids to TEM were carefully executed to prevent air exposure. Cryo-focused ion beam (cryo-FIB) was used to prepare the lamella samples for STEM-EELS analysis through an FEI Scios DualBeam. A platinum protecting layer was deposited on the particle before the milling. A gallium ion beam source was used to mill and thin the sample. The lower operating voltages of the ion beam at 16 kV and 8 kV were used to thin and clean the lamella. The loading and transferring of the lamella to STEM were also carefully executed to prevent air exposure.

4.2.3 Electrolyte Characterizations

After cycling, the pouch cells were cut open in an Ar-filled glovebox and the cycled electrolyte was carefully squeezed out into a plastic microcentrifuge tube and stored inside the glovebox. Inductively coupled plasma mass spectrometry (ICP-MS) was performed with a Thermo iCAP RQ ICP-MS to analyze the elemental concentration in fresh and cycled electrolytes. Since the Li and B amounts in the electrolytes are much larger than Ni, Co and Mn, two different ICP sample preparation recipes were used. For Ni, Co and Mn concentration analysis, 50 µL of the electrolyte was diluted with ICP matrix solution (0.5% HCl + 0.5% HNO_3 in H_2O) to form 3 mL of ICP sample. For Li and B concentration analysis, 10 µL of the electrolyte was diluted with

matrix solution to form 25 mL initial-mixed sample, and 500 µL of the initial-mixed sample were extracted and diluted with matrix solution to form 10 mL of ICP sample. An electrolyte density of 1.2 g/mL was used in ICP-MS calculations. Karl-Fischer Titration (KF Titration) was performed with an AQ-300 Coulometric Karl Fischer Titrator to determine the moisture level in the electrolyte. For each titration, 10 µL of electrolyte was collected with a micro-syringe inside the Ar-filled glovebox. The syringe was then taken out of the glovebox and the electrolyte was injected into the titrator immediately. Two to three titrations were performed on each sample. Nuclear magnetic resonance spectroscopy (NMR) was conducted on electrolytes to analyze the salt species in the electrolyte. The NMR measurements of the electrolyte samples were performed with a Jeol ECA 500 spectrometer. For each NMR sample, 120 µL of electrolyte was mixed with 360 µL anhydrous deuterated dimethyl sulfoxide (d-DMSO) to form a clear solution, and 50 µL of α, α, α-Trifluorotoluene was added to each sample as the reference. The NMR sample was then sealed in an NMR tube inside the Ar-filled glovebox for further measurement. The NMR spectrums were analyzed with MestReNova. All spectrums were calibrated with α, α, α-Trifluorotoluene at -63.72 ppm.

4.3 Results and Discussion

4.3.1 Electrochemical Performance Comparison

SEM images of the pristine LRLO-UM are shown in Figure 4.2a and 4.2b, where spheroid secondary particles with an average size of around 6 µm are observed. Synchrotron XRD pattern was collected for the pristine LRLO-UM for structural analysis. Rietveld refinement was performed on the collected XRD data to characterize the lattice parameters and site occupancies of the pristine LRLO-UM sample, shown in Figure 4.2c and 4.2d. The sXRD pattern can be well indexed to the R-3m space group, with lattice parameter a = 2.8418(3) Å and lattice parameter c

= 14.2470(3) Å. The refined occupancies show a 1.59% Li/Ni mixing between the Li and TM layer. The superlattice peak at 6~7° in 2θ (λ = 0.4579 Å) corresponds to the short-range ordering of Li and TM atoms on a $\sqrt{3}a_{hex.} \times \sqrt{3}a_{hex.}$ honeycomb superlattice within the TM layer.[23] Overall, the LRLO-UM sample shows high material purity and a well ordered layered structure with a small amount of Li/Ni mixing, which serves as a good baseline material in the study.

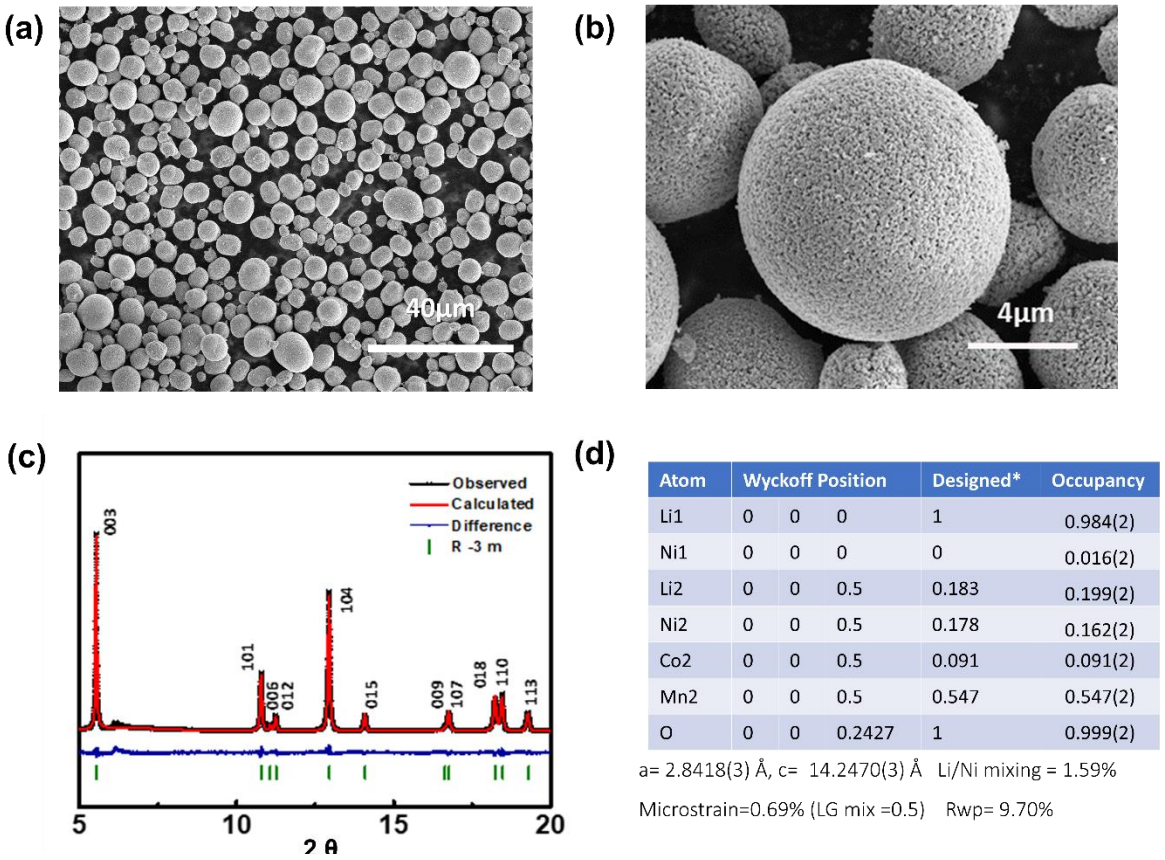

Atom	Wyckoff Position			Designed*	Occupancy
Li1	0	0	0	1	0.984(2)
Ni1	0	0	0	0	0.016(2)
Li2	0	0	0.5	0.183	0.199(2)
Ni2	0	0	0.5	0.178	0.162(2)
Co2	0	0	0.5	0.091	0.091(2)
Mn2	0	0	0.5	0.547	0.547(2)
O	0	0	0.2427	1	0.999(2)

a= 2.8418(3) Å, c= 14.2470(3) Å Li/Ni mixing = 1.59%

Microstrain=0.69% (LG mix =0.5) Rwp= 9.70%

Figure 4.2 (a) SEM image of pristine LRLO-UM materials; (b) SEM image of a magnified LRLO-UM secondary particle; (c) Rietveld refinement of the XRD pattern of the pristine LRLO-UM; (d) Refined crystal structure parameters for the pristine

Electrochemistry tests were performed on LRLO-UM/graphite full cells with both baseline and LiBOB electrolyte. Figure 4.3a shows a similar charge and discharge voltage profile of the initial cycle of the full cells with different electrolytes. Both cells consist of a slope region around

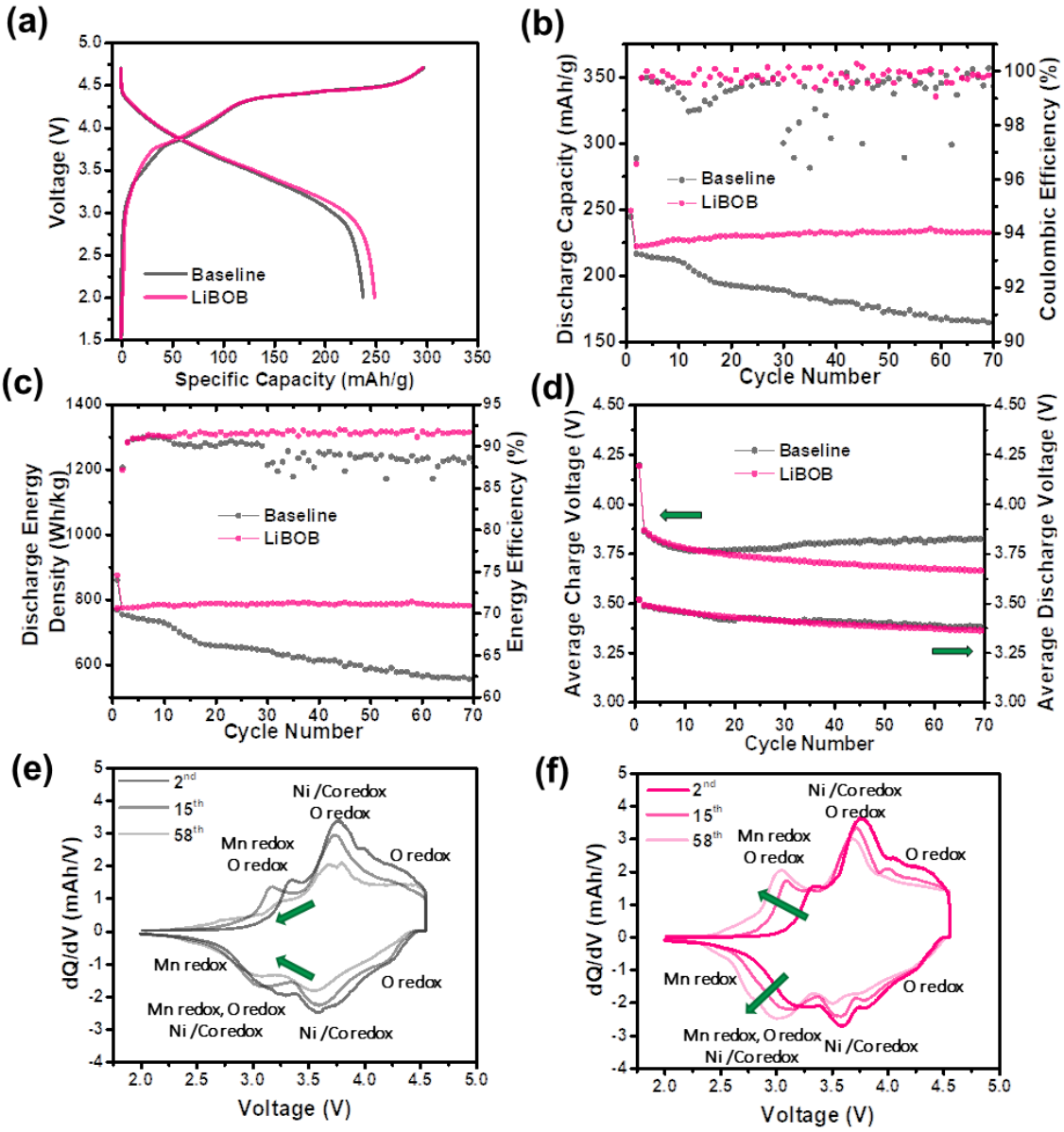

Figure 4.3 Electrochemistry performance of LRLO-UM/graphite full cell with the baseline and LiBOB electrolyte: (a) first cycle voltage profiles, (b) discharge capacity and CE over cycling, (c) discharge energy density and EE over cycling, (d) average charge and discharge voltage over cycling, (e) dQ/dV analysis of cell cycled in the baseline electrolyte, (f) dQ/dV analysis of cell cycled in the LiBOB electrolyte. All cells are 3 mAh cm^{-2} level LRLO-UM/graphite full cells cycled with 2-4.7 V, C/20 for the first cycle, and 2-4.55 V, C/10 for the rest of cycling (1 C = 270 mA g^{-1}).

4.1 V contributed by the TM redox, and a plateau region around 4.5 V ascribed to the oxygen redox.[131,172] At the first cycle, the baseline cell delivers 244 mAh g^{-1} discharge capacity and 858

Wh kg^{-1} energy density with 83.9% Coulombic efficiency (CE). The LiBOB cell delivers slightly higher capacity, energy density, and CE, which is 248 mAh g^{-1}, 874 Wh kg^{-1}, and 84.1%, respectively. The capacity and energy density of the LRLO-UM/graphite cells along with cycling are shown in Figure 4.3b and 4.3c. An obvious improvement of the cycling retention is observed with the LiBOB cell. The LiBOB cell shows no capacity decay within 70 cycles at C/10 rate, compared to 76.3% capacity retention in the baseline cell. It is also observed that the CE and energy efficiency (EE) in the LiBOB cell is higher and more stable than the baseline cell. It is also noticeable that the LiBOB cell shows an Li_2MnO_3 activation period at 1-20 cycles while the baseline cell shows capacity decay from the beginning of cycling.[173] This indicates the continuous Li loss in the baseline cell upon cycling. Similar cycling retention improvements were also obtained with a series of LRLO materials with different compositions in both half cells and full cells, confirming that the LiBOB additive is generally applicable for high voltage LRLO cells. The detailed material information and cycling performance of those cells are shown in **Figure 4.4**. The average charge and discharge voltage and the dQ/dV curves of the LRLO-UM/graphite cells are shown in Figure 4.3d and 4.3f. The average discharge voltage of both baseline and LiBOB cell shows a slight decrease over cycling, which is well known as the voltage decay process for LRLO materials, coming from the structure degradation along with cycling.[21] Such a decay is also reflected as the overall peak shift to the low voltage range in the dQ/dV plots for both cells.[174] From the 2^{nd} to the 70^{th} cycle, the difference between the average charge and discharge voltage decreases 76 mV in the LiBOB cell, but it increases 65 mV in the baseline cell, representing a large increase in the voltage hysteresis and impedance in the baseline cell.[175] In addition, the dQ/dV plot in the baseline cell shows an overall peak area shrinkage over cycling, indicating either the active material or Li inventory loss during cycling. During long-term cycling, the average

discharge voltage decay for the LiBOB cell is only 1.2 mV per cycle, showing the ability of LiBOB electrolyte to alleviating LRLO cathode voltage decay. In summary, the addition of LiBOB in carbonate-based electrolytes evidently improves the cycling stability of LRLO/graphite full cells at high voltage.

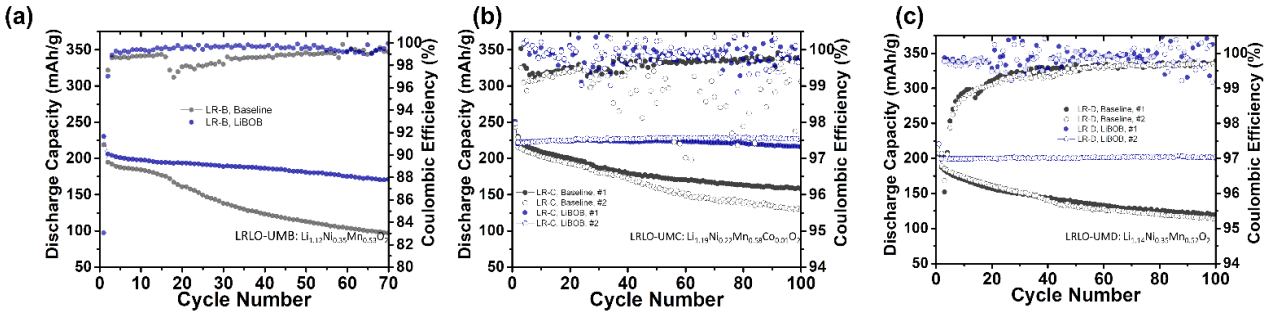

Figure 4.4 Cycling performance for LRLO/graphite full cells with different LRLO cathode materials. All cells were cycled between 2.0-4.7 V at C/20 for the first cycle and 2.0-4.55 V at C/10 for the rest of cycling (1 C=270 mA g^{-1}).

4.3.2 Formation of Conformal CEI

Cryo-(S)TEM and EELS were performed on LRLO-UM cathode to evaluate the CEI formed in different electrolytes. In cryo-STEM sample preparation, a cross-section of the cathode sample is cut by a cryo-FIB, and a lamella of the cross-section is lifted out and thinned down for cryo-EM testing. This workflow can protect the CEI on the surface of spherical cathode particles to the largest extent. Figure 4.5a-c presents the cryo-STEM images of LRLO-UM at the pristine state, after cycling in the baseline electrolyte, and after cycling in the LiBOB electrolyte. At the pristine state, LRLO-UM shows a highly ordered structure with a clean surface. After 70 cycles in the baseline electrolyte, an inhomogeneous CEI layer with an average thickness of 1.5 nm can be observed on the LRLO-UM surface. Some part of this particle surface has a CEI chunk with a thickness of 4.5 nm, while no CEI can be found on some other part. As a comparison, a uniform CEI layer around 3.5 nm in thickness can be found on the LRLO-UM surface after 70 cycles in

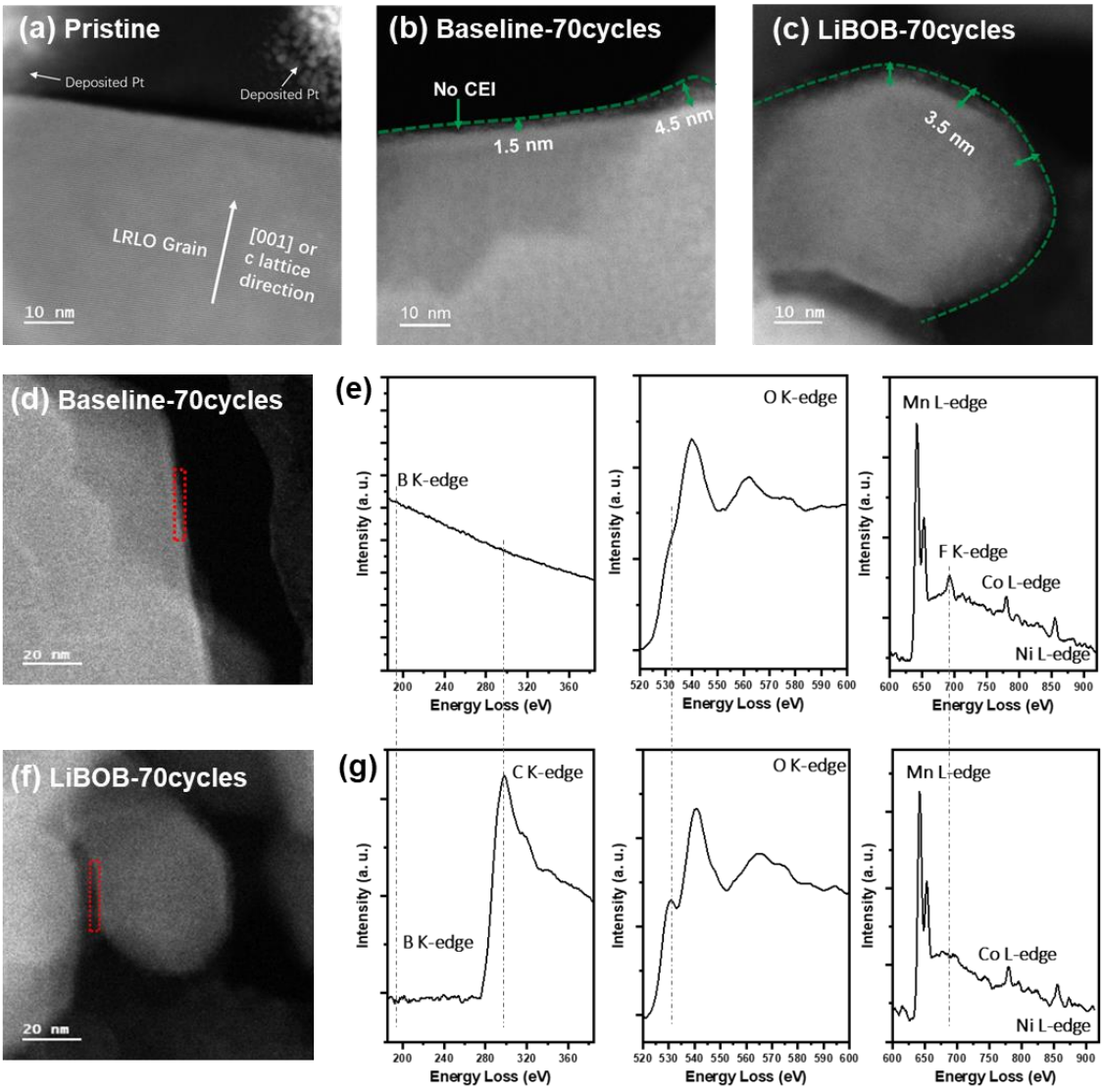

Figure 4.5 Cryo-STEM images of surface and/or CEI region of LRLO-UM cathode samples at different states: (a) pristine, (b) cycled in the baseline electrolyte, (c) cycled in the LiBOB electrolyte. (d)-(e) Cryo-EELS analysis of the CEI in the baseline electrolyte, the EELS spectra in (e) are collected from the red box region in (d). (f)-(g) Cryo-EELS analysis of the CEI in the LiBOB electrolyte, the EELS spectra in (g) are collected from the red box region in (f).

the LiBOB electrolyte. Cryo-TEM samples and cryo-FIB lamella samples were also prepared with the LRLO-NIMTE cathode from the half cells. The corresponding cryo-EM images and analysis are shown in Figure 4.6, where a more uniform and thicker CEI layer can also be observed with the LiBOB electrolyte. It is noticed that in the baseline electrolyte, the material loss and defect spinel phase formation is not limited to the surface, but evolving from the surface to subsurface

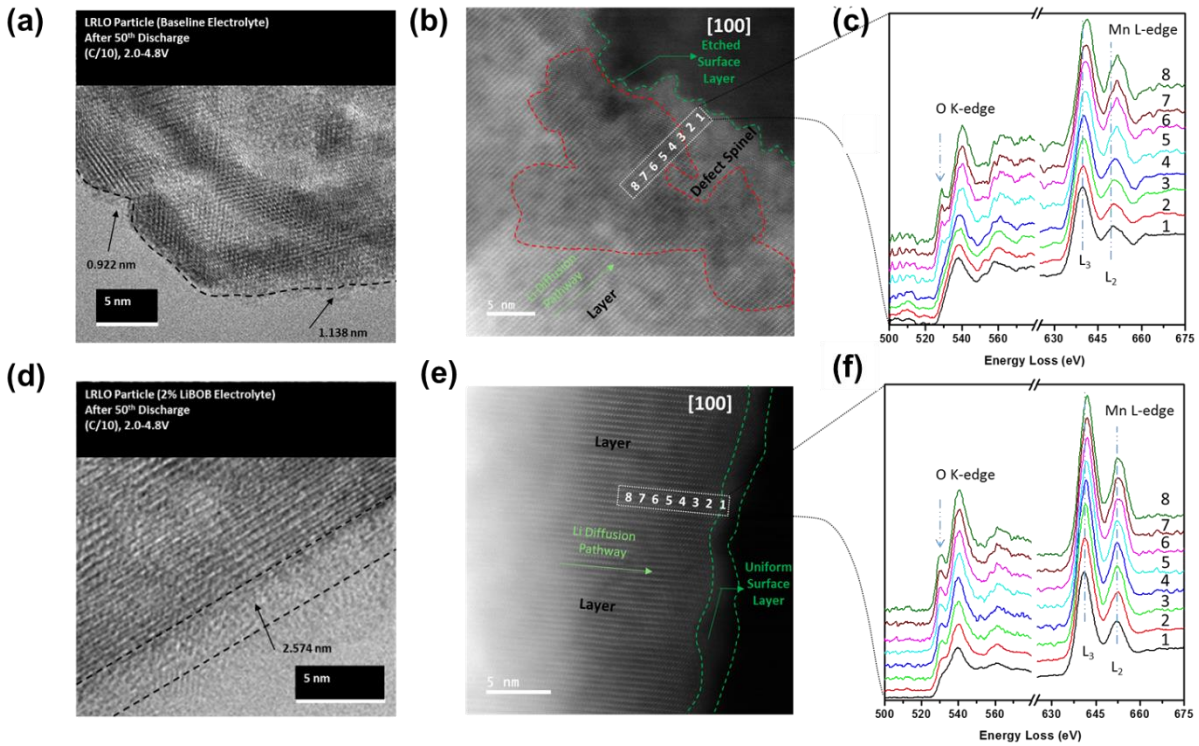

Figure 4.6 Cryo-EM analysis of the LRLO-NIMTE cathode from half cells. (a) cryo-TEM images, (b) cryo-STEM images, (c) cryo-STEM-EELS analysis of the cathode after 50 cycles in the baseline electrolyte; (d) cryo-TEM images, (e) cryo-STEM images, (f) cryo-STEM-EELS analysis of the cathode after 50 cycles in the LiBOB electrolyte.

and even bulk region with a maximum depth around 20 nm. In comparison, the well preserved cathode surface in the LiBOB cell suppresses the surface material loss and surface/subsurface phase transformation, thereby slowing down the polarization increase in the cell and mitigating the cathode voltage decay.[171] XPS analysis for the cathode surface is shown in Figure 4.7. A much lower lattice oxygen peak is observed in the LiBOB cell compared to the baseline cell in Figure 4.7b, indicating the formation of a more conformal CEI layer in the LiBOB cell.[176]

Observations of a thicker and more uniform CEI in the borate additive-containing electrolyte is in good agreement with various previous literature reports on both LNMO[177] and LRLO[178] cathode surface. For many of those studies focusing on the high voltage system, the formation of a good CEI was attributed to the LiBOB salt decomposition upon cycling. Different

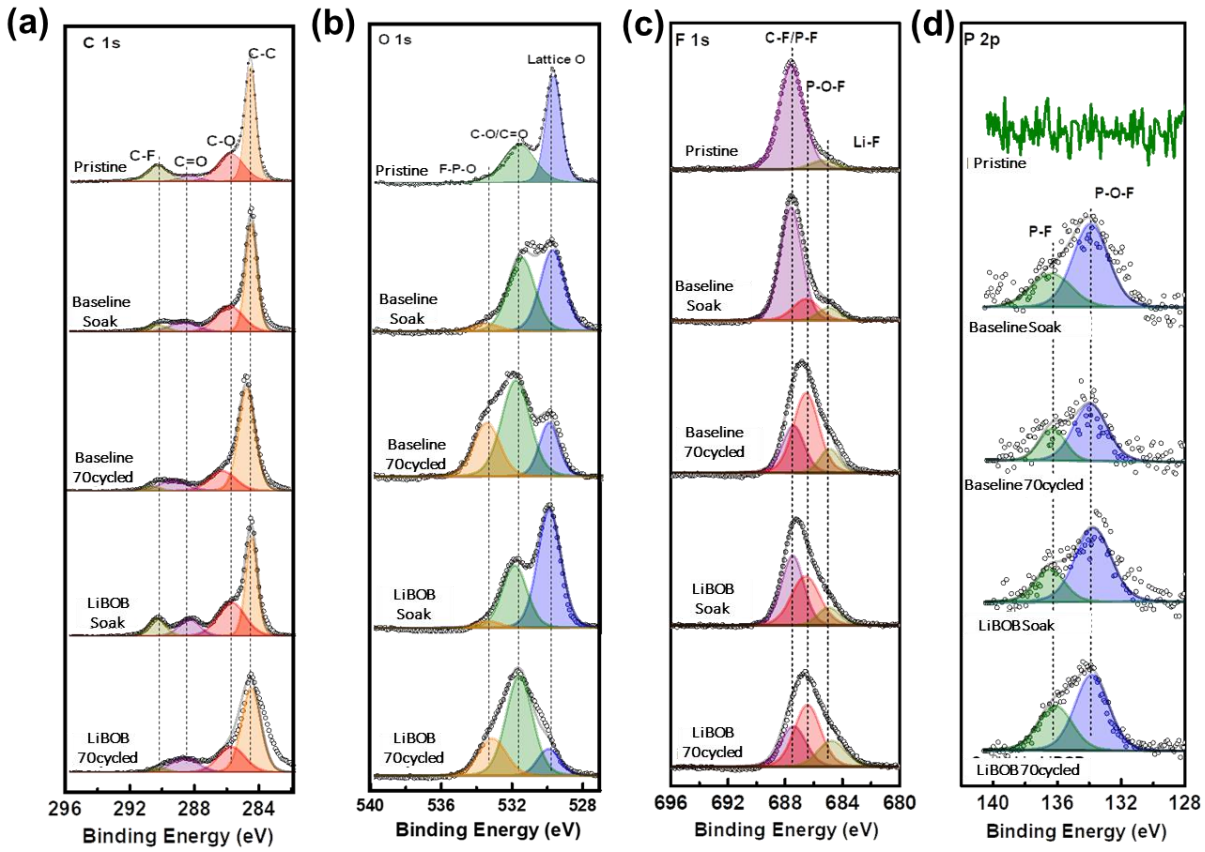

Figure 4.7 XPS comparison of the LRLO-UM cathode at the pristine state, soaked, and cycled in different electrolytes. (a) C 1s, (b) O 1s, (c) F 1s, (d) P 2p spectra.

mechanisms have been proposed in explaining the LiBOB decomposition pathways, such as through the loss of one electron per LiBOB and followed by radical coupling reaction;[179] or through the loss of two electrons per LiBOB and followed by the binding with oxygen radicals.[164] After all, the decomposition of LiBOB would lead to the formation of a CEI layer containing boron species, which serves as a passivation film and slows down the side reactions at high voltage on the cathode and improves the cycling stability. In this work, to obtain the chemical information of the CEI on the cathode surface formed in different electrolytes, cryo-STEM-EELS are collected and shown in Figure 4.5d-g. Surprisingly, no boron signal is found from the CEI in the LiBOB electrolyte at B K-edge. At C K-edge, a large amount of carbon signal can be observed in the

LiBOB cell but not in the baseline cell, implying that at least at this tested location, the carbonate-based CEI is maintained very well in the LiBOB electrolyte. At O K-edge, a clear pre-edge peak can be observed in the LiBOB cell but not in the baseline cell. This pre-edge peak originates from the Mn 3d-O 2p electron orbital hybridization, and the disappearance of this peak in the baseline cell suggests the reduced covalency between Mn and O, corresponding to the surface/subsurface phase transformation.[180] At F K-edge, a clear fluorine signal is observed from the CEI in the baseline electrolyte but not in the LiBOB electrolyte. This fluorine signal in the baseline cell can be a result of HF attacking the cathode surface and the LiF generation,[181] which is in line with the low carbon signal observed at C K-edge as a result of HF corrosion on the CEI. These findings also agree with the increased cell impedance in the baseline cell as suggested in Figure 4.3d, coming from the etched material surface, the surface/subsurface phase transformation, and the accumulation of LiF. To summarize the characterization results for CEI, a thicker and more uniform CEI are formed on the cathode surface in the LiBOB electrolyte, accompanied by less phase transformation of the LRLO-UM material. Surprisingly, this CEI layer in the LiBOB electrolyte does not contain boron-based species. In previous literature reports, the chemical information of the as-hypothesized boron-containing passivation CEI was mainly evaluated through the following evidences: increased semi-carbonate species observed in XPS C 1s spectra,[177] boron signal presented in XPS B 1s spectra,[182] and reduced electrolyte decomposition products confirmed through FTIR[179177]. However, the carbon signal in XPS C 1s and FTIR results are not direct evidence of boron in CEI, hence they may just represent the suppression of electrolyte decomposition and a good preservation of CEI in the LiBOB electrolyte. In addition, B 1s region is intrinsically overlapping with P 2s region in XPS, making it difficult to ascribe the observed signal to boron species or phosphide that are largely contained in $LiPF_6$ based

electrolytes. To the best of our knowledge, this work for the first time employs cryo-STEM-EELS in the analysis of the chemical environment in CEI and confirms that no boron signal is presented in CEI. To locate the boron species after cycling, further characterization is required on other components of the full cell system such as the electrolyte and graphite anode.

4.3.3 B-F Chemistry in LiBOB Electrolyte

To further investigate the underlying mechanism for the cycling stability improvement and the existence of boron species in the LiBOB cell, the cycled electrolyte needs to be carefully

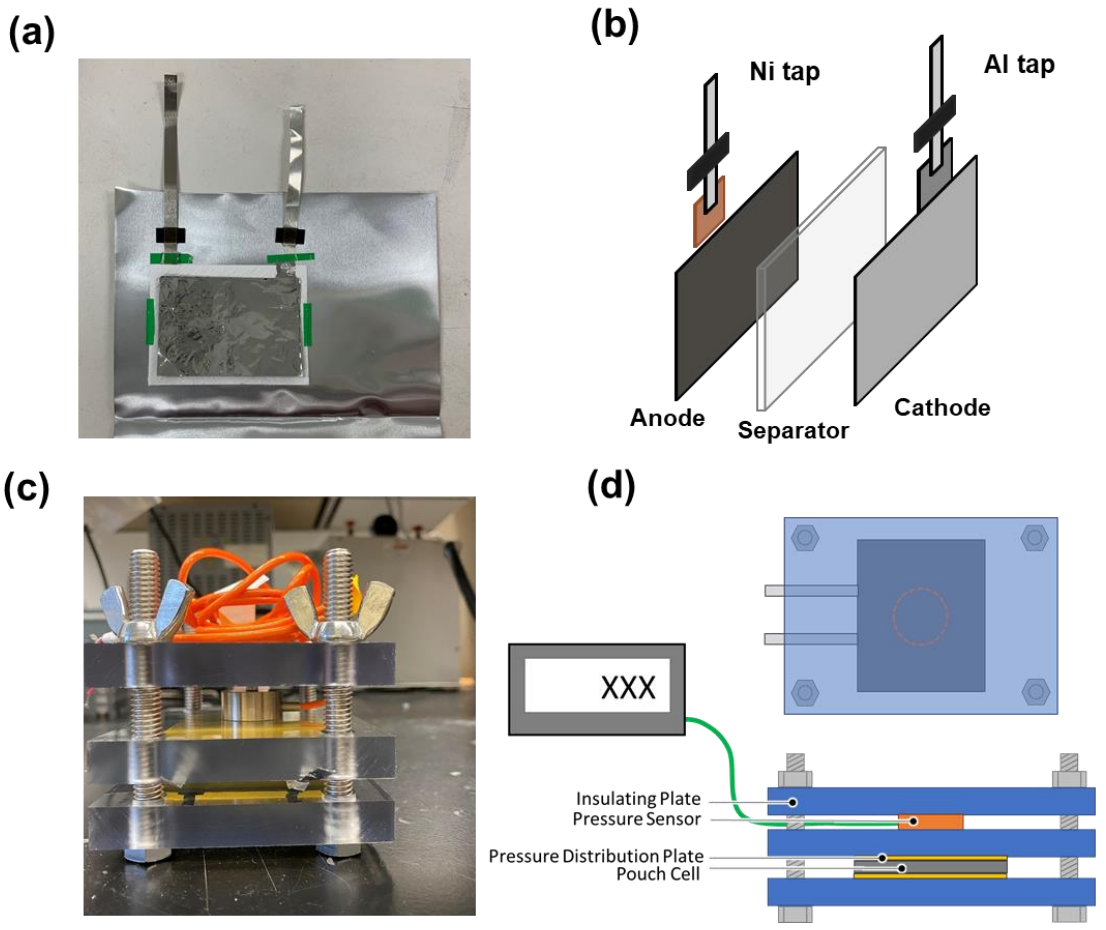

Figure 4.8 Single layer pouch cell design and testing setup. (a) photo and (b) scheme of the dry pouch design, (c) photo and (d) scheme of the pressure controlled single layer pouch cell testing device.

studied. Since it is tough to extract any remaining electrolyte after cycling from coin cells, we fabricated a single-layer LRLO-UM/graphite pouch cell for the electrolyte characterization. The design and testing setup for the pouch cells are shown in Figure 4.8. A stacking pressure of 416 kPa on the electrode area was accurately applied to the pouch cell during the cycling to ensure good electrochemical contact. In the first cycle, the LRNCM/graphite pouch cells deliver a similar discharge capacity compared to the coin cells. For the following cycles, the pouch cells also show a good consistency with the coin cells, where a continuous decay for the baseline cell but a stable cycling for the LiBOB cell is observed. The hysteresis growth in the baseline electrolyte can also be observed in pouch cells. The pouch cells were disassembled after 50 cycles, and the cycled electrolytes were extracted inside the Ar-filled glovebox for characterizations.

ICP-MS was performed on the fresh and cycled electrolytes for elemental concentration analysis, and the results are shown in Figure 4.9a. For both the baseline and LiBOB electrolyte, a lithium concentration around 7-8 g/L is detected at fresh state, in line with the designed 1 M Li salt concentration in the electrolyte. A slight decrease of Li concentration is observed after cycling in both electrolytes, which may be attributed to the loss of Li through CEI/SEI formation.[183] The boron concentration is similar in the LiBOB electrolyte before and after cycling. This indicates that the majority of the boron stays in the electrolyte during cycling, which explains why no boron signal was observed in the cryo-STEM-EELS analysis of the CEI. Further investigation on possible boron species in the electrolyte will be conducted in the latter part of this work. It is also noticed that in the fresh baseline and LiBOB electrolyte, no TM signals can be detected through ICP-MS. After cycling, less TM dissolution, especially less Mn dissolution, is observed in the LiBOB electrolyte. A similar decrease in TM deposition on the anode has also been reported in LNMO/graphite system with LiBOB-containing electrolyte before.[184] KF Titration was performed

with both electrolytes at the fresh state and after cycling, where a similar moisture level is detected across all the samples. However, this does not mean that the same amount of moisture is generated during cycling for both electrolytes because the moisture can react with $LiPF_6$ right after formation.

To further quantify the salt composition in the electrolyte, ^{19}F NMR was conducted on the fresh and cycled electrolytes. Figure 4.9b shows the full range of the ^{19}F NMR spectra, where a strong doublet is observed at −72.4 ppm, corresponding to the $LiPF_6$ salt from the electrolyte.[185]

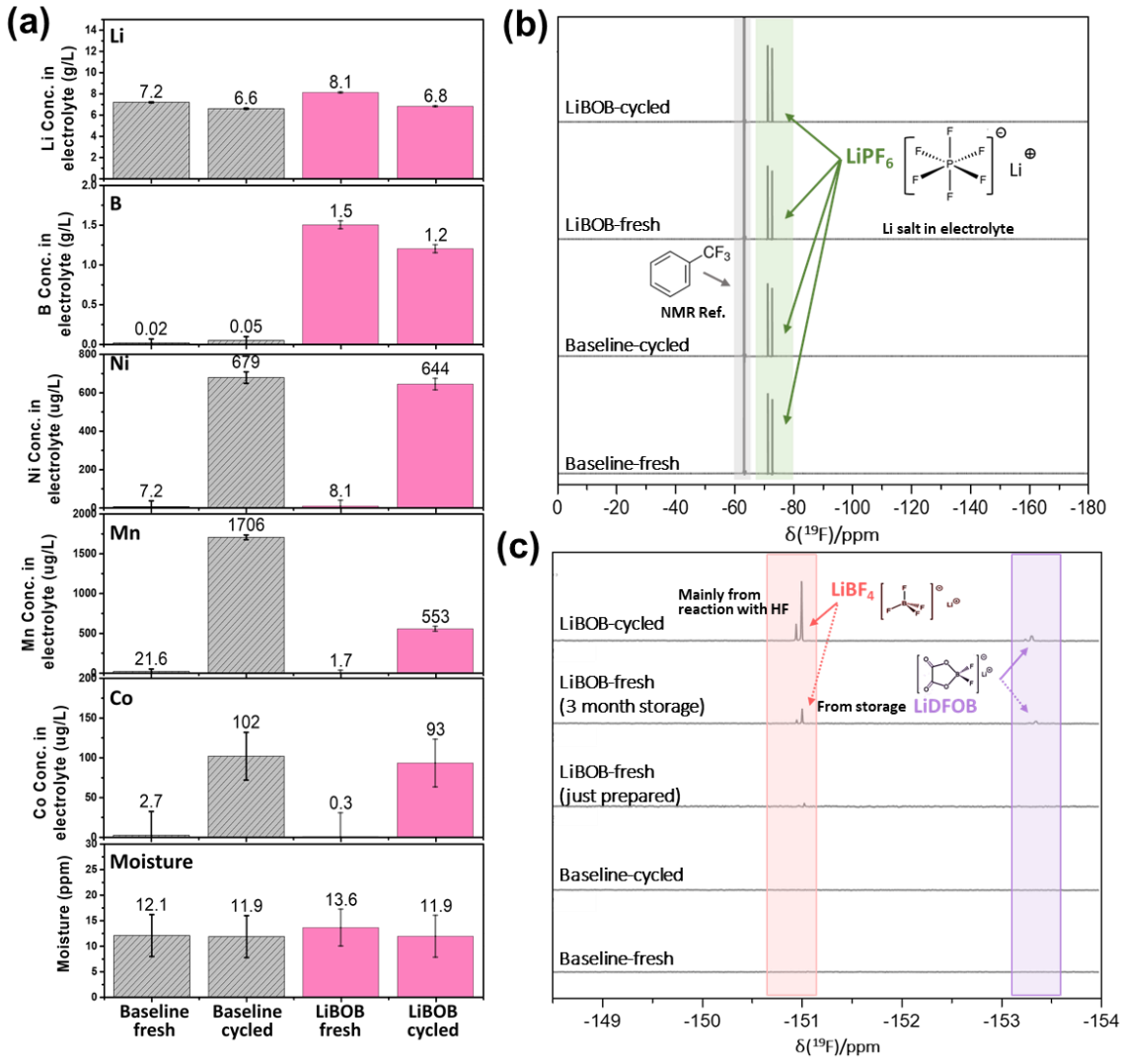

Figure 4.9 Characterizations of the baseline and LiBOB electrolyte at fresh state and after 50 cycles in pouch cells. (a) Element concentration of Li, B, Ni, Co, Mn obtained from ICP-MS and moisture level obtained from Karl-Fischer test, (b) ^{19}F NMR spectra at full scan, (c) ^{19}F NMR spectra at magnified region for B-F bonding.

For baseline electrolyte, the amount of $LiPF_6$ is smaller in the cycled sample compared to the fresh sample, as suggested by the area integration of $LiPF_6$ species shown in Table 4.3. This indicates the $LiPF_6$ decomposition after cycling. Figure 4.9c shows the magnified region around −150 ppm for B-F species.[186] The baseline electrolytes show no signal in this region. The just-prepared LiBOB electrolyte also barely shows any signals. However, clear peaks are seen in the fresh LiBOB electrolyte after storage and grow even higher after cycling. These signals at −150.9 ppm and −153.2 ppm are assigned to lithium tetrafluoroborate ($LiBF_4$) and lithium difluoroborate (LiDFOB), respectively.[187,188] Since only 2 wt% of LiBOB was added to the baseline electrolyte, these B-F peaks are very small compared to the $LiPF_6$ signal. The generation of $LiBF_4$ and LiDFOB in fresh LiBOB electrolyte after storage can be attributed to the effect of the thermal reaction of $LiPF_6$ in presence with LiBOB, where disproportionation reaction happens between the fluoride ligands on phosphorus (in $LiPF_6$) and the oxalato ligands on boron (in LiBOB).[189] Compared to the fresh LiBOB electrolyte after storage, the amount of B-F species largely increases in the cycled electrolyte, indicating that other reactions occur between LiBOB salt and fluoride in the electrolyte under high voltage cycling. During cycling, it is commonly acknowledged that $LiPF_6$ decomposition and PF_5 hydrolysis can lead to the generation of large amount of acidic species such as HF, which corrodes the CEI and SEI in the cell and degrades the battery performance.[190146] When LiBOB additive is used in the electrolyte, it decomposes upon charging. The LiBOB salt or borate radicals from LiBOB decomposition can then directly react with HF, which is the source of $LiBF_4$ observed in NMR. Similar B-F species generation was also reported in $LiNi_{0.5}Mn_{0.3}Co_{0.2}O_2$ (NMC532) anode-free pouch cells using other borate additives in the electrolyte.[188191] In summary of the CEI and electrolyte characterizations, the majority of B stays in the electrolyte during cycling rather than forming a B-enriched CEI on the cathode surface.

Upon cycling, LiBOB in the electrolyte serves as the HF scavenger that inhibits the generation of HF and its corrosion on the interphase, leading to less TM dissolution from the cathode surface. In other words, the observed uniform and stable CEI in the LiBOB-containing electrolyte is the result of reduced HF corrosion.

Table 4.3 Peak area integration in ^{19}F NMR for different electrolytes.

Sample	$LiPF_6$ Absolute Area	Ref Absolute Area	Ref Peak Normalization	$LiPF_6$/Ref
Baseline fresh	60.79	322.81	1	0.188
Baseline cycled	53.98	316.70	1	0.170
LiBOB fresh	66.74	328.84	1	0.203
LiBOB cycled	66.24	327.69	1	0.202

4.3.4 Mitigated TM Dissolution and Redeposition

A reduced amount of HF in the electrolyte would also lead to less corrosion of the SEI and less TM deposition on the graphite anode, which will be further characterized in this section. EDX was performed on the graphite electrodes to measure the elemental distribution on the graphite surface, shown in Figure4.10a and 4.10b. At the pristine state, only carbon and copper (current collector for graphite electrode) signals are detected. After cycling, EDX suggests the appearance of oxygen, fluorine, phosphorus, manganese, cobalt, and nickel on the graphite surface in both electrolytes. The TM (Mn, Co, Ni) signals are much less on the graphite cycled in the LiBOB cell than in the baseline cell, indicating less TM deposition on the graphite in the LiBOB electrolyte. This is in good agreement with the ICP-MS analysis of the electrolyte, where less TM dissolution was also observed in the cycled LiBOB electrolyte. The overall mass loss from the cathode side is less in the LiBOB electrolyte compared to the baseline electrolyte, also contributing to the improved cycling stability of the LiBOB cell. Moreover, the fluorine amount on graphite surface

in the baseline electrolyte is higher than that in the LiBOB electrolyte, which is in line with the STEM-EELS results on the CEI side. The high fluorine signal on both CEI and SEI analysis suggests more $LiPF_6$ decomposition and HF corrosion in the baseline electrolyte.

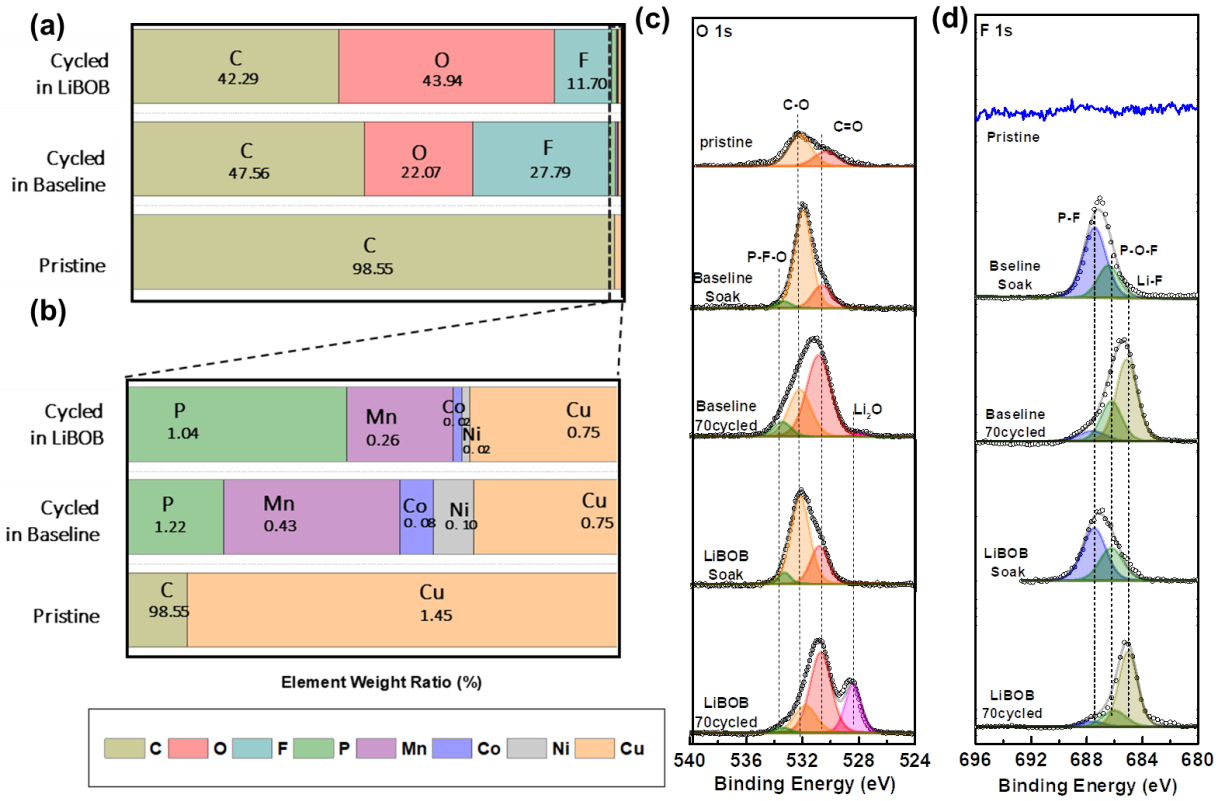

Figure 4.10 Characterization of SEI species on graphite at the pristine state, cycled in the baseline electrolyte, and cycled in the LiBOB electrolyte from the LRLO-UM/graphite full cells. (a) Element weight ratio obtained from SEM-EDX; (b) Magnified region from Figure 5(a) for TM deposited on the graphite surface; (c) XPS comparison at O 1s spectra; (d) XPS comparison at F 1s spectra.

XPS is employed to further explore the surface chemistry of graphite at the pristine state, soaked and cycled in both electrolytes. Figure 4.10c and 4.10d shows the O 1s spectra and the F 1s spectra. For O 1s spectra, the peaks at 533.8 eV, 532 eV, 530.7 eV, and 528.3 eV are assigned to P-F-O ($Li_xPF_yO_z$ from $LiPF_6$ decomposition), C-O, C=O, and Li_2O species, respectively.[192] A large amount of Li_2O can be found in the cycled LiBOB cell but not in the baseline cell. Since

Li_2O is a common component for SEI and is highly sensitive to the presence of HF and H_2O,[193] the higher amount of Li_2O in the LiBOB electrolyte indicates a better SEI formation and lower moisture/HF level in the LiBOB cell. For F 1s spectra, the peaks at 687.8 eV, 686.1 eV, and 685 eV are assigned to P-F (from $LiPF_6$), P-O-F ($Li_xPF_yO_z$ from $LiPF_6$ decomposition), and LiF species, respectively. No F species are detected on the pristine graphite surface. After cycling, the generation of LiF and $Li_xPF_yO_z$ are observed on graphite surface cycled in both electrolytes, but the amount of $Li_xPF_yO_z$ is much less in the LiBOB case, indicating less $LiPF_6$ decomposition.

4.3.5 Elucidating the HF Scavenger Effect of LiBOB

To summarize the characterization results on the different components of the LRLO-UM/graphite full cell system, a mechanism for explaining the improved high voltage cell performance in LiBOB electrolyte is proposed and illustrated in Figure 4.11. The decomposition of carbonate-based electrolyte at high voltage is shown in Figure 4.11a with EC molecules as an example. During the high voltage charge process, electrons are extracted from the cathode as Li ions move out of active materials. However, such high voltage may also pull electrons from EC and cause the oxidation and structure breaking of EC molecules.[194] With the ring opening of EC, the formation of CO_2 gas and the generation of free protons also take place with the participation of trace amount of H_2O in the fresh electrolyte.[195–197] The generated free protons may further attack the cathode surface, binding with the oxygen on the cathode surface and generating more H_2O.[145] The H_2O will then hydrolyze the $LiPF_6$ salt or PF_5 in the electrolyte and form HF, which would, in turn, corrode the CEI and the oxide cathode to generate even more H_2O.[146] These reactions form a vicious circle and contribute to a large portion of cell performance degradation. Since HF can continuously corrode both the CEI and SEI during cell cycling, the cell will suffer from lithium inventory loss as to compensate for the continuous new CEI/SEI formation. Furthermore, as the

cathode oxides get corroded, some TM cations dissolute to the electrolyte and deposit on the graphite, which contributes to graphite poisoning.[37] This is also referred to as the cross-talk between cathode and anode in full cells.[73] The left part in Figure 4.11b summarizes these cell degradation factors in the baseline electrolyte including HF generation and corrosion on cell components, CEI/SEI damage and regrowth, TM dissolution and redeposition, graphite poisoning, etc. The generation of HF plays a crucial role in performance degradation and leads to poor cycling performance for high voltage cells. In this work, we seek to clarify the mechanism for the improved cycling stability for high voltage cells with the borate additive-containing electrolytes. Our results are highly consistent with many previous literature reports on high voltage cathode materials that a more uniform and thicker CEI can be detected on the cathode surface in the borate-containing electrolytes. However, the uniform CEI may be the result of less HF attack, instead of the reason for preventing HF corrosion as suggested in many papers. Through a series of characterization tools on the cathode, the electrolyte, and the anode component in the full cell system, HF corrosion is found to be the main cause of CEI and SEI damage in carbonate-based electrolytes, and borate additives can effectively improve the cell cycling performance by suppressing the HF corrosion. This mechanism is depicted in the right part of Figure 4.11b. When LiBOB presents as an additive in carbonate-based electrolytes, the LiBOB salt or borate radicals from LiBOB decomposition can effectively serve as the HF scavenger through the formation of B-F species. Note that the formation energy of BF_4^- (-1710 kJ/mol)[198] is much lower than HF (-273 kJ/mol)[199], so this reaction would be thermodynamically favorable. In addition, B-F (613 kJ/mol) has much higher bond energy than H-F (565 kJ/mol) and P-F (490 kJ/mol), meaning that the B-F bond is more stable than H-F and P-F bond.[200] This is also in line with the increased stability of $LiBF_4$ than $LiPF_6$ reported in literature.[201] As a result, less HF corrosion happens in LiBOB electrolyte, leading to the presence

of uniform CEI/SEI layers in the cell. The well preserved CEI/SEI then result in a reduced amount of cathode surface/subsurface phase transformation and less voltage decay as well as less TM dissolution and deposition in the cell, which all contributes to the improved cell cycling stability in the LiBOB electrolyte.

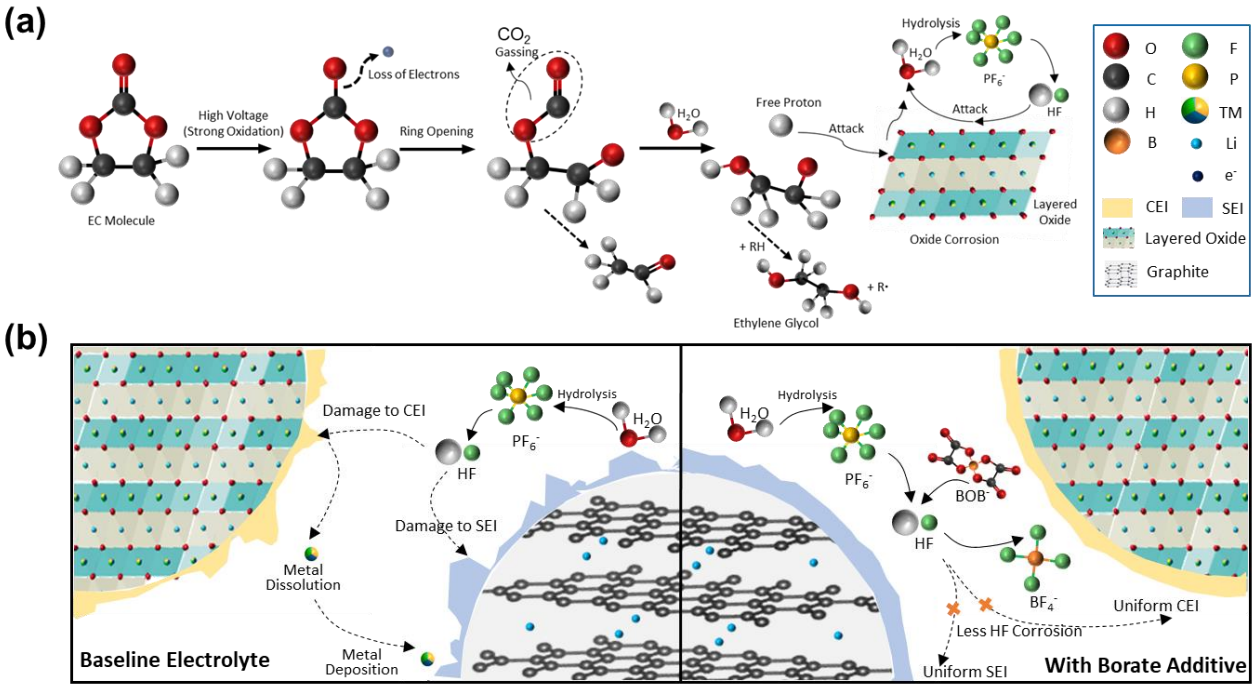

Figure 4.11 Schematic of (a) carbonate-based electrolyte decomposition in high voltage layered oxide system using EC as an example; (b) enhanced cell performance for borate additive electrolyte in high voltage full cell system.

4.4 Conclusions

LiBOB is studied as an electrolyte additive in a high voltage full cell system with LRLO cathode and graphite anode with 3 mAh cm^{-2} areal capacity loading. With 2 wt% of LiBOB added to the carbonate-based electrolyte, the LRLO-UM/graphite full cell shows 25% more capacity retention in the LiBOB-containing electrolyte than in the baseline electrolyte after 70 cycles. After 150 cycles with C/5, the cell only exhibits 185 mV voltage decay and can still deliver 95.5% of its

original capacity. The mechanism for the cycling stability improvement with the LiBOB electrolyte is studied with a systematic analysis of the cathode, the electrolyte, and the anode from the cycled full cells. Cryo-EM and XPS confirm less surface/subsurface phase transformation and a more uniform and thicker CEI on cathode surface in the LiBOB electrolyte, which may be beneficial in stabilizing the polarization increase in the cell and mitigate the voltage decay in cathode. However, this CEI is not boron-based and the majority of boron stays in the electrolyte after cycling. NMR confirms the generation of LiDFOB and $LiBF_4$ in the electrolyte during cycling, which comes from the reaction between LiBOB or borate radicals and HF generated from electrolyte decomposition. The reduced amount of HF corrosion in the LiBOB electrolyte also leads to a more uniform SEI on the graphite surface. With less HF attack on both CEI and SEI, less TM dissolution into the electrolyte and less TM deposition on the graphite is observed in the full cell with LiBOB electrolyte. Overall, LiBOB serves as the HF scavenger in high voltage cells, which leads to less HF corrosion on both electrodes and therefore improved cycling stability in LRLO/graphite full cells. These findings may also be applied to other high voltage systems besides layered oxides, such as spinel LNMO or $LiCoMnO_4$, olivine $LiCoPO_4$, etc., thus opening a door for the commercialization of those high voltage materials. This work also inspires the future exploration of other scavenging materials that can stabilize the $LiPF_6$-containing carbonate-based electrolytes through the elimination or deactivation of the reactive substances generated in electrolyte decomposition processes.

Chapter 4, in full, is a reprint of the material, as it appears in: **Li, Y.**, Li, W., Shimizu, R., Cheng, D., Nguyen, H., Paulsen, J., Kumakura, S., Zhang, M. and Meng, Y.S., 2022. Elucidating the Effect of Borate Additive in High-Voltage Electrolyte for Li-Rich Layered

Oxide Materials. Advanced Energy Materials, 12(11), p.2103033.The dissertation author was the primary investigator and first author of this paper.

Chapter 5. Conclusion and Future Perspectives

5.1 Summary of the Thesis

The rapid market growth of EVs and portable electronics requires the development of LIBs with high energy density, wide working temperature, long cycle life, and high cost-effectiveness. For EV applications, the highest cell level battery gravimetric and volumetric energy densities achieved to date are 250 Wh kg^{-1} and 670 Wh L^{-1}, respectively (based on 18650 cylindrical cells in Tesla Model 3).[202] However, to allow a driving range beyond 500 km, the energy densities in LIBs are required to reach approximately 350 Wh kg^{-1} and 750 Wh L^{-1} at cell level.[203,204] Therefore, the energy density and cycling life of current LIBs must be further extended to meet the EV application requirements. As an important component of LIBs, cathode material to a large extent determines the electrochemical performance of the cell. Classical NMC layered oxide, especially with high Ni content, is one of the most successful cathode materials due to their high reversible capacity and good rate capability. However, the upper voltage cut-off for high-Ni NMC materials is usually limited to below 4.2 V, which makes the practical capacity of these materials much smaller than the theoretical value. Increasing the operating voltage can achieve higher capacity but is accompanied by severe structural transformation at particle surface and microcrack formation at both intragranular and intergranular level, leading to rapid capacity decay over cycling. Another approach to push the energy density limit in cathode materials is to explore new compounds beyond classical layered NMC materials. As we discussed in the chapters above, one of the most promising next-generation high energy cathode material is LRLO, which is also constructed based on the intercalation chemistry and shares the similar layered structure as NMC. The "extra" Li occupying the *3a* TM site leads to the special Li-

O-Li configuration in the structure and contributes to the reversible oxidation and reduction of the non-bonding oxygen.[131] Despite the high discharge capacity, LRLO materials suffer from the capacity and voltage fade rooted in the structure instability. In addition, compared to NMC, LRLO operates with a much higher upper voltage cut-off of around 4.6 V, which brings a series of interphase related problems. The high voltage in the cell induces significant amount of electrolyte decomposition and acidic species generation, which corrodes both the CEI and SEI and leads to parasitic crosstalk reactions.

The focus of my thesis is to investigate the degradation mechanisms and to explore the mitigating strategies for lithium transition metal layered oxides, including both classical layered NMC materials and LRLO materials. Various advanced analytical characterization techniques were adopted in my work to capture the changes inside the cathode, on the cathode surface, or on the CEI during cycling. **Chapter 2** focuses on understanding and alleviating the capacity decay problem in multiple classical NMC materials through the design of controlled TB defects. The radially aligned TB defects maximize the particle exposure to the electrolyte with the more stable (003) planes. Increased cation disorder and the formation of rocksalt-like phase are consistently observed along the TBs through STEM, acting as a rigid framework that mitigates anisotropic changes in NMC during cycling. *Operando* XRD confirms this hypothesis as the degree of anisotropic changes is minimized in NMC with TBs. The synthesized NMC materials with TB defects exhibit enhanced electrochemical performance compared to the corresponding micro-sized materials with identical composition. The TB defects engineering in NMC structure can effectively suppress the phase transformation and material degradation, serving as a novel

and universal approach in designing stable intercalation compounds for high voltage long-cycle life LIBs.

In **Chapter 3**, heat treatment and ambient-air relithation was applied to cycled LRLO materials to recover the decayed voltage and capacity. In this work, a detailed mechanism study of the voltage and structure recovery is conducted through NPD, PDF, EXAFS, and computation. We discovered that heat treatment provides the necessary energy for TM to overcome the kinetic barrier to move from honeycomb center to honeycomb vertex and recover the honeycomb ordering in the TM layer. An ambient-air relithiation using Li^+ molten salt was also conducted along with the heat treatment to the cycled LRLO cathode and lead to a material regeneration in both the voltage and capacity. This work identifies the TM reordering as the key factor under the structure recovery of degraded LRLO materials. It opens a door for the promising strategies to mitigate the voltage and capacity degradation problem in LRLO and provides a potential route to recycle degraded LRLO materials.

In **Chapter 4**, we report the use of LiBOB as an electrolyte additive to improve the cycling stability in LRLO/graphite full cells. The cell with LiBOB-containing electrolyte delivers 95.5% retention after 150 cycles over 4.5 V cycling. A systematic mechanism study for the LiBOB-enabled cycling performance improvement was conducted. Analytical EM under cryo-condition confirms the formation of a uniform CEI and less phase transformation on the LRLO particle surface, accompanied by less voltage decay in the cathode. The formation of B-F species is identified in the cycled electrolyte with NMR, elucidating the HF scavenger effect of LiBOB. Due to less HF corrosion on both CEI and SEI, a reduced amount of TM dissolution and redeposition on the graphite has been observed through SEM-EDX, ICP, and XPS. The capacity decay in LRLO/graphite full cells is thus mitigated. These findings suggest that the borate additive is a

promising strategy to optimize high voltage electrolyte for the industrialization of LRLO. It also inspires the future exploration of other scavenging materials that can stabilize the $LiPF_6$-containing carbonate-based electrolytes.

In summary, this thesis provides a thorough study of the degradation mechanisms and mitigation strategies in lithium transition metal layered oxides. Degradation is overall a complicated process involving different aspects of the cathode material. Therefore, advanced analytical characterization tools are needed to deconvolute the contribution from different degradation pathways and take up a large portion of this thesis. In the next section, we will discuss some potential directions following up the work presented in this thesis as well as some limitations that could be addressed in the future studies.

5.2 Future Perspectives

5.2.1 Defect Engineering in Cathode Materials

The first thing to discuss in this perspective section is the role of defect engineering. As mentioned in Chapter 2, a lot of previous literature focused on the negative effects of defects generated during electrochemical cycling. The uncontrolled and heterogeneous defects formed during cycling such as Li-Ni anti-site,[78] stacking faults (SF),[79] anti-phase boundaries (APB)[80] are usually correlated with the performance decay of the cathode materials. In recent years, however, the field starts to realize that the designed and well-controlled defects in the cathode materials may play a crucial role in enhancing their electrochemical performances.

Crystallographic defects are generally categorized into three groups based on their dimensionality, i.e., point defects, linear defects, and planar defects.[205] Common point

defects explored in battery materials include the substitutional sites, interstitial atoms, and TM or oxygen vacancies. While Li/Ni anti-site defect is a commonly acknowledged detrimental point defect which hinders Li^+ transport,[78] there are also many studies exploring the beneficial effects of point defects. For example, substitutional atoms such as Al^{3+} or Ti^{4+} doping has been proved as an effective approach in improving structure stability for layered oxides.[39,206,207] In spinel LNMO, interstitial Al^{3+} taking the empty *16c* octahedral sites can suppress TM dissolution without interfering Li^+ mobility.[208] Our group's own work on introducing well-controlled oxygen vacancies on LRLO surface also brought beneficial effects to LRLO such as preventing gaseous oxygen evolution and promoting Li^+ diffusion.[41] Linear defects, such as edge dislocation, is discussed more as the reason for intragranular crack formation and phase transformation for cathode materials during cycling.[209] The formation of edge dislocation network was also reported in LRLO and recognized as one of the origins for voltage fade.[34] However, the dislocation network in $LiNi_{0.5}Mn_{1.5}O_4$ (LNMO) was reported to cause the decrease of Poisson's ratio during delithation and could explain why LNMO is resistant to oxygen loss at high voltage.[210] Planar defects have been discussed more thoroughly in Chapter 2, where TB, APB, and SF defects were compared. Among these planar defects, TB is a unique type of defect that does not necessarily hinder the ionic diffusion and can potentially enhance the electrochemical performance in cathode materials. Our work on a series of TB-containing NMC materials shows that TBs can act as a rigid framework to improve NMC cycling stability by mitigating the anisotropic lattice changes during cycling.[211] TB defect engineering has also been studied in $LiMn_2O_4$ spinel materials, where agminated Li atoms are found occupying

the Mn sites around the TBs, enabling fast Li-ion diffusion and excellent fast charging performance.[205]

Topological defects can largely affect electrochemical performance in cathode materials through altering their mechanical and electronic properties. To follow up with our work on the TB-NMC materials, the following research directions are proposed. First direction is the synthesis of micron-sized single crystal (SC) NMC with TB defects. Current TB-NMC materials are synthesized with polyol method, where only nano-sized particles were achieved (particle size < 200 nm). Bruce *et al.* reported in LMO materials that the high porosity in nanoparticles would simultaneously increases parasitic side reactions between the electrode and electrolyte, thus impeding cell performance during cycling.[212] One potential direction is to optimize the polyol synthesis procedure to obtain SC TB-NMC. SC NMCs have been widely reported in literature as an effective method to eliminate the risk of intergranular fracture in polycrystalline particles.[213] The micron-level particle size also alleviates the problem of intense surface side reactions happening in nano-sized particles. While many SC NMCs reported in literature are synthesized through solid state method,[214,215] Zhang *et al.* reported a hydrothermal method that is relatively close to our polyol method used in Chapter 2.[216] By altering reaction temperature, increasing reaction time, and/or changing reaction solvent, it is highly possible that micron-sized SC TB-NMC materials can be synthesized and will further increase the cycling stability of this series of materials. Another future direction is using polyol synthesis to incorporate dopants in NMC and LRLO materials. Many works in literature, including our group's computation results, predict that certain dopant can effectively increase the cathode material performance.[49] Many dopant precursors are metal oxides that require high temperature (> 1000 °C) to melt,

which may interrupt the thermal stability of cathode materials if synthesized at this high temperature. On the other hand, when using lower reaction temperature (< 900 °C), these dopants cannot be incorporated into the cathode structure uniformly and form a pure phase. However, polyol method can synthesize nano-sized dopant precursors which can further react with the cathode precursor and Li source in the calcination process. The nano-sized dopant precursors can promote a fast and homogeneous reaction and reduce the synthesis temperature, which will yield uniformly doped materials with enhanced electrochemical performance. In addition, polyol method may directly incorporate the dopant elements into cathode precursor synthesis and avoid adding dopant metal oxide in the future calcination step, which should also yield pure materials without elemental segregation.

5.2.2 Novel Electrolyte Design for High-Voltage Cathode Materials

In Chapter 4, we revealed that the high voltage cell degradation is rooted from the electrolyte instability and the crosstalk reactions happening in the cell during cycling. Our work in Chapter 4 identifies the HF scavenger effect of LiBOB and shows a much-improved cycling stability for LRLO with 2 – 4.55 V voltage cutoff during cycling. However, carbonate-based solvents plus scavenger-type additive may not be a sufficient solution when pushing the cell charge voltage to even higher or cycling the cell at elevated temperatures (> 55 °C). For example, spinel LNMO has an operating voltage of 4.7 V. The high operating voltage and the capability to handle high charging rates make LNMO a desirable cathode candidate for the EV industry. More recently, the strong desire to eliminate cobalt in cathode materials has sparked immense interests in this class of oxides. However, such high operating voltage causes much easier dehydrogenation of the carbonate-based solvents as well as easier $LiPF_6$ hydrolysis, which leads to more aggressive

crosstalk reactions in the cell and faster cell decay. Various attempts have been carried out in designing novel electrolytes with high oxidative stability to accommodate high voltage cycling, including the use of fluorinated solvents[152], sulfone-based solvents[154], nitrile-based solvents[155], and the development of high salt concentration electrolyte (HCE)[150] or ionic liquid electrolyte[151]. However, as we discussed in Figure 4.1a, high oxidative stability is not the only criteria in selecting high voltage electrolytes. Other important properties are also required in designing high voltage electrolytes, such as good reduction stability and graphite compatibility, good thermal stability, cost effectiveness, high ionic conductivity, and low viscosity. A good high-voltage electrolyte needs to have balanced performance in the electrolyte property metrics.

Based on our work in Chapter 4, the following research directions are proposed. To start with, fluorinated carbonate solvents can be used in enabling batteries with high-voltage window and wide-temperature window. Fluorinated molecules possess C-F bonds that can significantly affect the HOMO and LUMO level of the solvents and alter the interfacial chemistry for LIBs.[217] Our group recently screened the deprotonation energy of different solvents on different LNMO facets (Table 5.1), and the results clearly show that FEC exhibits the highest energy barrier for both (100) and (111) facet in all the screened solvents. A FEC/FEMC electrolyte was prepared with a formula of 1M $LiPF_6$ in FEC/FEMC = 3:7 wt% and was compared with Gen2 electrolyte (1M $LiPF_6$ in EC/EMC = 3:7 wt%) in 3 mAh cm^{-2} level LNMO/graphite coin cells. While the cells show similar initial discharge capacities, FEC/FEMC electrolyte gives the most promising performance with 87.7% initial Coulombic efficiency and 73.2% capacity retention after 500 cycles (Figure 5.1a). At elevated temperature (55°C), the FEC/FEMC cells also show about 68%

retention after 100 cycles in C/3 cycling while Gen2 cells show a rapid decay after around 50 cycles (Figure 5.1b). This electrolyte can also be tested in LRLO or NMC materials and is expected to promote the cycling stability in these layered oxides as well. In addition, fluorinated solvents may be combined with LiBOB or other types of borate additives to further increase the cycling performance for high volage cathode materials.

Table 5.1 NEB reaction energy barriers for the electrolyte/cathode decomposition reactions.

$Ni_{0.5}Mn_{1.5}O_4$ (100) Fd3m	**EC**	**FEC**
Reaction Barrier (eV)	0.45	0.77
Reaction Energy (eV)	-1.53	-1.30
$Ni_{0.5}Mn_{1.5}O_4$ (111) Fd3m	**EC**	**FEC**
Reaction Barrier (eV)	0.54	0.90
Reaction Energy (eV)	-0.81	-0.72

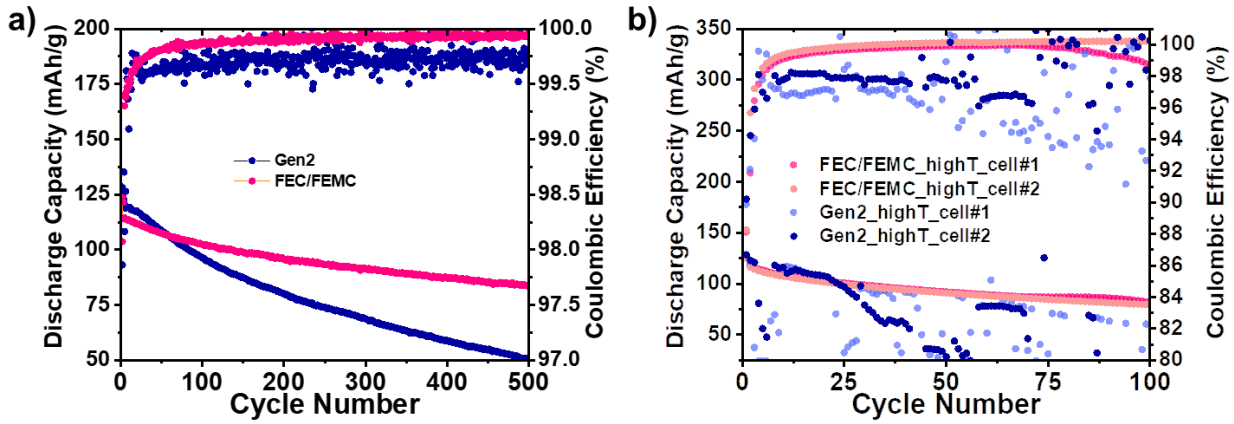

Figure 5.1 Cycling retention and Coulombic efficiency of LNMO/graphite cells with Gen2 and FEC/FEMC electrolyte under a) room temperature and b) 55°. All the cells are 3 mAh cm^{-2} loading cells tested with Al-clad CR2032 cases and Dreamweaver separator under 3.3-4.85V with C/3 cycling (1C=147 mA g^{-1}).

The second proposal in designing high voltage electrolyte is to explore localized high concentration electrolytes (LHCE). Previous studies indicate that the increase of salt concentration may increase the oxidative stability of the electrolyte, and high concentration electrolytes (HCE) has been proved as an effective strategy in stabilizing high voltage cells.[218,219] For example, with 5.9 M $LiBF_4$ in PC/FEC = 7:3, a capacity retention of 70% after 700 cycles can be achieved in a 4.8 V Li_2CoPO_4F/graphite cell.[220] However, HCE electrolytes usually suffer from high cost and poor electrode wettability which limits its application in thick electrodes. LHCE are thus employed to reduce the electrolyte viscosity by diluting the HCE electrolyte with an inert diluent.[217] LHCE can significantly lower the total Li salt concentration and improve the wettability with the electrodes and separators while preserving the benefits of HCE. This method has been recently applied to LRLO materials by Zhang *et al.*, where an LHCE electrolyte 1.4 M LiFSI in DMC/EC/TTE = 2:0.2:3 leads to 91.7% retention in 1.8 mAh cm^{-2} level $Li_{1.2}Ni_{0.15}Co_{0.1}Mn_{0.55}O_2$/graphite full cells cycled between 2.2 – 4.7 V.[221] Uniform CEI and SEI was also captured in this full cell after cycling. This electrolyte and its extensions may be explored with our LRLO or LNMO materials at higher loading. Also, a detailed mechanism study on how LHCE type electrolyte enhance the cell stability is still needed. For example, the chemical composition of CEI and SEI species as well as the electrolyte decomposition pathway on cathode and anode needs to be analysed. In addition, it is reported in literature that the increase of TTE diluent concentration may decrease the electrolyte ionic conductivity in LHCE.[222] Thus, the salt concentration and the ratio between carbonate solvent and diluent may also be further optimized.

References

(1) Sternberg, R. Hydropower's Future, the Environment, and Global Electricity Systems. *Renewable and Sustainable Energy Reviews* **2010**, *14* (2), 713–723. https://doi.org/10.1016/j.rser.2009.08.016.

(2) Santamouris, M.; Cartalis, C.; Synnefa, A.; Kolokotsa, D. On the Impact of Urban Heat Island and Global Warming on the Power Demand and Electricity Consumption of Buildings—A Review. *Energy and Buildings* **2015**, *98*, 119–124. https://doi.org/10.1016/j.enbuild.2014.09.052.

(3) Jacobson, M. Z.; Delucchi, M. A.; Bauer, Z. A. F.; Goodman, S. C.; Chapman, W. E.; Cameron, M. A.; Bozonnat, C.; Chobadi, L.; Clonts, H. A.; Enevoldsen, P.; Erwin, J. R.; Fobi, S. N.; Goldstrom, O. K.; Hennessy, E. M.; Liu, J.; Lo, J.; Meyer, C. B.; Morris, S. B.; Moy, K. R.; O'Neill, P. L.; Petkov, I.; Redfern, S.; Schucker, R.; Sontag, M. A.; Wang, J.; Weiner, E.; Yachanin, A. S. 100% Clean and Renewable Wind, Water, and Sunlight All-Sector Energy Roadmaps for 139 Countries of the World. *Joule* **2017**, *1* (1), 108–121. https://doi.org/10.1016/j.joule.2017.07.005.

(4) Moriarty, P.; Honnery, D. What Is the Global Potential for Renewable Energy? *Renewable and Sustainable Energy Reviews* **2012**, *16* (1), 244–252. https://doi.org/10.1016/j.rser.2011.07.151.

(5) Evans, A.; Strezov, V.; Evans, T. J. Assessment of Utility Energy Storage Options for Increased Renewable Energy Penetration. *Renewable and Sustainable Energy Reviews* **2012**, *16* (6), 4141–4147. https://doi.org/10.1016/j.rser.2012.03.048.

(6) Nishi, Y. Lithium Ion Secondary Batteries; Past 10 Years and the Future. *Journal of Power Sources* **2001**, *100* (1–2), 101–106. https://doi.org/10.1016/S0378-7753(01)00887-4.

(7) Madian, M.; Eychmüller, A.; Giebeler, L. Current Advances in TiO2-Based Nanostructure Electrodes for High Performance Lithium Ion Batteries. *Batteries* **2018**, *4* (1), 7. https://doi.org/10.3390/batteries4010007.

(8) Birkl, C. R.; Roberts, M. R.; McTurk, E.; Bruce, P. G.; Howey, D. A. Degradation Diagnostics for Lithium Ion Cells. *Journal of Power Sources* **2017**, *341*, 373–386. https://doi.org/10.1016/j.jpowsour.2016.12.011.

(9) Choi, J. U.; Voronina, N.; Sun, Y.; Myung, S. Recent Progress and Perspective of Advanced High-Energy Co-Less Ni-Rich Cathodes for Li-Ion Batteries: Yesterday, Today, and Tomorrow. *Advanced Energy Materials* **2020**, *10* (42), 2002027. https://doi.org/10.1002/aenm.202002027.

(10) Chen, Z.; Zhang, W.; Yang, Z. A Review on Cathode Materials for Advanced Lithium Ion Batteries: Microstructure Designs and Performance Regulations. *Nanotechnology* **2020**, *31* (1), 012001. https://doi.org/10.1088/1361-6528/ab4447.

(11) Whittingham, M. S. Electrical Energy Storage and Intercalation Chemistry. *Science (1979)* **1976**, *192* (4244), 1126–1127. https://doi.org/10.1126/science.192.4244.1126.

(12) Mizushima, K.; Jones, P. C.; Wiseman, P. J.; Goodenough, J. B. LixCoO2 (0<x<1): A New Cathode Material for Batteries of High Energy Density. *Materials Research Bulletin* **1980**, *15* (6), 783–789. https://doi.org/10.1016/0025-5408(80)90012-4.

(13) Yang, L.; Yang, K.; Zheng, J.; Xu, K.; Amine, K.; Pan, F. Harnessing the Surface Structure to Enable High-Performance Cathode Materials for Lithium-Ion Batteries. *Chemical Society Reviews* **2020**, *49* (14), 4667–4680. https://doi.org/10.1039/D0CS00137F.

(14) Li, W.; Wang, H.; Zhang, Y.; Ouyang, M. Flammability Characteristics of the Battery Vent Gas: A Case of NCA and LFP Lithium-Ion Batteries during External Heating Abuse. *Journal of Energy Storage* **2019**, *24*, 100775. https://doi.org/10.1016/J.EST.2019.100775.

(15) Logan, E. R.; Hebecker, H.; Eldesoky, A.; Luscombe, A.; Johnson, M. B.; Dahn, J. R. Performance and Degradation of LiFePO4/Graphite Cells: The Impact of Water Contamination and an Evaluation of Common Electrolyte Additives. *Journal of The Electrochemical Society* **2020**, *167* (13), 130543. https://doi.org/10.1149/1945-7111/abbbbe.

(16) Robert, R.; Villevieille, C.; Novák, P. Enhancement of the High Potential Specific Charge in Layered Electrode Materials for Lithium-Ion Batteries. *Journal of Materials Chemistry A* **2014**, *2* (23), 8589. https://doi.org/10.1039/c3ta12643a.

(17) Sharifi-Asl, S.; Lu, J.; Amine, K.; Shahbazian-Yassar, R. Oxygen Release Degradation in Li-Ion Battery Cathode Materials: Mechanisms and Mitigating Approaches. *Advanced Energy Materials* **2019**, *9* (22), 1900551. https://doi.org/10.1002/aenm.201900551.

(18) Pieczonka, N. P. W.; Liu, Z.; Lu, P.; Olson, K. L.; Moote, J.; Powell, B. R.; Kim, J.-H. Understanding Transition-Metal Dissolution Behavior in LiNi0.5Mn1.5O4 High-Voltage Spinel for Lithium Ion Batteries. *The Journal of Physical Chemistry C* **2013**, *117* (31), 15947–15957. https://doi.org/10.1021/jp405158m.

(19) Li, W.; Cho, Y.-G.; Yao, W.; Li, Y.; Cronk, A.; Shimizu, R.; Schroeder, M. A.; Fu, Y.; Zou, F.; Battaglia, V.; Manthiram, A.; Zhang, M.; Meng, Y. S. Enabling High Areal Capacity for Co-Free High Voltage Spinel Materials in next-Generation Li-Ion Batteries. *Journal of Power Sources* **2020**, *473*, 228579. https://doi.org/10.1016/j.jpowsour.2020.228579.

(20) Yabuuchi, N.; Takeuchi, M.; Nakayama, M.; Shiiba, H.; Ogawa, M.; Nakayama, K.; Ohta, T.; Endo, D.; Ozaki, T.; Inamasu, T.; Sato, K.; Komaba, S. High-Capacity Electrode Materials for Rechargeable Lithium Batteries: Li_3NbO_4 -Based System with Cation-Disordered Rocksalt Structure. *Proceedings of the National Academy of Sciences* **2015**, *112* (25), 7650–7655. https://doi.org/10.1073/pnas.1504901112.

(21) Qiu, B.; Zhang, M.; Xia, Y.; Liu, Z.; Meng, Y. S. Understanding and Controlling Anionic Electrochemical Activity in High-Capacity Oxides for Next Generation Li-Ion Batteries. *Chemistry of Materials* **2017**, *29* (3), 908–915. https://doi.org/10.1021/acs.chemmater.6b04815.

(22) Hong, J.; Lim, H. D.; Lee, M.; Kim, S. W.; Kim, H.; Oh, S. T.; Chung, G. C.; Kang, K. Critical Role of Oxygen Evolved from Layered Li-Excess Metal Oxides in Lithium Rechargeable Batteries. *Chemistry of Materials* **2012**, *24* (14), 2692–2697. https://doi.org/10.1021/cm3005634.

(23) Lu, Z.; Beaulieu, L. Y.; Donaberger, R. A.; Thomas, C. L.; Dahn, J. R. Synthesis, Structure, and Electrochemical Behavior of Li[Ni[Sub x]Li[Sub 1/3−2x/3]Mn[Sub 2/3−x/3]]O[Sub 2]. *Journal of The Electrochemical Society* **2002**, *149* (6), A778. https://doi.org/10.1149/1.1471541.

(24) Sathiya, M.; Leriche, J.-B.; Salager, E.; Gourier, D.; Tarascon, J.-M.; Vezin, H. Electron Paramagnetic Resonance Imaging for Real-Time Monitoring of Li-Ion Batteries. *Nature Communications* **2015**, *6*, 6276. https://doi.org/10.1038/ncomms7276.

(25) McCalla, E.; Abakumov, A. M.; Saubanere, M.; Foix, D.; Berg, E. J.; Rousse, G.; Doublet, M.-L.; Gonbeau, D.; Novak, P.; Van Tendeloo, G.; Dominko, R.; Tarascon, J.-M. Visualization of O-O Peroxo-like Dimers in High-Capacity Layered Oxides for Li-Ion Batteries. *Science (1979)* **2015**, *350* (6267), 1516–1522.

(26) Luo, K.; Roberts, M. R.; Hao, R.; Guerrini, N.; Pickup, D. M.; Liu, Y. S.; Edström, K.; Guo, J.; Chadwick, A. V.; Duda, L. C.; Bruce, P. G. Charge-Compensation in 3d-Transition-Metal-Oxide Intercalation Cathodes through the Generation of Localized Electron Holes on Oxygen. *Nature Chemistry* **2016**, *8* (7), 684–691. https://doi.org/10.1038/nchem.2471.

(27) Zhao, E.; Zhang, M.; Wang, X.; Hu, E.; Liu, J.; Yu, X.; Olguin, M.; Wynn, T. A.; Meng, Y. S.; Page, K.; Wang, F.; Li, H.; Yang, X. Q.; Huang, X.; Chen, L. Local Structure Adaptability through Multi Cations for Oxygen Redox Accommodation in Li-Rich Layered Oxides. *Energy Storage Materials* **2020**, *24*, 384–393. https://doi.org/10.1016/j.ensm.2019.07.032.

(28) House, R. A.; Maitra, U.; Pérez-Osorio, M. A.; Lozano, J. G.; Jin, L.; Somerville, J. W.; Duda, L. C.; Nag, A.; Walters, A.; Zhou, K. J.; Roberts, M. R.; Bruce, P. G. Superstructure Control of First-Cycle Voltage Hysteresis in Oxygen-Redox Cathodes. *Nature* **2020**, *577* (7791), 502–508. https://doi.org/10.1038/s41586-019-1854-3.

(29) Fan, Y.; Zhang, W.; Zhao, Y.; Guo, Z.; Cai, Q. Fundamental Understanding and Practical Challenges of Lithium-Rich Oxide Cathode Materials: Layered and Disordered-Rocksalt Structure. *Energy Storage Materials* **2021**, *40*, 51–71. https://doi.org/10.1016/J.ENSM.2021.05.005.

(30) Clément, R. J.; Lun, Z.; Ceder, G. Cation-Disordered Rocksalt Transition Metal Oxides and Oxyfluorides for High Energy Lithium-Ion Cathodes. *Energy & Environmental Science* **2020**, *13* (2), 345–373. https://doi.org/10.1039/C9EE02803J.

(31) Vetter, J.; Novák, P.; Wagner, M. R.; Veit, C.; Möller, K. C.; Besenhard, J. O.; Winter, M.; Wohlfahrt-Mehrens, M.; Vogler, C.; Hammouche, A. Ageing Mechanisms in Lithium-Ion Batteries. *Journal of Power Sources* **2005**, *147* (1–2), 269–281. https://doi.org/10.1016/J.JPOWSOUR.2005.01.006.

(32) Sharifi-Asl, S.; Lu, J.; Amine, K.; Shahbazian-Yassar, R. Oxygen Release Degradation in Li-Ion Battery Cathode Materials: Mechanisms and Mitigating Approaches. *Advanced Energy Materials* **2019**, *9* (22), 1900551. https://doi.org/10.1002/aenm.201900551.

(33) Jung, R.; Metzger, M.; Maglia, F.; Stinner, C.; Gasteiger, H. A. Oxygen Release and Its Effect on the Cycling Stability of LiNi x Mn y Co z O 2 (NMC) Cathode Materials for Li-Ion Batteries . *Journal of The Electrochemical Society* **2017**, *164* (7), A1361–A1377. https://doi.org/10.1149/2.0021707jes.

(34) Singer, A.; Zhang, M.; Hy, S.; Cela, D.; Fang, C.; Wynn, T. A.; Qiu, B.; Xia, Y.; Liu, Z.; Ulvestad, A.; Hua, N.; Wingert, J.; Liu, H.; Sprung, M.; Zozulya, A. v.; Maxey, E.; Harder, R.; Meng, Y. S.; Shpyrko, O. G. Nucleation of Dislocations and Their Dynamics in Layered Oxide Cathode Materials during Battery Charging. *Nature Energy* **2018**, *3* (8), 641–647. https://doi.org/10.1038/s41560-018-0184-2.

(35) Yan, P.; Zheng, J.; Gu, M.; Xiao, J.; Zhang, J.-G.; Wang, C.-M. Intragranular Cracking as a Critical Barrier for High-Voltage Usage of Layer-Structured Cathode for Lithium-Ion Batteries. *Nature Communications* **2017**, *8* (1), 14101. https://doi.org/10.1038/ncomms14101.

(36) Wei, W.; Ding, Z.; Chen, C.; Yang, C.; Han, B.; Xiao, L.; Liang, C.; Gao, P.; Cho, K. Surface-Dependent Stress-Corrosion Cracking in Ni-Rich Layered Oxide Cathodes. *Acta Materialia* **2021**, *212*, 116914. https://doi.org/10.1016/j.actamat.2021.116914.

(37) Zhan, C.; Wu, T.; Lu, J.; Amine, K. Dissolution, Migration, and Deposition of Transition Metal Ions in Li-Ion Batteries Exemplified by Mn-Based Cathodes – a Critical Review. *Energy & Environmental Science* **2018**, *11* (2), 243–257. https://doi.org/10.1039/C7EE03122J.

(38) Li, H.; Liu, A.; Zhang, N.; Wang, Y.; Yin, S.; Wu, H.; Dahn, J. R. An Unavoidable Challenge for Ni-Rich Positive Electrode Materials for Lithium-Ion Batteries. *Chemistry of Materials* **2019**, *31* (18), 7574–7583. https://doi.org/10.1021/acs.chemmater.9b02372.

(39) Zhao, W.; Zou, L.; Jia, H.; Zheng, J.; Wang, D.; Song, J.; Hong, C.; Liu, R.; Xu, W.; Yang, Y.; Xiao, J.; Wang, C.; Zhang, J.-G. Optimized Al Doping Improves Both Interphase Stability and Bulk Structural Integrity of Ni-Rich NMC Cathode Materials. *ACS Applied Energy Materials* **2020**, *3* (4), 3369–3377. https://doi.org/10.1021/acsaem.9b02372.

(40) Hu, J.; Li, L.; Bi, Y.; Tao, J.; Lochala, J.; Liu, D.; Wu, B.; Cao, X.; Chae, S.; Wang, C.; Xiao, J. Locking Oxygen in Lattice: A Quantifiable Comparison of Gas Generation in Polycrystalline and Single Crystal Ni-Rich Cathodes. *Energy Storage Materials* **2022**, *47*, 195–202. https://doi.org/10.1016/J.ENSM.2022.02.025.

(41) Qiu, B.; Zhang, M.; Wu, L.; Wang, J.; Xia, Y.; Qian, D.; Liu, H.; Hy, S.; Chen, Y.; An, K.; Zhu, Y.; Liu, Z.; Meng, Y. S. Gas–Solid Interfacial Modification of Oxygen Activity in Layered Oxide Cathodes for Lithium-Ion Batteries. *Nature Communications* **2016**, *7*, 12108. https://doi.org/10.1038/ncomms12108.

(42) Grenier, A.; Kamm, G. E.; Li, Y.; Chung, H.; Meng, Y. S.; Chapman, K. W. Nanostructure Transformation as a Signature of Oxygen Redox in Li-Rich 3d and 4d Cathodes. *J Am Chem Soc* **2021**, *143* (15), 5763–5770. https://doi.org/10.1021/jacs.1c00497.

(43) Seo, J. H.; Park, J.; Plett, G.; Sastry, A. M. Gas-Evolution Induced Volume Fraction Changes and Their Effect on the Performance Degradation of Li-Ion Batteries. *Electrochemical and Solid-State Letters* **2010**, *13* (9), A135. https://doi.org/10.1149/1.3458649.

(44) Vogt, L. O.; el Kazzi, M.; Jämstorp Berg, E.; Pérez Villar, S.; Novák, P.; Villevieille, C. Understanding the Interaction of the Carbonates and Binder in Na-Ion Batteries: A Combined Bulk and Surface Study. *Chemistry of Materials* **2015**, *27* (4), 1210–1216. https://doi.org/10.1021/cm5039649.

(45) Ma, T.; Xu, G.-L.; Li, Y.; Wang, L.; He, X.; Zheng, J.; Liu, J.; Engelhard, M. H.; Zapol, P.; Curtiss, L. A.; Jorne, J.; Amine, K.; Chen, Z. Revisiting the Corrosion of the Aluminum Current Collector in Lithium-Ion Batteries. *The Journal of Physical Chemistry Letters* **2017**, *8* (5), 1072–1077. https://doi.org/10.1021/acs.jpclett.6b02933.

(46) Li, X.; Deng, S.; Banis, M. N.; Doyle-Davis, K.; Zhang, D.; Zhang, T.; Yang, J.; Divigalpitiya, R.; Brandys, F.; Li, R.; Sun, X. Suppressing Corrosion of Aluminum Foils via Highly Conductive Graphene-like Carbon Coating in High-Performance Lithium-Based Batteries. *ACS Applied Materials & Interfaces* **2019**, *11* (36), 32826–32832. https://doi.org/10.1021/acsami.9b06442.

(47) Kobayashi, G.; Irii, Y.; Matsumoto, F.; Ito, A.; Ohsawa, Y.; Yamamoto, S.; Cui, Y.; Son, J.-Y.; Sato, Y. Improving Cycling Performance of Li-Rich Layered Cathode Materials through Combination of Al2O3-Based Surface Modification and Stepwise Precycling. *Journal of Power Sources* **2016**, *303*, 250–256. https://doi.org/10.1016/j.jpowsour.2015.11.014.

(48) Knight, J. C.; Nandakumar, P.; Kan, W. H.; Manthiram, A. Effect of Ru Substitution on the First Charge–Discharge Cycle of Lithium-Rich Layered Oxides. *Journal of Materials Chemistry A* **2015**, *3* (5), 2006–2011. https://doi.org/10.1039/C4TA05178E.

(49) Wynn, T. A.; Fang, C.; Zhang, M.; Liu, H.; Davies, D. M.; Wang, X.; Lau, D.; Lee, J. Z.; Huang, B. Y.; Fung, K. Z.; Ni, C. T.; Meng, Y. S. Mitigating Oxygen Release in Anionic-

Redox-Active Cathode Materials by Cationic Substitution through Rational Design. *Journal of Materials Chemistry A* **2018**, *6* (47), 24651–24659. https://doi.org/10.1039/c8ta06296j.

(50) Lengyel, M.; Shen, K. Y.; Lanigan, D. M.; Martin, J. M.; Zhang, X.; Axelbaum, R. L. Trace Level Doping of Lithium-Rich Cathode Materials. *Journal of Materials Chemistry A* **2016**, *4* (9), 3538–3545. https://doi.org/10.1039/c5ta07764h.

(51) Nayak, P. K.; Grinblat, J.; Levi, M.; Aurbach, D. Understanding the Effect of Lithium Bis(Oxalato) Borate (LiBOB) on the Structural and Electrochemical Aging of Li and Mn Rich High Capacity Li1.2Ni0.16Mn0.56Co0.08O2 Cathodes. *J Electrochem Soc* **2015**, *162* (4), A596–A602. https://doi.org/10.1149/2.0251504jes.

(52) Li, Y.; Li, W.; Shimizu, R.; Cheng, D.; Nguyen, H.; Paulsen, J.; Kumakura, S.; Zhang, M.; Meng, Y. S. Elucidating the Effect of Borate Additive in High-Voltage Electrolyte for Li-Rich Layered Oxide Materials. *Advanced Energy Materials* **2022**, *12* (11), 2103033. https://doi.org/10.1002/aenm.202103033.

(53) Alvarado, J.; Schroeder, M. A.; Zhang, M.; Borodin, O.; Gobrogge, E.; Olguin, M.; Ding, M. S.; Gobet, M.; Greenbaum, S.; Meng, Y. S.; Xu, K. A Carbonate-Free, Sulfone-Based Electrolyte for High-Voltage Li-Ion Batteries. *Materials Today* **2018**, *21* (4), 341–353. https://doi.org/10.1016/j.mattod.2018.02.005.

(54) Neumann, D. A. Neutron Scattering and Hydrogenous Materials. *Materials Today* **2006**, *9* (1–2), 34–41. https://doi.org/10.1016/S1369-7021(05)71336-5.

(55) Zhao, E.; Zhang, M.; Wang, X.; Hu, E.; Liu, J.; Yu, X.; Olguin, M.; Wynn, T. A.; Meng, Y. S.; Page, K.; Wang, F.; Li, H.; Yang, X.-Q.; Huang, X.; Chen, L. Local Structure Adaptability through Multi Cations for Oxygen Redox Accommodation in Li-Rich Layered Oxides. *Energy Storage Materials* **2020**, *24*, 384–393. https://doi.org/10.1016/j.ensm.2019.07.032.

(56) Wang, X.; Tan, S.; Yang, X.-Q.; Hu, E. Pair Distribution Function Analysis: Fundamentals and Application to Battery Materials. *Chinese Physics B* **2020**, *29* (2), 028802. https://doi.org/10.1088/1674-1056/ab6656.

(57) Zernike, F.; Prins, J. A. Die Beugung von Röntgenstrahlen in Flüssigkeiten Als Effekt Der Molekülanordnung. *Zeitschrift für Physik A Hadrons and nuclei* **1927**, *41* (2–3), 184–194. https://doi.org/10.1007/BF01391926.

(58) Lin, R.; Hu, E.; Liu, M.; Wang, Y.; Cheng, H.; Wu, J.; Zheng, J.-C.; Wu, Q.; Bak, S.; Tong, X.; Zhang, R.; Yang, W.; Persson, K. A.; Yu, X.; Yang, X.-Q.; Xin, H. L. Anomalous Metal Segregation in Lithium-Rich Material Provides Design Rules for Stable Cathode in Lithium-Ion Battery. *Nature Communications* **2019**, *10* (1), 1650. https://doi.org/10.1038/s41467-019-09248-0.

(59) Allan, P. K.; Griffin, J. M.; Darwiche, A.; Borkiewicz, O. J.; Wiaderek, K. M.; Chapman, K. W.; Morris, A. J.; Chupas, P. J.; Monconduit, L.; Grey, C. P. Tracking Sodium-

Antimonide Phase Transformations in Sodium-Ion Anodes: Insights from Operando Pair Distribution Function Analysis and Solid-State NMR Spectroscopy. *J Am Chem Soc* **2016**, *138* (7), 2352–2365. https://doi.org/10.1021/jacs.5b13273.

(60) Liu, D.; Shadike, Z.; Lin, R.; Qian, K.; Li, H.; Li, K.; Wang, S.; Yu, Q.; Liu, M.; Ganapathy, S.; Qin, X.; Yang, Q.; Wagemaker, M.; Kang, F.; Yang, X.; Li, B. Review of Recent Development of In Situ/Operando Characterization Techniques for Lithium Battery Research. *Advanced Materials* **2019**, *31* (28), 1806620. https://doi.org/10.1002/adma.201806620.

(61) Borkiewicz, O. J.; Shyam, B.; Wiaderek, K. M.; Kurtz, C.; Chupas, P. J.; Chapman, K. W. The AMPIX Electrochemical Cell: A Versatile Apparatus for *in Situ* X-Ray Scattering and Spectroscopic Measurements. *Journal of Applied Crystallography* **2012**, *45* (6), 1261–1269. https://doi.org/10.1107/S0021889812042720.

(62) Brant, W. R.; Li, D.; Gu, Q.; Schmid, S. Comparative Analysis of Ex-Situ and Operando X-Ray Diffraction Experiments for Lithium Insertion Materials. *Journal of Power Sources* **2016**, *302*, 126–134. https://doi.org/10.1016/j.jpowsour.2015.10.015.

(63) Rosciano, F.; Holzapfel, M.; Kaiser, H.; Scheifele, W.; Ruch, P.; Hahn, M.; Kötz, R.; Novák, P. A Multi-Sample Automatic System for *in Situ* Electrochemical X-Ray Diffraction Synchrotron Measurements. *Journal of Synchrotron Radiation* **2007**, *14* (6), 487–491. https://doi.org/10.1107/S0909049507039209.

(64) Liu, Q.; He, H.; Li, Z.-F.; Liu, Y.; Ren, Y.; Lu, W.; Lu, J.; Stach, E. A.; Xie, J. Rate-Dependent, Li-Ion Insertion/Deinsertion Behavior of $LiFePO_4$ Cathodes in Commercial 18650 $LiFePO_4$ Cells. *ACS Applied Materials & Interfaces* **2014**, *6* (5), 3282–3289. https://doi.org/10.1021/am405150c.

(65) Leriche, J. B.; Hamelet, S.; Shu, J.; Morcrette, M.; Masquelier, C.; Ouvrard, G.; Zerrouki, M.; Soudan, P.; Belin, S.; Elkaïm, E.; Baudelet, F. An Electrochemical Cell for Operando Study of Lithium Batteries Using Synchrotron Radiation. *Journal of The Electrochemical Society* **2010**, *157* (5), A606. https://doi.org/10.1149/1.3355977.

(66) Liu, H.; Allan, P. K.; Borkiewicz, O. J.; Kurtz, C.; Grey, C. P.; Chapman, K. W.; Chupas, P. J. A Radially Accessible Tubular *in Situ* X-Ray Cell for Spatially Resolved *Operando* Scattering and Spectroscopic Studies of Electrochemical Energy Storage Devices. *Journal of Applied Crystallography* **2016**, *49* (5), 1665–1673. https://doi.org/10.1107/S1600576716012632.

(67) Ruppender, H. J.; Grunze, M.; Kong, C. W.; Wilmers, M. In Situ X-Ray Photoelectron Spectroscopy of Surfaces at Pressures up to 1 Mbar. *Surface and Interface Analysis* **1990**, *15* (4), 245–253. https://doi.org/10.1002/sia.740150403.

(68) Gupta, V.; Ganegoda, H.; Engelhard, M. H.; Terry, J.; Linford, M. R. Assigning Oxidation States to Organic Compounds via Predictions from X-Ray Photoelectron Spectroscopy: A Discussion of Approaches and Recommended Improvements. *Journal of Chemical Education* **2014**, *91* (2), 232–238. https://doi.org/10.1021/ed400401c.

(69) Liu, Y.; Harlow, J.; Dahn, J. Microstructural Observations of “Single Crystal” Positive Electrode Materials Before and After Long Term Cycling by Cross-Section Scanning Electron Microscopy. *Journal of The Electrochemical Society* **2020**, *167* (2), 020512. https://doi.org/10.1149/1945-7111/ab6288.

(70) Harlow, J. E.; Ma, X.; Li, J.; Logan, E.; Liu, Y.; Zhang, N.; Ma, L.; Glazier, S. L.; Cormier, M. M. E.; Genovese, M.; Buteau, S.; Cameron, A.; Stark, J. E.; Dahn, J. R. A Wide Range of Testing Results on an Excellent Lithium-Ion Cell Chemistry to Be Used as Benchmarks for New Battery Technologies. *Journal of The Electrochemical Society* **2019**, *166* (13), A3031–A3044. https://doi.org/10.1149/2.0981913jes.

(71) Lin, F.; Markus, I. M.; Nordlund, D.; Weng, T. C.; Asta, M. D.; Xin, H. L.; Doeff, M. M. Surface Reconstruction and Chemical Evolution of Stoichiometric Layered Cathode Materials for Lithium-Ion Batteries. *Nat Commun* **2014**, *5*, 3529. https://doi.org/10.1038/ncomms4529.

(72) Dixit, M.; Markovsky, B.; Schipper, F.; Aurbach, D.; Major, D. T. Origin of Structural Degradation during Cycling and Low Thermal Stability of Ni-Rich Layered Transition Metal-Based Electrode Materials. *Journal of Physical Chemistry C* **2017**, *121* (41), 22628–22636. https://doi.org/10.1021/acs.jpcc.7b06122.

(73) Asenbauer, J.; Eisenmann, T.; Kuenzel, M.; Kazzazi, A.; Chen, Z.; Bresser, D. The Success Story of Graphite as a Lithium-Ion Anode Material – Fundamentals, Remaining Challenges, and Recent Developments Including Silicon (Oxide) Composites. *Sustainable Energy & Fuels* **2020**, *4* (11), 5387–5416. https://doi.org/10.1039/D0SE00175A.

(74) de Biasi, L.; Schwarz, B.; Brezesinski, T.; Hartmann, P.; Janek, J.; Ehrenberg, H. Chemical, Structural, and Electronic Aspects of Formation and Degradation Behavior on Different Length Scales of Ni-Rich NCM and Li-Rich HE-NCM Cathode Materials in Li-Ion Batteries. *Advanced Materials* **2019**, *31* (26), 1900985. https://doi.org/10.1002/adma.201900985.

(75) Ryu, H. H.; Park, K. J.; Yoon, C. S.; Sun, Y. K. Capacity Fading of Ni-Rich Li[NixCoyMn1-x-y]O2 ($0.6 \leq x \leq 0.95$) Cathodes for High-Energy-Density Lithium-Ion Batteries: Bulk or Surface Degradation? *Chemistry of Materials* **2018**, *30* (3), 1155–1163. https://doi.org/10.1021/acs.chemmater.7b05269.

(76) Lee, E. J.; Chen, Z.; Noh, H. J.; Nam, S. C.; Kang, S.; Kim, D. H.; Amine, K.; Sun, Y. K. Development of Microstrain in Aged Lithium Transition Metal Oxides. *Nano Letters* **2014**, *14* (8), 4873–4880. https://doi.org/10.1021/nl5022859.

(77) Kim, J. H.; Park, K. J.; Kim, S. J.; Yoon, C. S.; Sun, Y. K. A Method of Increasing the Energy Density of Layered Ni-Rich Li[Ni 1-2: X Co x Mn x]O 2 Cathodes (x = 0.05, 0.1, 0.2). *Journal of Materials Chemistry A* **2019**, *7* (6), 2694–2701. https://doi.org/10.1039/c8ta10438g.

(78) Zhang, S. S. Problems and Their Origins of Ni-Rich Layered Oxide Cathode Materials. *Energy Storage Materials* **2020**, *24*, 247–254. https://doi.org/10.1016/j.ensm.2019.08.013.

(79) Han, M.; Liu, Z.; Shen, X.; Yang, L.; Shen, X.; Zhang, Q.; Liu, X.; Wang, J.; Lin, H.; Chen, C.; Pao, C.; Chen, J.; Kong, Q.; Yu, X.; Yu, R.; Gu, L.; Hu, Z.; Wang, X.; Wang, Z.; Chen, L. Stacking Faults Hinder Lithium Insertion in Li_2RuO_3. *Advanced Energy Materials* **2020**, *10* (48), 2002631. https://doi.org/10.1002/aenm.202002631.

(80) Li, S.; Yao, Z.; Zheng, J.; Fu, M.; Cen, J.; Hwang, S.; Jin, H.; Orlov, A.; Gu, L.; Wang, S.; Chen, Z.; Su, D. Direct Observation of Defect-Aided Structural Evolution in a Nickel-Rich Layered Cathode. *Angewandte Chemie* **2020**, *132* (49), 22276–22283. https://doi.org/10.1002/ange.202008144.

(81) van der Ven, A.; Aydinol, M. K.; Ceder, G.; Kresse, G.; Hafner, J. First-Principles Investigation of Phase Stability in LixCoO2. *Physical Review B* **1998**, *58* (6), 2975–2987. https://doi.org/10.1103/PhysRevB.58.2975.

(82) Wang, C.; Han, L.; Zhang, R.; Cheng, H.; Mu, L.; Kisslinger, K.; Zou, P.; Ren, Y.; Cao, P.; Lin, F.; Xin, H. L. Resolving Atomic-Scale Phase Transformation and Oxygen Loss Mechanism in Ultrahigh-Nickel Layered Cathodes for Cobalt-Free Lithium-Ion Batteries. *Matter* **2021**, *4* (6), 2013–2026. https://doi.org/10.1016/j.matt.2021.03.012.

(83) Huang, J. J.; Weinstock, D.; Hirsh, H.; Bouck, R.; Zhang, M.; Gorobtsov, O. Yu.; Okamura, M.; Harder, R.; Cha, W.; Ruff, J. P. C.; Meng, Y. S.; Singer, A. Disorder Dynamics in Battery Nanoparticles During Phase Transitions Revealed by Operando Single-Particle Diffraction. *Advanced Energy Materials* **2022**, *12* (12), 2103521. https://doi.org/10.1002/aenm.202103521.

(84) Ahmed, S.; Pokle, A.; Bianchini, M.; Schweidler, S.; Beyer, A.; Brezesinski, T.; Janek, J.; Volz, K. Understanding the Formation of Antiphase Boundaries in Layered Oxide Cathode Materials and Their Evolution upon Electrochemical Cycling. *Matter* **2021**, *4* (12), 3953–3966. https://doi.org/10.1016/j.matt.2021.10.001.

(85) Chung, H.; Grenier, A.; Huang, R.; Wang, X.; Lebens-Higgins, Z.; Doux, J. M.; Sallis, S.; Song, C.; Ercius, P.; Chapman, K.; Piper, L. F. J.; Cho, H. M.; Zhang, M.; Meng, Y. S. Comprehensive Study of a Versatile Polyol Synthesis Approach for Cathode Materials for Li-Ion Batteries. *Nano Research* **2019**, *12* (9), 2238–2249. https://doi.org/10.1007/s12274-019-2494-5.

(86) Faenza, N. V.; Bruce, L.; Lebens-Higgins, Z. W.; Plitz, I.; Pereira, N.; Piper, L. F. J.; Amatucci, G. G. Growth of Ambient Induced Surface Impurity Species on Layered Positive Electrode Materials and Impact on Electrochemical Performance. *J Electrochem Soc* **2017**, *164* (14), A3727–A3741. https://doi.org/10.1149/2.0921714jes.

(87) Liu, H.; Allan, P. K.; Borkiewicz, O. J.; Kurtz, C.; Grey, C. P.; Chapman, K. W.; Chupas, P. J. A Radially Accessible Tubular in Situ X-Ray Cell for Spatially Resolved Operando Scattering and Spectroscopic Studies of Electrochemical Energy Storage Devices. *Journal of Applied Crystallography* **2016**, *49* (5), 1665–1673. https://doi.org/10.1107/S1600576716012632.

(88) Toby, B. H.; von Dreele, R. B. GSAS-II: The Genesis of a Modern Open-Source All Purpose Crystallography Software Package. *Journal of Applied Crystallography* **2013**, *46.2*, 544–549. https://doi.org/10.1107/S0021889813003531.

(89) Lin, F.; Markus, I. M.; Nordlund, D.; Weng, T. C.; Asta, M. D.; Xin, H. L.; Doeff, M. M. Surface Reconstruction and Chemical Evolution of Stoichiometric Layered Cathode Materials for Lithium-Ion Batteries. *Nat Commun* **2014**, *5*, 3529. https://doi.org/10.1038/ncomms4529.

(90) Jiang, Y.; Yan, P.; Yu, M.; Li, J.; Jiao, H.; Zhou, B.; Sui, M. Atomistic Mechanism of Cracking Degradation at Twin Boundary of LiCoO2. *Nano Energy* **2020**, *78*, 105364. https://doi.org/10.1016/j.nanoen.2020.105364.

(91) Moriwake, H.; Kuwabara, A.; Fisher, C. A. J.; Huang, R.; Hitosugi, T.; Ikuhara, Y. H.; Oki, H.; Ikuhara, Y. First-Principles Calculations of Lithium-Ion Migration at a Coherent Grain Boundary in a Cathode Material, LiCoO2. *Advanced Materials* **2013**, *25* (4), 618–622. https://doi.org/10.1002/adma.201202805.

(92) Zheng, J.; Yan, P.; Zhang, J.; Engelhard, M. H.; Zhu, Z.; Polzin, B. J.; Trask, S.; Xiao, J.; Wang, C.; Zhang, J. Suppressed Oxygen Extraction and Degradation of LiNixMnyCozO2cathodes at High Charge Cut-off Voltages. *Nano Research* **2017**, *10* (12), 4221–4231. https://doi.org/10.1007/s12274-017-1761-6.

(93) Wulff, G. XXV. Zur Frage Der Geschwindigkeit Des Wachsthums Und Der Auflösung Der Krystallflächen. *Zeitschrift für Kristallographie - Crystalline Materials* **1901**, *34* (1), 449–530. https://doi.org/https://doi.org/10.1524/zkri.1901.34.1.449.

(94) Marks, L. D. Surface Structure and Energetics of Multiply Twinned Particles. *Philosophical Magazine A* **1984**, *49* (1), 81–93. https://doi.org/10.1080/01418618408233431.

(95) Howie, A.; Marks, L. D. Elastic Strains and the Energy Balance for Multiply Twinned Particles. *Philosophical Magazine A* **1984**, *49* (1), 95–109. https://doi.org/10.1080/01418618408233432.

(96) Kramer, D.; Ceder, G. Tailoring the Morphology of LiCoO2: A First Principles Study. *Chemistry of Materials* **2009**, *21* (16), 3799–3809. https://doi.org/10.1021/cm9008943.

(97) Howe, J. M. *Interfaces in Materials*, 1st ed.; Wiley-Interscience: New York, 1997.

(98) Chung, H.; Grenier, A.; Huang, R.; Wang, X.; Lebens-Higgins, Z.; Doux, J. M.; Sallis, S.; Song, C.; Ercius, P.; Chapman, K.; Piper, L. F. J.; Cho, H. M.; Zhang, M.; Meng, Y. S. Comprehensive Study of a Versatile Polyol Synthesis Approach for Cathode Materials for Li-Ion Batteries. *Nano Research* **2019**, *12* (9), 2238–2249. https://doi.org/10.1007/s12274-019-2494-5.

(99) Seo, D.-H.; Lee, J.; Urban, A.; Malik, R.; Kang, S.; Ceder, G. The Structural and Chemical Origin of the Oxygen Redox Activity in Layered and Cation-Disordered Li-

Excess Cathode Materials. *Nature Chemistry* **2016**, *8* (7), 692–697. https://doi.org/10.1038/nchem.2524.

(100) Zhang, F.; Lou, S.; Li, S.; Yu, Z.; Liu, Q.; Dai, A.; Cao, C.; Toney, M. F.; Ge, M.; Xiao, X.; Lee, W. K.; Yao, Y.; Deng, J.; Liu, T.; Tang, Y.; Yin, G.; Lu, J.; Su, D.; Wang, J. Surface Regulation Enables High Stability of Single-Crystal Lithium-Ion Cathodes at High Voltage. *Nature Communications* **2020**, *11* (1). https://doi.org/10.1038/s41467-020-16824-2.

(101) Li, W.; Asl, H. Y.; Xie, Q.; Manthiram, A. Collapse of LiNi1- x- YCoxMnyO2 Lattice at Deep Charge Irrespective of Nickel Content in Lithium-Ion Batteries. *J Am Chem Soc* **2019**, *141* (13), 5097–5101. https://doi.org/10.1021/jacs.8b13798.

(102) Chen, J.; Yang, H.; Li, T.; Liu, C.; Tong, H.; Chen, J.; Liu, Z.; Xia, L.; Chen, Z.; Duan, J.; Li, L. The Effects of Reversibility of H2-H3 Phase Transition on Ni-Rich Layered Oxide Cathode for High-Energy Lithium-Ion Batteries. *Frontiers in Chemistry* **2019**, *7* (July), 1–10. https://doi.org/10.3389/fchem.2019.00500.

(103) Xu, X.; Huo, H.; Jian, J.; Wang, L.; Zhu, H.; Xu, S.; He, X.; Yin, G.; Du, C.; Sun, X. Radially Oriented Single-Crystal Primary Nanosheets Enable Ultrahigh Rate and Cycling Properties of LiNi 0.8 Co 0.1 Mn 0.1 O 2 Cathode Material for Lithium-Ion Batteries. *Advanced Energy Materials* **2019**, *9* (15), 1–9. https://doi.org/10.1002/aenm.201803963.

(104) Hu, J.; Li, L.; Hu, E.; Chae, S.; Jia, H.; Liu, T.; Wu, B.; Bi, Y.; Amine, K.; Wang, C.; Zhang, J.; Tao, J.; Xiao, J. Mesoscale-Architecture-Based Crack Evolution Dictating Cycling Stability of Advanced Lithium Ion Batteries. *Nano Energy* **2021**, *79*, 105420. https://doi.org/10.1016/j.nanoen.2020.105420.

(105) Kim, J. H.; Kim, S. J.; Yuk, T.; Kim, J.; Yoon, C. S.; Sun, Y. K. Variation of Electronic Conductivity within Secondary Particles Revealing a Capacity-Fading Mechanism of Layered Ni-Rich Cathode. *ACS Energy Letters* **2018**, *3* (12), 3002–3007. https://doi.org/10.1021/acsenergylett.8b02043.

(106) Tsai, P. C.; Wen, B.; Wolfman, M.; Choe, M. J.; Pan, M. S.; Su, L.; Thornton, K.; Cabana, J.; Chiang, Y. M. Single-Particle Measurements of Electrochemical Kinetics in NMC and NCA Cathodes for Li-Ion Batteries. *Energy and Environmental Science* **2018**, *11* (4), 860–871. https://doi.org/10.1039/c8ee00001h.

(107) Woodford, W. H.; Carter, W. C.; Chiang, Y. M. Design Criteria for Electrochemical Shock Resistant Battery Electrodes. *Energy and Environmental Science* **2012**, *5* (7), 8014–8024. https://doi.org/10.1039/c2ee21874g.

(108) Kim, T.; Song, W.; Son, D. Y.; Ono, L. K.; Qi, Y. Lithium-Ion Batteries: Outlook on Present, Future, and Hybridized Technologies. *Journal of Materials Chemistry A* **2019**, *7* (7), 2942–2964. https://doi.org/10.1039/C8TA10513H.

(109) Lee, B.; Wu, Z.; Petrova, V.; Xing, X.; Lim, H.; Liu, H.; Liu, P. Analysis of Rate-Limiting Factors in Thick Electrodes for Electric Vehicle Applications. *Journal of The*

Electrochemical Society **2018**, *165* (3), A525–A533. https://doi.org/10.1149/2.0571803jes.

(110) Ye, J.; Li, Y. X.; Zhang, L.; Zhang, X. P.; Han, M.; He, P.; Zhou, H. S. Fabrication and Performance of High Energy Li-Ion Battery Based on the Spherical Li[Li0.2Ni0.16Co0.1Mn0.54]O2 Cathode and Si Anode. *ACS Applied Materials and Interfaces* **2016**, *8* (1), 208–214. https://doi.org/10.1021/acsami.5b08349.

(111) Goodenough, J. B.; Kim, Y. Challenges for Rechargeable Li Batteries. *Chemistry of Materials* **2010**, *22* (3), 587–603. https://doi.org/10.1021/cm901452z.

(112) Hy, S.; Liu, H.; Zhang, M.; Qian, D.; Hwang, B.-J.; Meng, Y. S. Performance and Design Considerations for Lithium Excess Layered Oxide Positive Electrode Materials for Lithium Ion Batteries. *Energy Environ. Sci.* **2016**, *9* (6), 1931–1954. https://doi.org/10.1039/C5EE03573B.

(113) Radin, M. D.; Hy, S.; Sina, M.; Fang, C.; Liu, H.; Vinckeviciute, J.; Zhang, M.; Whittingham, M. S.; Meng, Y. S.; Van der Ven, A. Narrowing the Gap between Theoretical and Practical Capacities in Li-Ion Layered Oxide Cathode Materials. *Advanced Energy Materials* **2017**, *1602888*, 1–33. https://doi.org/10.1002/aenm.201602888.

(114) Fell, C. R.; Qian, D.; Carroll, K. J.; Chi, M.; Jones, J. L.; Meng, Y. S. Correlation Between Oxygen Vacancy, Microstrain, and Cation Distribution in Lithium-Excess Layered Oxides During the First Electrochemical Cycle. *Chemistry of Materials* **2013**, *25* (9), 1621–1629. https://doi.org/10.1021/cm4000119.

(115) Croy, J. R.; Balasubramanian, M.; Gallagher, K. G.; Burrell, A. K. Review of the U.S. Department of Energy's "Deep Dive" Effort to Understand Voltage Fade in Li- and Mn-Rich Cathodes. *Accounts of Chemical Research* **2015**, *48* (11), 2813–2821. https://doi.org/10.1021/acs.accounts.5b00277.

(116) Jarvis, K. A.; Deng, Z.; Allard, L. F.; Manthiram, A.; Ferreira, P. J. Atomic Structure of a Lithium-Rich Layered Oxide Material for Lithium-Ion Batteries: Evidence of a Solid Solution. *Chemistry of Materials* **2011**, *23* (16), 3614–3621. https://doi.org/10.1021/cm200831c.

(117) Qian, D.; Xu, B.; Chi, M.; Meng, Y. S. Uncovering the Roles of Oxygen Vacancies in Cation Migration in Lithium Excess Layered Oxides. *Phys Chem Chem Phys* **2014**, *16* (28), 14665–14668. https://doi.org/10.1039/c4cp01799d.

(118) Xu, B.; Fell, C. R.; Chi, M.; Meng, Y. S. Identifying Surface Structural Changes in Layered Li-Excess Nickel Manganese Oxides in High Voltage Lithium Ion Batteries: A Joint Experimental and Theoretical Study. *Energy and Environmental Science* **2011**, *4* (6), 2223–2233. https://doi.org/10.1039/c1ee01131f.

(119) Fell, C. R.; Chi, M.; Meng, Y. S.; Jones, J. L. In Situ X-Ray Diffraction Study of the Lithium Excess Layered Oxide Compound Li[Li 0.2Ni 0.2Mn 0.6]O 2 during

Electrochemical Cycling. *Solid State Ionics* **2012**, *207*, 44–49. https://doi.org/10.1016/j.ssi.2011.11.018.

(120) Zhang, X.; Belharouak, I.; Li, L.; Lei, Y.; Elam, J. W.; Nie, A.; Chen, X.; Yassar, R. S.; Axelbaum, R. L. Structural and Electrochemical Study of Al2O3 and TiO2 Coated Li1.2Ni0.13Mn0.54Co 0.13O2 Cathode Material Using ALD. *Advanced Energy Materials* **2013**, *3* (10), 1299–1307. https://doi.org/10.1002/aenm.201300269.

(121) Wynn, T. A.; Fang, C.; Zhang, M.; Liu, H.; Davies, D. M.; Wang, X.; Lau, D.; Lee, J. Z.; Huang, B. Y.; Fung, K. Z.; Ni, C. T.; Meng, Y. S. Mitigating Oxygen Release in Anionic-Redox-Active Cathode Materials by Cationic Substitution through Rational Design. *Journal of Materials Chemistry A* **2018**, *6* (47), 24651–24659. https://doi.org/10.1039/c8ta06296j.

(122) Qiu, B.; Zhang, M.; Lee, S.-Y.; Liu, H.; Wynn, T. A.; Wu, L.; Zhu, Y.; Wen, W.; Brown, C. M.; Zhou, D.; Liu, Z.; Meng, Y. S. Metastability and Reversibility of Anionic Redox-Based Cathode for High-Energy Rechargeable Batteries. *Cell Reports Physical Science* **2020**, *1* (3), 100028. https://doi.org/10.1016/j.xcrp.2020.100028.

(123) Toby, B. H.; Von Dreele, R. B. GSAS-II: The Genesis of a Modern Open-Source All Purpose Crystallography Software Package. *Journal of Applied Crystallography* **2013**, *46.2*, 544–549. https://doi.org/10.1107/S0021889813003531.

(124) Farrow, C. L.; Juhas, P.; Liu, J. W.; Bryndin, D.; Boin, E. S.; Bloch, J.; Proffen, T.; Billinge, S. J. L. PDFfit2 and PDFgui: Computer Programs for Studying Nanostructure in Crystals. *Journal of Physics Condensed Matter* **2007**, *19.33*, 335219. https://doi.org/10.1088/0953-8984/19/33/335219.

(125) Newville, M. IFEFFIT: Interactive XAFS Analysis and FEFF Fitting. *Journal of Synchrotron Radiation* **2001**, *8*, 322–324. https://doi.org/10.1107/S0909049500016964.

(126) Ravel, B.; Newville, M. ATHENA, ARTEMIS, HEPHAESTUS: Data Analysis for X-Ray Absorption Spectroscopy Using IFEFFIT. In *Journal of Synchrotron Radiation*; 2005; Vol. 12, pp 537–541. https://doi.org/10.1107/S0909049505012719.

(127) Ankudinov, A.; Ravel, B. Real-Space Multiple-Scattering Calculation and Interpretation of x-Ray-Absorption near-Edge Structure. *Physical Review B - Condensed Matter and Materials Physics* **1998**, *58* (12), 7565–7576. https://doi.org/10.1103/PhysRevB.58.7565.

(128) Joubert, D. From Ultrasoft Pseudopotentials to the Projector Augmented-Wave Method. *Physical Review B - Condensed Matter and Materials Physics* **1999**, *59* (3), 1758–1775. https://doi.org/10.1103/PhysRevB.59.1758.

(129) Perdew, J. P.; Burke, K.; Ernzerhof, M. Generalized Gradient Approximation Made Simple. *Physical Review Letters* **1996**, *77* (18), 3865–3868. https://doi.org/10.1103/PhysRevLett.77.3865.

(130) Ko, M.; Oh, P.; Chae, S.; Cho, W.; Cho, J. Considering Critical Factors of Li-Rich Cathode and Si Anode Materials for Practical Li-Ion Cell Applications. *Small* **2015**, 11.33, 4058–4073. https://doi.org/10.1002/smll.201500474.

(131) Seo, D.-H.; Lee, J.; Urban, A.; Malik, R.; Kang, S.; Ceder, G. The Structural and Chemical Origin of the Oxygen Redox Activity in Layered and Cation-Disordered Li-Excess Cathode Materials. *Nature Chemistry* **2016**, *8* (7), 692–697. https://doi.org/10.1038/nchem.2524.

(132) Liu, H.; Chen, Y.; Hy, S.; An, K.; Venkatachalam, S.; Qian, D.; Zhang, M.; Meng, Y. S. Operando Lithium Dynamics in the Li-Rich Layered Oxide Cathode Material via Neutron Diffraction. *Advanced Energy Materials* **2016**, *6* (7), 1–7. https://doi.org/10.1002/aenm.201502143.

(133) Mohanty, D.; Kalnaus, S.; Meisner, R. A.; Rhodes, K. J.; Li, J.; Payzant, E. A.; Wood, D. L.; Daniel, C. Cathode during High Voltage Cycling Resolved by in Situ X-Ray Diffraction. *Journal of Power Sources* **2013**, *229*, 239–248. https://doi.org/10.1016/j.jpowsour.2012.11.144.

(134) Koga, H.; Croguennec, L.; Ménétrier, M.; Mannessiez, P.; Weill, F.; Delmas, C.; Belin, S. Operando X-Ray Absorption Study of the Redox Processes Involved upon Cycling of the Li-Rich Layered Oxide Li1.20Mn0.54Co 0.13Ni0.13O2 in Li Ion Batteries. *Journal of Physical Chemistry C* **2014**, *118* (11), 5700–5709. https://doi.org/10.1021/jp412197z.

(135) Croy, J. R.; Gallagher, K. G.; Balasubramanian, M.; Long, B. R.; Thackeray, M. M. Quantifying Hysteresis and Voltage Fade in XLi 2 MnO 3 ● (1-x)LiMn 0.5 Ni 0.5 O 2 Electrodes as a Function of Li 2 MnO 3 Content. *Journal of The Electrochemical Society* **2013**, *161* (3), A318–A325. https://doi.org/10.1149/2.049403jes.

(136) Dalba, G.; Fornasini, P. EXAFS Debye - Waller Factor and Thermal Vibrations of Crystals. *Journal of Synchrotron Radiation* **1997**, *4* (4), 243–255. https://doi.org/10.1107/S0909049597006900.

(137) Zeng, D.; Cabana, J.; Bréger, J.; Yoon, W.; Grey, C. P. Cation Ordering in Li [Ni x Mn x Co (1 – 2 x)] O 2 -Layered Cathode Materials : A Nuclear Magnetic Resonance (NMR), Pair Distribution Function , X-Ray Absorption Spectroscopy , and Electrochemical Study. **2007**, No. 6, 6277–6289.

(138) Shi, Y.; Zhang, M.; Meng, Y. S.; Chen, Z. Ambient-Pressure Relithiation of Degraded LixNi0.5Co0.2Mn0.3O2 ($0 < x < 1$) via Eutectic Solutions for Direct Regeneration of Lithium-Ion Battery Cathodes. *Advanced Energy Materials* **2019**, *9* (20). https://doi.org/10.1002/aenm.201900454.

(139) Li, Y.; Bai, Y.; Bi, X.; Qian, J.; Ma, L.; Tian, J.; Wu, C.; Wu, F.; Lu, J.; Amine, K. An Effectively Activated Hierarchical Nano-/Microspherical Li 1.2 Ni 0.2 Mn 0.6 O 2 Cathode for Long-Life and High-Rate Lithium-Ion Batteries. *ChemSusChem* **2016**, *9* (7), 728–735. https://doi.org/10.1002/cssc.201501548.

(140) Xu, B.; Fell, C. R.; Chi, M.; Meng, Y. S. Identifying Surface Structural Changes in Layered Li-Excess Nickel Manganese Oxides in High Voltage Lithium Ion Batteries: A Joint Experimental and Theoretical Study. *Energy and Environmental Science* **2011**, *4* (6), 2223–2233. https://doi.org/10.1039/c1ee01131f.

(141) Singer, A.; Hy, S.; Zhang, M.; Cela, D.; Fang, C.; Qiu, B.; Xia, Y.; Liu, Z.; Ulvestad, A.; Hua, N.; Wingert, J.; Liu, H.; Sprung, M.; Zozulya, A. v.; Maxey, E.; Harder, R.; Meng, Y. S.; Shpyrko, O. G. Nucleation of Dislocations and Their Dynamics in Layered Oxides Cathode Materials during Battery Charging. *Nature Energy* **2017**, *3(8)*, 641–647.

(142) Li, L.; Song, B. H.; Chang, Y. L.; Xia, H.; Yang, J. R.; Lee, K. S.; Lu, L. Retarded Phase Transition by Fluorine Doping in Li-Rich Layered Li 1.2 Mn 0.54 Ni 0.13 Co 0.13 O 2 Cathode Material. *Journal of Power Sources* **2015**, *283*, 162–170. https://doi.org/10.1016/j.jpowsour.2015.02.085.

(143) Li, W.; Cho, Y.-G.; Yao, W.; Li, Y.; Cronk, A.; Shimizu, R.; Schroeder, M. A.; Fu, Y.; Zou, F.; Battaglia, V.; Manthiram, A.; Zhang, M.; Meng, Y. S. Enabling High Areal Capacity for Co-Free High Voltage Spinel Materials in next-Generation Li-Ion Batteries. *Journal of Power Sources* **2020**, *473*, 228579. https://doi.org/10.1016/j.jpowsour.2020.228579.

(144) Metzger, M.; Walke, P.; Solchenbach, S.; Salitra, G.; Aurbach, D.; Gasteiger, H. A. Evaluating the High-Voltage Stability of Conductive Carbon and Ethylene Carbonate with Various Lithium Salts. *Journal of The Electrochemical Society* **2020**, *167* (16), 160522. https://doi.org/10.1149/1945-7111/abcabd.

(145) Han, J.; Kim, K.; Lee, Y.; Choi, N. Scavenging Materials to Stabilize LiPF 6 -Containing Carbonate-Based Electrolytes for Li-Ion Batteries. *Advanced Materials* **2019**, *31* (20), 1804822. https://doi.org/10.1002/adma.201804822.

(146) Liu, M.; Vatamanu, J.; Chen, X.; Xing, L.; Xu, K.; Li, W. Hydrolysis of LiPF 6 -Containing Electrolyte at High Voltage. *ACS Energy Letters* **2021**, *6* (6), 2096–2102. https://doi.org/10.1021/acsenergylett.1c00707.

(147) Wang, L.; Ma, Y.; Li, Q.; Zhou, Z.; Cheng, X.; Zuo, P.; Du, C.; Gao, Y.; Yin, G. 1,3,6-Hexanetricarbonitrile as Electrolyte Additive for Enhancing Electrochemical Performance of High Voltage Li-Rich Layered Oxide Cathode. *Journal of Power Sources* **2017**, *361*, 227–236. https://doi.org/10.1016/j.jpowsour.2017.06.075.

(148) Lan, J.; Zheng, Q.; Zhou, H.; Li, J.; Xing, L.; Xu, K.; Fan, W.; Yu, L.; Li, W. Stabilizing a High-Voltage Lithium-Rich Layered Oxide Cathode with a Novel Electrolyte Additive. *ACS Applied Materials and Interfaces* **2019**, *11* (32), 28841–28850. https://doi.org/10.1021/acsami.9b07441.

(149) Cha, J.; Han, J. G.; Hwang, J.; Cho, J.; Choi, N. S. Mechanisms for Electrochemical Performance Enhancement by the Salt-Type Electrolyte Additive, Lithium Difluoro(Oxalato)Borate, in High-Voltage Lithium-Ion Batteries. *Journal of Power Sources* **2017**, *357*, 97–106. https://doi.org/10.1016/j.jpowsour.2017.04.094.

(150) Liu, W.; Li, J.; Li, W.; Xu, H.; Zhang, C.; Qiu, X. Inhibition of Transition Metals Dissolution in Cobalt-Free Cathode with Ultrathin Robust Interphase in Concentrated Electrolyte. *Nature Communications* **2020**, *11* (1), 3629. https://doi.org/10.1038/s41467-020-17396-x.

(151) Brutti, S.; Simonetti, E.; De Francesco, M.; Sarra, A.; Paolone, A.; Palumbo, O.; Fantini, S.; Lin, R.; Falgayrat, A.; Choi, H.; Kuenzel, M.; Passerini, S.; Appetecchi, G. B. Ionic Liquid Electrolytes for High-Voltage, Lithium-Ion Batteries. *Journal of Power Sources* **2020**, *479*, 228791. https://doi.org/10.1016/j.jpowsour.2020.228791.

(152) Im, J.; Lee, J.; Ryou, M.-H.; Lee, Y. M.; Cho, K. Y. Fluorinated Carbonate-Based Electrolyte for High-Voltage Li(Ni 0.5 Mn 0.3 Co 0.2)O 2 /Graphite Lithium-Ion Battery. *Journal of The Electrochemical Society* **2017**, *164* (1), A6381–A6385. https://doi.org/10.1149/2.0591701jes.

(153) Zhu, Y.; Yang, J.; Cheng, G.; Carroll, K.; Clemons, O.; Strand, D. *Novel Non-Carbonate Based Electrolytes for Silicon Anodes*; Pittsburgh, PA, and Morgantown, WV (United States), 2016. https://doi.org/10.2172/1351982.

(154) Noguchi, T.; Hasegawa, T.; Yamauchi, H.; Yamazaki, I.; Utsugi, K. Effect of Using Fluorinated Ether and Sulfone as Electrolyte Solvents for Lithium Ion Batteries with Lithium-Rich Layered Cathodes and Silicon Oxide Anodes. *ECS Transactions* **2017**, *80* (10), 291–303. https://doi.org/10.1149/08010.0291ecst.

(155) Ehteshami, N.; Paillard, E. Ethylene Carbonate-Free, Adiponitrile-Based Electrolytes Compatible with Graphite Anodes. *ECS Transactions* **2017**, *77* (1), 11–20. https://doi.org/10.1149/07701.0011ecst.

(156) Zhao, J.; Liang, Y.; Zhang, X.; Zhang, Z.; Wang, E.; He, S.; Wang, B.; Han, Z.; Lu, J.; Amine, K.; Yu, H. In Situ Construction of Uniform and Robust Cathode–Electrolyte Interphase for Li-Rich Layered Oxides. *Advanced Functional Materials* **2021**, *31* (8), 2009192. https://doi.org/10.1002/adfm.202009192.

(157) Xu, W.; Angell, C. A. Weakly Coordinating Anions, and the Exceptional Conductivity of Their Nonaqueous Solutions. *Electrochemical and Solid-State Letters* **2001**, *4* (1), E1. https://doi.org/10.1149/1.1344281.

(158) Lishka, U.; Wietelmann, U.; Wegner, M. Pat. DE 19829030 C1, 1999.

(159) Xu, K.; Zhang, S.; Jow, T. R.; Xu, W.; Angell, C. A. LiBOB as Salt for Lithium-Ion Batteries. A Possible Solution for High Temperature Operation. *Electrochemical and Solid-State Letters* **2002**, *5* (1), 26–29. https://doi.org/10.1149/1.1426042.

(160) Lian, F.; Li, Y.; He, Y.; Guan, H.; Yan, K.; Qiu, W.; Chou, K. C.; Axmann, P.; Wohlfahrt-Mehrens, M. Preparation of LiBOB via Rheological Phase Method and Its Application to Mitigate Voltage Fade of Li1.16[Mn0.75Ni0.25]0.84O2 Cathode. *RSC Advances* **2015**, *5* (105), 86763–86770. https://doi.org/10.1039/c5ra18520c.

(161) Xu, M.; Zhou, L.; Dong, Y.; Chen, Y.; Garsuch, A.; Lucht, B. L. Improving the Performance of Graphite/ LiNi 0.5 Mn 1.5 O 4 Cells at High Voltage and Elevated Temperature with Added Lithium Bis(Oxalato) Borate (LiBOB). *Journal of The Electrochemical Society* **2013**, *160* (11), A2005–A2013. https://doi.org/10.1149/2.053311jes.

(162) Dalavi, S.; Xu, M.; Knight, B.; Lucht, B. L. Effect of Added LiBOB on High Voltage (LiNi0.5Mn1.5O4) Spinel Cathodes. *Electrochemical and Solid-State Letters* **2011**, *15* (2), A28–A31. https://doi.org/10.1149/2.015202esl.

(163) Aravindan, V.; Cheah, Y. L.; Ling, W. C.; Madhavi, S. Effect of LiBOB Additive on the Electrochemical Performance of LiCoPO 4. *Journal of The Electrochemical Society* **2012**, *159* (9), A1435–A1439. https://doi.org/10.1149/2.024209jes.

(164) Xiao, Z.; Liu, J.; Fan, G.; Yu, M.; Liu, J.; Gou, X.; Yuan, M.; Cheng, F. Lithium Bis(Oxalate)Borate Additive in the Electrolyte to Improve Li-Rich Layered Oxide Cathode Materials. *Materials Chemistry Frontiers* **2020**, *4* (6), 1689–1696. https://doi.org/10.1039/D0QM00094A.

(165) Bian, X.; Ge, S.; Pang, Q.; Zhu, K.; Wei, Y.; Zou, B.; Du, F.; Zhang, D.; Chen, G. A Novel Lithium Difluoro(Oxalate) Borate and Lithium Hexafluoride Phosphate Dual-Salt Electrolyte for Li-Excess Layered Cathode Material. *Journal of Alloys and Compounds* **2018**. https://doi.org/10.1016/j.jallcom.2017.11.126.

(166) Xu, M.; Tsiouvaras, N.; Garsuch, A.; Gasteiger, H. A.; Lucht, B. L. Generation of Cathode Passivation Films via Oxidation of Lithium Bis(Oxalato) Borate on High Voltage Spinel (LiNi 0.5 Mn 1.5 O 4). *J. Phys. Chem. C* **2014**, *118*, 37. https://doi.org/10.1021/jp501970j.

(167) Dong, Y.; Young, B. T.; Zhang, Y.; Yoon, T.; Heskett, D. R.; Hu, Y.; Lucht, B. L. Effect of Lithium Borate Additives on Cathode Film Formation in LiNi0.5Mn1.5O4/Li Cells. *ACS Applied Materials and Interfaces* **2017**, *9* (24), 20467–20475. https://doi.org/10.1021/acsami.7b01481.

(168) Shi, J. L.; Zhang, J. N.; He, M.; Zhang, X. D.; Yin, Y. X.; Li, H.; Guo, Y. G.; Gu, L.; Wan, L. J. Mitigating Voltage Decay of Li-Rich Cathode Material via Increasing Ni Content for Lithium-Ion Batteries. *ACS Applied Materials and Interfaces* **2016**, *8* (31), 20138–20146. https://doi.org/10.1021/acsami.6b06733.

(169) Wei, Z.; Zhang, W.; Wang, F.; Zhang, Q.; Qiu, B.; Han, S.; Xia, Y.; Zhu, Y.; Liu, Z. Eliminating Voltage Decay of Lithium-Rich Li1.14Mn0.54Ni0.14Co0.14O2 Cathodes by Controlling the Electrochemical Process. *Chemistry - A European Journal* **2015**, *21* (20), 7503–7510. https://doi.org/10.1002/chem.201406641.

(170) Zhang, J.; Zhang, Q.; Wong, D.; Zhang, N.; Ren, G.; Gu, L.; Schulz, C.; He, L.; Yu, Y.; Liu, X. Addressing Voltage Decay in Li-Rich Cathodes by Broadening the Gap between Metallic and Anionic Bands. *Nature Communications* **2021**, *12* (1), 3071. https://doi.org/10.1038/s41467-021-23365-9.

(171) Wang, J.; He, X.; Paillard, E.; Laszczynski, N.; Li, J.; Passerini, S. Lithium- and Manganese-Rich Oxide Cathode Materials for High-Energy Lithium Ion Batteries. *Advanced Energy Materials* **2016**, *6* (21), 1600906. https://doi.org/10.1002/aenm.201600906.

(172) Assat, G.; Tarascon, J. M. Fundamental Understanding and Practical Challenges of Anionic Redox Activity in Li-Ion Batteries. *Nature Energy* **2018**, *3* (5), 373–386. https://doi.org/10.1038/s41560-018-0097-0.

(173) Thackeray, M. M.; Kang, S.-H.; Johnson, C. S.; Vaughey, J. T.; Benedek, R.; Hackney, S. A. Li2MnO3-Stabilized LiMO2 (M = Mn, Ni, Co) Electrodes for Lithium-Ion Batteries. *Journal of Materials Chemistry* **2007**, *17* (30), 3112. https://doi.org/10.1039/b702425h.

(174) Assat, G.; Foix, D.; Delacourt, C.; Iadecola, A.; Dedryvère, R.; Tarascon, J.-M. Fundamental Interplay between Anionic/Cationic Redox Governing the Kinetics and Thermodynamics of Lithium-Rich Cathodes. *Nature Communications* **2017**, *8* (1), 2219. https://doi.org/10.1038/s41467-017-02291-9.

(175) Shi, J.-L.; Zhang, J.-N.; He, M.; Zhang, X.-D.; Yin, Y.-X.; Li, H.; Guo, Y.-G.; Gu, L.; Wan, L.-J. Mitigating Voltage Decay of Li-Rich Cathode Material via Increasing Ni Content for Lithium-Ion Batteries. *ACS Applied Materials & Interfaces* **2016**, *8* (31), 20138–20146. https://doi.org/10.1021/acsami.6b06733.

(176) Jiao, S.; Ren, X.; Cao, R.; Engelhard, M. H.; Liu, Y.; Hu, D.; Mei, D.; Zheng, J.; Zhao, W.; Li, Q.; Liu, N.; Adams, B. D.; Ma, C.; Liu, J.; Zhang, J.-G.; Xu, W. Stable Cycling of High-Voltage Lithium Metal Batteries in Ether Electrolytes. *Nature Energy* **2018**, *3* (9), 739–746. https://doi.org/10.1038/s41560-018-0199-8.

(177) Ha, S. Y.; Han, J. G.; Song, Y. M.; Chun, M. J.; Han, S. Il; Shin, W. C.; Choi, N. S. Using a Lithium Bis(Oxalato) Borate Additive to Improve Electrochemical Performance of High-Voltage Spinel LiNi0.5Mn1.5O 4 Cathodes at 60 °c. *Electrochimica Acta* **2013**, *104*, 170–177. https://doi.org/10.1016/j.electacta.2013.04.082.

(178) Cui, C.; Fan, X.; Zhou, X.; Chen, J.; Wang, Q.; Ma, L.; Yang, C.; Hu, E.; Yang, X.-Q.; Wang, C. Structure and Interface Design Enable Stable Li-Rich Cathode. *J Am Chem Soc* **2020**, *142* (19), 8918–8927. https://doi.org/10.1021/jacs.0c02302.

(179) Xu, M.; Tsiouvaras, N.; Garsuch, A.; Gasteiger, H. A.; Lucht, B. L. Generation of Cathode Passivation Films via Oxidation of Lithium Bis(Oxalato) Borate on High Voltage Spinel (LiNi 0.5 Mn 1.5 O 4). *The Journal of Physical Chemistry C* **2014**, *118* (14), 7363–7368. https://doi.org/10.1021/jp501970j.

(180) Zhao, E.; Zhang, M.; Wang, X.; Hu, E.; Liu, J.; Yu, X.; Olguin, M.; Wynn, T. A.; Meng, Y. S.; Page, K.; Wang, F.; Li, H.; Yang, X.-Q.; Huang, X.; Chen, L. Local Structure Adaptability through Multi Cations for Oxygen Redox Accommodation in Li-Rich Layered Oxides. *Energy Storage Materials* **2020**, *24*, 384–393. https://doi.org/10.1016/j.ensm.2019.07.032.

(181) Tan, C.; Yang, J.; Pan, Q.; Li, Y.; Li, Y.; Cui, L.; Fan, X.; Zheng, F.; Wang, H.; Li, Q. Optimizing Interphase Structure to Enhance Electrochemical Performance of High Voltage LiNi0.5Mn1.5O4 Cathode via Anhydride Additives. *Chemical Engineering Journal* **2021**, *410*, 128422. https://doi.org/10.1016/j.cej.2021.128422.

(182) Dong, Y.; Young, B. T.; Zhang, Y.; Yoon, T.; Heskett, D. R.; Hu, Y.; Lucht, B. L. Effect of Lithium Borate Additives on Cathode Film Formation in LiNi 0.5 Mn 1.5 O 4 /Li Cells. *ACS Applied Materials & Interfaces* **2017**, *9* (24), 20467–20475. https://doi.org/10.1021/acsami.7b01481.

(183) Diehl, M.; Evertz, M.; Winter, M.; Nowak, S. Deciphering the Lithium Ion Movement in Lithium Ion Batteries: Determination of the Isotopic Abundances of 6 Li and 7 Li. *RSC Advances* **2019**, *9* (21), 12055–12062. https://doi.org/10.1039/C9RA02312G.

(184) Abeywardana, M. Y.; Laszczynski, N.; Kuenzel, M.; Bresser, D.; Passerini, S.; Lucht, B. Increased Cycling Performance of Li-Ion Batteries by Phosphoric Acid Modified $LiNi_{0.5}Mn_{1.5}O_4$ Cathodes in the Presence of LiBOB. *International Journal of Electrochemistry* **2019**, *2019*, 1–7. https://doi.org/10.1155/2019/8636540.

(185) Parimalam, B. S.; MacIntosh, A. D.; Kadam, R.; Lucht, B. L. Decomposition Reactions of Anode Solid Electrolyte Interphase (SEI) Components with $LiPF_6$. *The Journal of Physical Chemistry C* **2017**, *121* (41), 22733–22738. https://doi.org/10.1021/acs.jpcc.7b08433.

(186) Nie, M.; Lucht, B. L. Role of Lithium Salt on Solid Electrolyte Interface (SEI) Formation and Structure in Lithium Ion Batteries. *Journal of The Electrochemical Society* **2014**, *161* (6), A1001–A1006. https://doi.org/10.1149/2.054406jes.

(187) Lu, D.; Xu, G.; Hu, Z.; Cui, Z.; Wang, X.; Li, J.; Huang, L.; Du, X.; Wang, Y.; Ma, J.; Lu, X.; Lin, H. J.; Chen, C. Te; Nugroho, A. A.; Tjeng, L. H.; Cui, G. Deciphering the Interface of a High-Voltage (5 V-Class) Li-Ion Battery Containing Additive-Assisted Sulfolane-Based Electrolyte. *Small Methods* **2019**, *3* (10), 1900546. https://doi.org/10.1002/smtd.201900546.

(188) Weber, R.; Genovese, M.; Louli, A. J.; Hames, S.; Martin, C.; Hill, I. G.; Dahn, J. R. Long Cycle Life and Dendrite-Free Lithium Morphology in Anode-Free Lithium Pouch Cells Enabled by a Dual-Salt Liquid Electrolyte. *Nature Energy* **2019**, *4* (8), 683–689. https://doi.org/10.1038/s41560-019-0428-9.

(189) Xiao, A.; Yang, L.; Lucht, B. L. Thermal Reactions of LiPF[Sub 6] with Added LiBOB. *Electrochemical and Solid-State Letters* **2007**, *10* (11), A241. https://doi.org/10.1149/1.2772084.

(190) Choi, N.-S.; Han, J.-G.; Ha, S.-Y.; Park, I.; Back, C.-K. Recent Advances in the Electrolytes for Interfacial Stability of High-Voltage Cathodes in Lithium-Ion Batteries. *RSC Advances* **2015**, *5* (4), 2732–2748. https://doi.org/10.1039/C4RA11575A.

(191) Louli, A. J.; Eldesoky, A.; Weber, R.; Genovese, M.; Coon, M.; deGooyer, J.; Deng, Z.; White, R. T.; Lee, J.; Rodgers, T.; Petibon, R.; Hy, S.; Cheng, S. J. H.; Dahn, J. R. Diagnosing and Correcting Anode-Free Cell Failure via Electrolyte and Morphological Analysis. *Nature Energy* **2020**, *5* (9), 693–702. https://doi.org/10.1038/s41560-020-0668-8.

(192) Schulz, N.; Hausbrand, R.; Wittich, C.; Dimesso, L.; Jaegermann, W. XPS-Surface Analysis of SEI Layers on Li-Ion Cathodes: Part II. SEI-Composition and Formation inside Composite Electrodes. *Journal of The Electrochemical Society* **2018**, *165* (5), A833–A846. https://doi.org/10.1149/2.0881803jes.

(193) An, S. J.; Li, J.; Daniel, C.; Mohanty, D.; Nagpure, S.; Wood, D. L. The State of Understanding of the Lithium-Ion-Battery Graphite Solid Electrolyte Interphase (SEI) and Its Relationship to Formation Cycling. *Carbon N Y* **2016**, *105*, 52–76. https://doi.org/10.1016/j.carbon.2016.04.008.

(194) Zhang, J.; Yang, J.; Yang, L.; Lu, H.; Liu, H.; Zheng, B. Exploring the Redox Decomposition of Ethylene Carbonate–Propylene Carbonate in Li-Ion Batteries. *Materials Advances* **2021**, *2* (5), 1747–1751. https://doi.org/10.1039/d0ma00847h.

(195) Metzger, M.; Sicklinger, J.; Haering, D.; Kavakli, C.; Stinner, C.; Marino, C.; Gasteiger, H. A. Carbon Coating Stability on High-Voltage Cathode Materials in H_2O-Free and H_2O-Containing Electrolyte. *Journal of The Electrochemical Society* **2015**, *162* (7), A1227–A1235. https://doi.org/10.1149/2.0461507jes.

(196) Metzger, M.; Strehle, B.; Solchenbach, S.; Gasteiger, H. A. Hydrolysis of Ethylene Carbonate with Water and Hydroxide under Battery Operating Conditions. *Journal of The Electrochemical Society* **2016**, *163* (7), A1219–A1225. https://doi.org/10.1149/2.0411607jes.

(197) Xing, L.; Li, W.; Wang, C.; Gu, F.; Xu, M.; Tan, C.; Yi, J. Theoretical Investigations on Oxidative Stability of Solvents and Oxidative Decomposition Mechanism of Ethylene Carbonate for Lithium Ion Battery Use. *The Journal of Physical Chemistry B* **2009**, *113* (52), 16596–16602. https://doi.org/10.1021/jp9074064.

(198) Philippe, B.; Hahlin, M.; Edström, K.; Gustafsson, T.; Siegbahn, H.; Rensmo, H. Photoelectron Spectroscopy for Lithium Battery Interface Studies. *Journal of The Electrochemical Society* **2016**, *163* (2), A178–A191. https://doi.org/10.1149/2.0051602jes.

(199) Cox, J. D.; Wagman, D. D.; Medvedev, V. A. *CODATA Key Values for Thermodynamics*; 1984; Vol. 1. https://doi.org/10.11311/jscta1974.3.61.

(200) Cottrell, T. L. *The Strengths of Chemical Bonds*; Butterworths Scientific Publications: London, 1958.

(201) Ellis, L. D.; Hill, I. G.; Gering, K. L.; Dahn, J. R. Synergistic Effect of LiPF 6 and LiBF 4 as Electrolyte Salts in Lithium-Ion Cells. *Journal of The Electrochemical Society* **2017**, *164* (12), A2426–A2433. https://doi.org/10.1149/2.0811712jes.

(202) Janek, J.; Zeier, W. G. A Solid Future for Battery Development. *Nature Energy* **2016**, *1* (9), 16141. https://doi.org/10.1038/nenergy.2016.141.

(203) Schmuch, R.; Wagner, R.; Hörpel, G.; Placke, T.; Winter, M. Performance and Cost of Materials for Lithium-Based Rechargeable Automotive Batteries. *Nature Energy* **2018**, *3* (4), 267–278. https://doi.org/10.1038/s41560-018-0107-2.

(204) Andre, D.; Kim, S.-J.; Lamp, P.; Lux, S. F.; Maglia, F.; Paschos, O.; Stiaszny, B. Future Generations of Cathode Materials: An Automotive Industry Perspective. *Journal of Materials Chemistry A* **2015**, *3* (13), 6709–6732. https://doi.org/10.1039/C5TA00361J.

(205) Wang, R.; Chen, X.; Huang, Z.; Yang, J.; Liu, F.; Chu, M.; Liu, T.; Wang, C.; Zhu, W.; Li, S.; Li, S.; Zheng, J.; Chen, J.; He, L.; Jin, L.; Pan, F.; Xiao, Y. Twin Boundary Defect Engineering Improves Lithium-Ion Diffusion for Fast-Charging Spinel Cathode Materials. *Nature Communications* **2021**, *12* (1), 3085. https://doi.org/10.1038/s41467-021-23375-7.

(206) Zhang, J.-N.; Li, Q.; Ouyang, C.; Yu, X.; Ge, M.; Huang, X.; Hu, E.; Ma, C.; Li, S.; Xiao, R.; Yang, W.; Chu, Y.; Liu, Y.; Yu, H.; Yang, X.-Q.; Huang, X.; Chen, L.; Li, H. Trace Doping of Multiple Elements Enables Stable Battery Cycling of LiCoO2 at 4.6 V. *Nature Energy* **2019**, *4* (7), 594–603. https://doi.org/10.1038/s41560-019-0409-z.

(207) Wynn, T. A.; Fang, C.; Zhang, M.; Liu, H.; Davies, D. M.; Wang, X.; Lau, D.; Lee, J. Z.; Huang, B.-Y.; Fung, K.-Z.; Ni, C.-T.; Meng, Y. S. Mitigating Oxygen Release in Anionic-Redox-Active Cathode Materials by Cationic Substitution through Rational Design. *Journal of Materials Chemistry A* **2018**, *6* (47). https://doi.org/10.1039/C8TA06296J.

(208) Piao, J.-Y.; Sun, Y.-G.; Duan, S.-Y.; Cao, A.-M.; Wang, X.-L.; Xiao, R.-J.; Yu, X.-Q.; Gong, Y.; Gu, L.; Li, Y.; Liu, Z.-J.; Peng, Z.-Q.; Qiao, R.-M.; Yang, W.-L.; Yang, X.-Q.; Goodenough, J. B.; Wan, L.-J. Stabilizing Cathode Materials of Lithium-Ion Batteries by Controlling Interstitial Sites on the Surface. *Chem* **2018**, *4* (7), 1685–1695. https://doi.org/10.1016/j.chempr.2018.04.020.

(209) Yan, P.; Zheng, J.; Gu, M.; Xiao, J.; Zhang, J.-G.; Wang, C.-M. Intragranular Cracking as a Critical Barrier for High-Voltage Usage of Layer-Structured Cathode for Lithium-Ion Batteries. *Nature Communications* **2017**, *8* (1), 14101. https://doi.org/10.1038/ncomms14101.

(210) Ulvestad, A.; Singer, A.; Clark, J. N.; Cho, H. M.; Kim, J. W.; Harder, R.; Maser, J.; Meng, Y. S.; Shpyrko, O. G. Topological Defect Dynamics in Operando Battery Nanoparticles. *Science (1979)* **2015**, *348* (6241), 1344–1347. https://doi.org/10.1126/science.aaa1313.

(211) Chung, H.; Li, Y.; Zhang, M.; Grenier, A.; Mejia, C.; Cheng, D.; Sayahpour, B.; Song, C.; Shen, M. H.; Huang, R.; Wu, E. A.; Chapman, K. W.; Kim, S. J.; Meng, Y. S. Mitigating

Anisotropic Changes in Classical Layered Oxide Materials by Controlled Twin Boundary Defects for Long Cycle Life Li-Ion Batteries. *Chemistry of Materials* **2022**. https://doi.org/10.1021/acs.chemmater.2c01234.

(212) Jiao, F.; Bao, J.; Hill, A. H.; Bruce, P. G. Synthesis of Ordered Mesoporous Li-Mn-O Spinel as a Positive Electrode for Rechargeable Lithium Batteries. *Angewandte Chemie International Edition* **2008**, *47* (50), 9711–9716. https://doi.org/10.1002/anie.200803431.

(213) Qian, G.; Zhang, Y.; Li, L.; Zhang, R.; Xu, J.; Cheng, Z.; Xie, S.; Wang, H.; Rao, Q.; He, Y.; Shen, Y.; Chen, L.; Tang, M.; Ma, Z. F. Single-Crystal Nickel-Rich Layered-Oxide Battery Cathode Materials: Synthesis, Electrochemistry, and Intra-Granular Fracture. *Energy Storage Materials* **2020**, *27*, 140–149. https://doi.org/10.1016/J.ENSM.2020.01.027.

(214) Kim, Y. Lithium Nickel Cobalt Manganese Oxide Synthesized Using Alkali Chloride Flux: Morphology and Performance As a Cathode Material for Lithium Ion Batteries. *ACS Applied Materials & Interfaces* **2012**, *4* (5), 2329–2333. https://doi.org/10.1021/am300386j.

(215) Li, H.; Li, J.; Ma, X.; Dahn, J. R. Synthesis of Single Crystal $LiNi_{0.6}Mn_{0.2}Co_{0.2}O_2$ with Enhanced Electrochemical Performance for Lithium Ion Batteries. *Journal of The Electrochemical Society* **2018**, *165* (5), A1038–A1045. https://doi.org/10.1149/2.0951805jes.

(216) Guo, F.; Xie, Y.; Zhang, Y. Low-Temperature Strategy to Synthesize Single-Crystal LiNi0.8Co0.1Mn0.1O2 with Enhanced Cycling Performances as Cathode Material for Lithium-Ion Batteries. *Nano Research* **2022**, *15* (3), 2052–2059. https://doi.org/10.1007/s12274-021-3784-2.

(217) Fan, X.; Wang, C. High-Voltage Liquid Electrolytes for Li Batteries: Progress and Perspectives. *Chemical Society Reviews* **2021**, *50* (18), 10486–10566. https://doi.org/10.1039/D1CS00450F.

(218) Doi, T.; Masuhara, R.; Hashinokuchi, M.; Shimizu, Y.; Inaba, M. Concentrated LiPF6/PC Electrolyte Solutions for 5-V LiNi0.5Mn1.5O4 Positive Electrode in Lithium-Ion Batteries. *Electrochimica Acta* **2016**, *209*, 219–224. https://doi.org/10.1016/J.ELECTACTA.2016.05.062.

(219) Peng, X.; Lin, Y.; Wang, Y.; Li, Y.; Zhao, T. A Lightweight Localized High-Concentration Ether Electrolyte for High-Voltage Li-Ion and Li-Metal Batteries. *Nano Energy* **2022**, *96*, 107102. https://doi.org/10.1016/J.NANOEN.2022.107102.

(220) Ko, S.; Yamada, Y.; Yamada, A. A 4.8 V Reversible Li_2CoPO_4F/Graphite Battery Enabled by Concentrated Electrolytes and Optimized Cell Design. *Batteries & Supercaps* **2020**, *3* (9), 910–916. https://doi.org/10.1002/batt.202000050.

(221) Zhang, X.; Jia, H.; Xu, Y.; Zou, L.; Engelhard, M. H.; Matthews, B. E.; Wang, C.; Zhang, J. G.; Xu, W. Unravelling High-Temperature Stability of Lithium-Ion Battery with

Lithium-Rich Oxide Cathode in Localized High-Concentration Electrolyte. *Journal of Power Sources Advances* **2020**, *5*, 100024. https://doi.org/10.1016/J.POWERA.2020.100024.

(222) Ren, F.; Li, Z.; Chen, J.; Huguet, P.; Peng, Z.; Deabate, S. Solvent–Diluent Interaction-Mediated Solvation Structure of Localized High-Concentration Electrolytes. *ACS Applied Materials & Interfaces* **2022**, *14* (3), 4211–4219. https://doi.org/10.1021/acsami.1c21638.